ABSTRACT

Title of dissertation: A H_∞ Loop Shaping Framework for Bio-Inspired Sensorimotor Control

Jishnu Keshavan, Doctor of Philosophy, 2012

Dissertation directed by: Associate Professor J. Sean Humbert
Department of Aerospace Engineering

The insect visuomotor system combines a lightweight and high bandwidth sensor with fast processing algorithms for efficient information extraction that enables autonomous navigation in complex, obstacle laden environments. In this dissertation, a H_∞ loop shaping controller synthesis framework is introduced to couple the dynamic controller with an information extraction approach based on the processing of optic flow patterns by using wide-field motion-sensitive interneurons in the insect visuomotor system. Local proximity and velocity estimates are obtained with an optic flow model that is based on parameterization of typical three-dimensional urban environments. The insect inspired visual navigation technique developed in the dissertation combines optic flow outputs with a H_∞ controller to provide robust stability in a cluttered environment while mitigating measurement noise and gusts. Simulation-based validation studies are undertaken and the loop shaping approach is used to overcome limitation in optic flow-based navigation for planar applications as well as demonstrate safe obstacle avoidance and terrain following behavior on an autonomous rotary wing miro-air-vehicle (MAV) for an urban-like environment

subjected to gusts for both planar and 3D navigation applications.

In addition, an alternate approach to the H_∞ loop shaping framework is considered, based on using hair mechanosensory arrays in conjunction with optic flow outputs for enabling safe reflexive navigation. The hair sensor array outputs are combined with optic flow outputs within a biomimetic control framework and simulation-based studies are carried out to investigate their impact on the dynamics of a fixed wing MAV in an urban environment. The use of hair sensor arrays is found to augment stability and improve gust rejection performance resulting in safe obstacle avoidance behavior in the urban environment.

A H_∞ Loop Shaping Framework for Bio-Inspired Sensorimotor Control

by

Jishnu Keshavan

Dissertation submitted to the Faculty of the Graduate School of the
University of Maryland, College Park in partial fulfillment
of the requirements for the degree of
Doctor of Philosophy
2012

Advisory Committee:
Associate Professor J. Sean Humbert, Chair/Advisor
Professor Inderjit Chopra
Professor Balakumar Balachandran
Professor Norman M. Wereley
Associate Professor James Baeder

Acknowledgments

It has been a long journey with plenty of surprises along the way. I owe a debt of gratitude to my advisor Dr. J. Sean Humbert for his guidance all the way through. He has always had plenty of time for me, and his patience with my efforts as I dabbled with different projects that apparently led to nowhere, as well as his enthusiasm and dedication to the pursuit of excellence has guided me along.

I would also like to acknowledge my committee for the time taken to read through and provide constructive criticism of my work. Thanks are especially due to Dr. Balakumar Balachandran for his thoughtful suggestions which helped improve the quality of this dissertation. Additionally, cheers to Bryan for help with developing the simulation software used for numerical studies in this work. Also, thanks to Imraan, Andrew, Joe, Kedar, Badri, Mac, Steve and Greg for their valued contributions as well as technical discussions that helped move things along at various stages of my studies.

On the personal front, the last few years have been truly enjoyable. I have had the privilege of being in the company of a large group of fun loving people. The moments spent with my Warriors team-mates,as well as buddies from tennis and squash have been truly memorable. A large thanks goes out to all of 'em.

Finally, I owe everything to my mom, dad and Vaishu. Words cannot nearly suffice to acknowlegde my gratitude. Thanks for being there.

Table of Contents

List of Tables

List of Figures

Nomenclature

u_0	Nominal forward velocity, m/s
y	Lateral offset, m
z	Altitude offset, m
$\dot{y}$	Vehicle lateral velocity in inertial frame, m/s
u	Vehicle forward velocity in body frame, m/s
v	Vehicle lateral velocity in body frame, m/s
w	Vehicle heave velocity in body frame, m/s
ϕ	Vehicle roll attitude, rad
θ	Vehicle pitch attitude, rad
ψ	Vehicle yaw attitude, rad
p	Vehicle roll rate, rad/s
q	Vehicle pitch rate, rad/s
r	Vehicle yaw rate, rad/s
d	Distance
μ	Nearness
$\dot{\mathbf{Q}}$	Planar optic flow field
γ	Azimuth angle, rad
β	Elevation angle, rad
σ	Singular value
a	Nominal longitudinal wall hug distance, m
g	Nominal lateral wall hug distance, m
h	Nominal transverse wall hug distance, m
$\mathbf{q}$	Vehicle configuration
$\dot{\mathbf{q}}$	Vehicle velocity
$\mathbf{x}$	Vehicle state vector
$\mathbf{u}$	Control vector
$\mathbf{y}$	Output vector
F	Sensitivity function
A	State space coefficient matrix
B	Control coefficients matrix
D	Gust disturbance matrix
C	Observation matrix
$C^\dagger$	Pseudo-inverse/Static estimator matrix
K	Gain matrix
K_∞	H_∞ feedback gain
W_1	Pre-compensator
W_2	Post-compensator
G	Nominal open loop plant transfer function
G_s	Nominal shaped plant transfer function
ΔG	Uncertainty plant transfer function
G_{d}	Open loop gust transfer function
$G_{\mathrm{d_{cl}}}$	Closed loop gust transfer function
$\mathcal{F}$	Inertial frame
$\mathcal{B}$	Body frame
$\mathcal{W}$	Wind frame

R	covariance matrix
$\bar{z}$	sonar altitude measurement, m
Λ	normalized micro-helicopter actuator input
ζ	Lateral flapping angle, rad
LL	Flapjack roll input
MM	Flapjack pitch input
NN	Flapjack yaw input
F_{x_t}	Flapjack throttle input
β_{ss}	Sideslip angle, rad
α	Angle-of-attack, rad
ζ_t	Azimuthal angle in wind reference frame, rad
θ_t	Central angle in wind reference frame, rad
χ	Longitudinal flapping angle, rad
Ω	Solid angle
$\boldsymbol{\omega}$	Angular velocity, rad/s
$\mathbf{v}$	Translational velocity, m
$\mathbf{r}$	Viewing station/Measurement node on spherical imaging surface
$\boldsymbol{\eta}$	Optic flow noise
$\mathbf{w}$	Optic flow output measurement noise
$\hat{\boldsymbol{\gamma}}$	Unit vector along azimuthal direction
$\hat{\boldsymbol{\beta}}$	Unit vector along elevation direction
$\boldsymbol{\delta}$	Hair sensor response
K_p	Hair sensor output proportionality constant
Subscript	
ref	Reference trajectory
cl	Closed loop
b	Body frame
s	Shaped plant quantities
lat	Lateral cyclic input
lon	Longitudinal cycle input
mr	Main rotor
t	Thrust
E, W, N, S, D, U	Inertial east, west, north, south, down, up
$\hat{}$	Estimated quantity
$\tilde{}$	Measured quantity
h	Hair sensor array
Abbreviations	
GPS	Global Positioning System
IMU	Inertial Measurement Unit
WFI	Wide-Field Integration
UAV	Unmanned Air Vehicle
MAV	Micro Air Vehicle

Chapter 1

Introduction

Unmanned air vehicles (UAVs) have become increasingly ubiquitous in the fields of aerial surveillance and reconnaissance, weather research and topography. The flight profile typically involves the vehicle flying at high altitudes with global positioning system (GPS) enabled waypoint navigation minimising operator workload (yellow trajectory in Fig. 1.1). Current limitations render terrain hugging profiles that include evading local unmapped obstacles impractical. On the other hand, micro-air-vehicles (MAVs), a subset of UAVs, fly much closer to ground and are envisaged for use in applications such as autonomous reflexive navigation in obstacle laden GPS denied environments subjected to gusts (red and blue trajectories in Fig. 1.1). Safe autonomous operation in such an environment would require an agile vehicle that is capable of sensing and reacting to clutter in the local environment, as well as being robust to uncertainties in terrain and gusts. Given the size and limited processing capabilities available onboard an MAV, this would entail the development of lightweight, high-bandwidth sensors and computationally efficient processing algorithms enabling low-latency actuation and high loop closure rate. While significant progress has been made in fabrication and actuation technology for such micro-systems [1, 2, 3], the development of requisite sensors and processing algorithms suitable for such highly agile vehicles has fallen behind. The aim of this

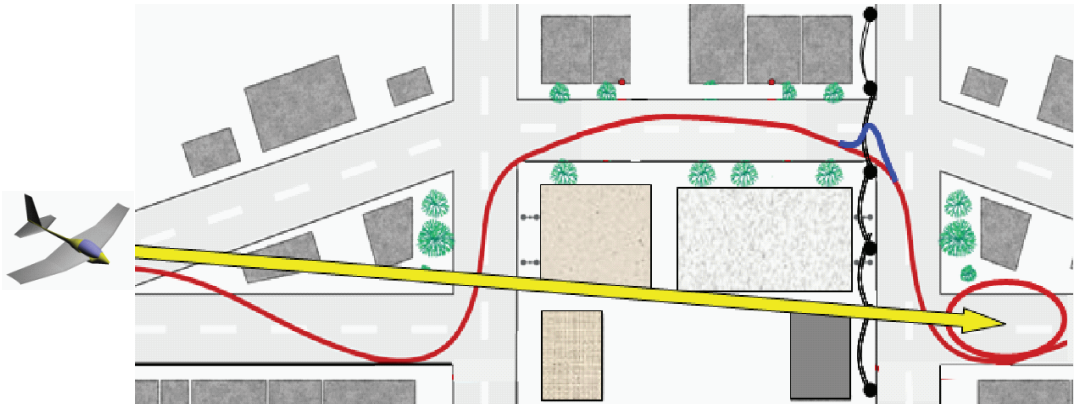

Figure 1.1: UAV autonomous navigation hierarchy; yellow: GPS-guided waypoint navigation, blue: local maneuvering through clutter to target, red: reactive obstacle avoidance preempting maneuver to target.

dissertation is to develop biologically-inspired sensing and control algorithms based on the insect visuomotor system that enable low-level reflexive navigation.

Developing a MAV capable of autonomous navigation in a cluttered environment is a difficult objective to achieve given the current state of sensing technology (Fig. 1.2). The fast dynamics of a MAV alongwith the payload limitations imposed requires high bandwidth sensors of the order of 2 g, that can operate at about 20-50 Hz and consume about 100 mW of power. Sensors such as GPS and Inertial Measurement units (IMU) that are typically employed to provide Kalman-filtered estimates of velocity [4, 5], attitude and inertial location are bandwidth and power limited ($\approx$ 5 Hz and 1 W respectively), weigh about 15-30 g and unavailable indoors. Miniature laser rangefinders and ultrasonics have the requisite bandwidth but are restricted to being point sensors with small fields of view and consume far greater power than available for deploying onboard MAVs [6].

Sensor	Weight (g)	Power (mW)	Bandwidth (Hz)
GPS (position, velocity)	16-28	770-910	4
IMU (attitude, ang. rate)	3	250	200
Rangefinder (distance)	26	400	250
Ultrasonics (distance)	10	1000	20
VLSI Optic Flow (distance, velocity, attitude, ang. rate)	0.25	0.01	500-1000
Target	2	100	20-50

Figure 1.2: Size, power and bandwidth capabilities of typical miniature sensors.

Negotiating a cluttered environment requires a MAV to be capable of sensing proximity to objects in the surrounding environment, especially when it becomes unsafe. Proximity detection capability is uncommon in large vehicles and is considered highly advanced for micro-systems. Vision provides abundant information of the obstacle-rich local environment and is particularly well suited for detecting proximity or generating an environment map. Traditional machine vision approaches that infer proximity and velocity from camera imagery have been implemented; however, these algorithms can be computationally expensive and require significant payload [6, 7, 8, 9, 10], necessitating off-board processing, even for relatively large vehicles with significant payloads [11]. Moreover, their small size and high maneuverability render MAVs acutely susceptible to wind gusts, requiring complicated sensing apparatus for large gust mitigation [12], especially in outdoor environments. For an aerial micro-system with a requirement of both indoor and outdoor operation, there is no viable approach for proximity and velocity estimation for safe obstacle avoidance

behavior. Novel sensing and processing mechanisms then need to be considered for the development of successful autonomous micro-systems.

Nature provides an elegant solution to the problem of robust visual proximity and velocity detection. Flying insects have demonstrated safe navigation behaviour in uncertain environments without the computational complexity that current machine vision algorithms require to perform the same task. Insects utilize optic flow [13, 14], the characteristic patterns of luminance that form on the retina, as they move. These patterns of visual motion are a rich source of motion cues, and they are a function of relative speed and proximity to objects in the surrounding environment [15]. Specialized tangential cell neurons, located in the insect's lobula plate, parse these patterns of optic flow over large fields of view to extract vital motion cues such as relative proximity and velocity for navigation. The robust flight behavior of these insects [16, 17, 18, 19] render optic flow based navigation methodologies particularly suitable for MAVs.

Therefore, the central aim of the dissertation is to utilize optic flow to develop control algorithms that enable accurate extraction of proximity and velocity information and provide stabilising commands for safe reflexive navigation in unknown, obstacle-laden and gusty environments. The methodology developed allows for a degree of uncertainty in the structure of the local environment map, thus precluding the need for either generating accurate environment structure from motion or employing optimization-based trajectory generation strategies.

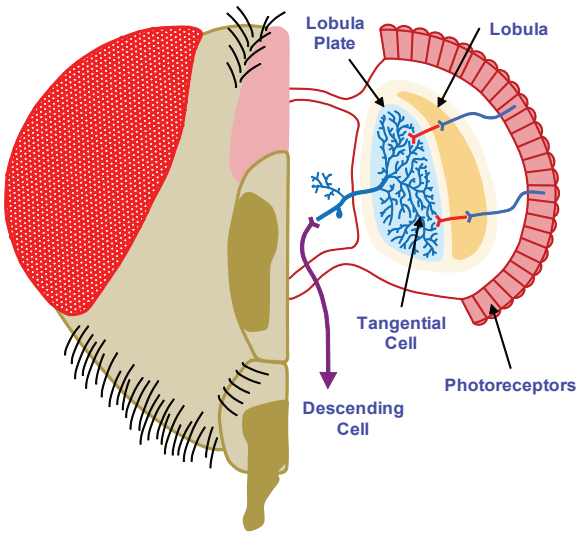

Figure 1.3: Insect visuomotor system.

1.1 Insect Visuomotor System

The insect eye is composed of numerous photoreceptors that function to create patterns of luminance, based on insect motion, on the retina. The relative velocity vector arising from local image shifts mapped over the entire visual field form patterns of optic flow. These patterns of optic flow are a function of insect's relative motion and proximity to objects in the surrounding environment, which can be expressed in closed form [20]. The retinotopic arrangement of the spatiotemporal patterns of optic flow is preserved and are parsed over large swathes of the visual field by tangential cell interneurons that reside in the lobula plate of the visual ganglia (Fig. 1.3). The most prominent of these neurons have been found to be sensitive to motion in the horizontal and vertical planes [21, 22, 23]. They respond with graded membrane potentials whose polarity depends on motion direction, with the magnitude being highly directionally selective [24, 25]. The directional sensitiv-

ity field has been mapped out in some instances [25] and it has been hypothesized that the optic flow outputs are generated by making a comparison between these sensitivity patterns and the pattern of the visual stimulus with the cells thus acting as matched filters [26, 27].

1.2 Optic Flow-Based Navigation

Biologically inspired approaches for MAV navigation [28] have been studied as an alternative paradigm to traditional computer and machine vision approaches [29, 30]. Seminal work by Srinivasan *et al.* [31, 19] that led to the discovery of honeybee-inspired optic flow heuristics - where optic flow on the left and right retinas were balanced as an insect traversed a narrow corridor - has spawned several similar approaches for MAV navigation [32, 33, 34, 35, 36, 37, 38]. For example, Muratet *et al.* employed a perspective camera in vehicle motion direction to detect frontal obstacles and execute a safe collision avoidance maneuver, while Hrabar [38] used a set of stereo cameras to generate depth estimates for lateral obstacle avoidance in an urban environment. Behavioral observations of visual perception in fruit flies [17], which demonstrate obstacle avoidance by turning away from regions of high optic flow, have inspired strategies for centering [39, 40], reflexive obstacle avoidance [41, 42, 43] and terrain following [44, 45, 46] behaviors. Typically, a feedback signal is generated by comparing single points or uniform averages of optic flow to generate continuous control input. One fundamental drawback of some of these approaches is the inability to decouple translational and rotational components of

optic flow, requiring independent estimation of vehicle rotation rates or selecting viewing stations on the camera to cancel those components directly.

Safe obstacle avoidance behavior requires attending to the twin issues of generating accurate self-motion (egomotion) estimates and developing an accurate environment map at the bandwidths required for safe operation. Most research efforts for estimating egomotion and generating an accurate 3D depth map involve comparing a theoretical linear model of time-dependent optic flow patterns to measurements across the camera image as a solution of the least squares problem [47, 48, 49, 50]. Alternatively, algorithms have been developed that generate updates of egomotion estimate and terrain structure in an iterative manner [51], requiring a GPS-IMU enabled initial egomotion estimate. Noise attenuation is accomplished by selecting viewing stations that generate high contrast images for measuring optic flow, requiring feature detection capability [52, 53]. Extended Kalman filters have been used by incorporating vehicle dynamics for generating more accurate estimates, based on a nonlinear optic flow measurement model [54, 52, 55]. Although these efforts to transition behavioral heuristics to engineered systems provide a path forward, they typically involve feature detection and tracking algorithms that impose high computational cost and largely ignore the processing and feedback mechanisms that insects employ to extract information and regulate behavior. Alternative path planning strategies such as simultaneous localization and mapping (SLAM) algorithms - which involve computing vehicle pose, proximity and velocity from successive tracking of a vast amount of select environment features as well as generating an accurate map of the environment from camera images [56, 57] - and receding horizon

model-based predictive control approaches, which utilize optimization strategies for trajectory generation at each instant, are also computationally expensive requiring significant payload, necessitating offboard processing.

The insect visuomotor system was first explored by Franz *et al.* [32] as a source for generating egomotion estimates necessary for obstacle avoidance applications. A linear model of optic flow was derived and selected weightings, that match the apparent motion induced by certain modes of egomotion, were used to filter the time dependent optic flow patterns to generate relevant motion cues. Loop closure using the filtered outputs was addressed by Humbert *et al.* [58, 59, 60], wherein a mathematical formalism - the technique of *Wide Field Integration* - was introduced to analyze flight behavior. Spatial decomposition of optic flow patterns can be used to detect imbalance and shift in the optic flow pattern arising from changes in velocity and proximity to obstacles in the environment. Traditional controller framework can then be used in generating stabilising commands that regulate optic flow pattern to typical patterns such as a simple sine wave that is induced across the imaging surface by planar motion in a corridor. This framework thus helps generate rapid compensatory commands to regulate flight behavior between obstacles.

Insects mitigate noise inherent in optic flow computation by implementing wide-field spatial integration across large areas of the visual field [14, 13, 25]. Safe stabilisation and obstacle avoidance behavior is achieved by extracting relative proximity and velocity information and using feedback with descending cell neurons transmitting tangential cell outputs to the the flight motor governing wing kinematics [61]. The primary advantage of WFI is computational simplicity and does not

require visual feature detection, tracking and classification. The approach leverages the fact that valuable information encoded by the spatial structure of optic flow patterns can be extracted by weighting these patterns with a set of well-chosen sensitivity functions which are then reducible to just a handful of stabilising control inputs via feedback of optic flow. This is a promising approach for micro-systems with limited processing capabilities and is extrememly robust to noise.

1.3 MAV Controller Framework

The typical control architecture utilizing optic flow feedback for safe obstacle avoidance behavior is shown in Fig. 1.4. The vehicle state $\mathbf{x}$ is sought to be regulated to the desired state $\mathbf{x}_{\text{ref}}$ by using the feedback control law, which actuates the vehicle's control inputs to provide appropriate stabilising commands for good tracking. Appropriate design of the feedback control law assumes accurate knowledge of the vehicle state $\mathbf{x}$. In the absence of a certain required state not being directly estimated from optic flow sensor outputs, the state estimation block generates the required estimates $\hat{\mathbf{x}}$ from available measurements. The estimator and the controller block assume knowledge of the vehicle dynamics, given by a set of either linear or nonlinear ordinary differential equations.

Safe reflexive navigation behavior in an uncertain environment requires generating stabilising commands based on an accurate environment map and vehicle state estimate. Thus the twin issues of environment mapping and localization needs to be addressed in a computationally efficient manner. The objective of generat-

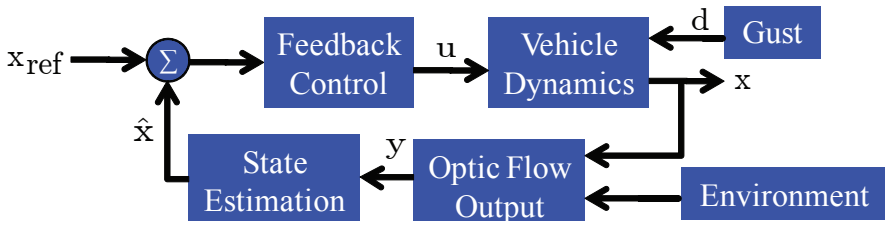

Figure 1.4: Typical feedback architecture for MAV navigation.

ing a depth map, which require computationally expensive feature detection and tracking algorithms, is replaced with the objective of generating estimates of vehicle proximity to an obstacle-symmetric path through the environment, a feature that is independent of environment structure, by allowing for a degree of uncertainty in the local environment map. Additionally, optic flow is used to generate vehicle pose and velocity estimates, eliminating the need for GPS-IMU enabled estimates. The framework outlined in this dissertation utilizes tools from control theory for model-based controller synthesis to obtain pose, proximity and velocity information in a gusty, complex, obstacle laden environment by employing feedback of optic flow. Better visual navigation performance results from efficient processing of optic flow information together with design for stability and navigation, which are closely intertwined. This research specifically addresses these issues and reduces the requirements of mapping and localization through the design of feedback gains using computationally efficient control and estimation algorithms for accurate state estimation in the presence of uncertainties, while generating stabilising commands that ensure good command tracking and gust mitigation characteristics.

The controller synthesis framework outlined in this dissertation has wide ap-

plication in the area of safe reflexive navigation. The current approach is equally well suited to the design of feedback gains using a wide array of distributed and point sensing apparatus such as the artificial lateral line system for proximity detection and prey localization found in fish, or the mechanosensory hair array system for flight stabilization found on insects.

1.4 Dissertation Contributions and Organization

The main contributions are listed below:

- Most approaches have considered visual navigation in an ad-hoc manner using a narrow field of view, with no explicit demonstration of stability. In contrast, the current approach uses a wide field of view to demonstrate safe navigation behavior using traditional control architecture that includes demonstration of stability.

- Safe obstacle avoidance and terrain following behavior require detailed knowledge of the local environment. Most prior approaches assume prior knowledge of an environment and hence are not suitable for navigating through an unknown environment. In contrast, the current approach seeks to develop navigation algorithms for safe flight in a cluttered, obstacle-laden environment that is subjected to gusts.

- Safe reflexive navigation behavior requires accurate extraction of vehicle state and the local environment map. Most prior approaches have utilized computationally expensive algorithms for the purpose, rendering them unsuitable for

MAVs. In contrast, the current bio-inspired approach seeks to extract vehicle pose, proximity and velocity in a computationally efficient manner that is suitable for implemention on an MAV.

The dissertation is organized as follows. Chapter 2 presents the development of the optic flow model and the technique of wide-field integration, which is used to extract relevant motion cues from spatiotemporal patterns of optic flow for both planar and 3D navigation applications. A typical urban environment is parameterized as a family of simplified environments, and optimal patterns for extracting proximity and velocity estimates are developed that minimise noise and uncertainty throughput relative to those environments. Chapter 3 addresses the H_∞ controller synthesis framework for design of feedback gains for good noise attenuation and gust mitigation characteristics resulting in safe planar and 3D navigation in the presence of gusts and environmental uncertainties. Robust stability is explicitly demonstrated for navigation in the urban environment with structural uncertainty. The resulting framework is applied to an aerial micro-system and simulation-based validation studies are carried out to demonstrate safe reflexive navigation behavior for both planar and 3D applications in an urban-like environment in chapter 4. Also, results are presented that demonstrate improvement in closed loop performance and bandwidth using the feedback gains developed from the loop shaping approach for planar navigation applications in chapter 4. Additionally, the controller synthesis framework is shown to result in low order dynamic gains that are physically realizable on a flying micro-system. Results that extend the mapping between optic

flow estimates and actuator commands to incorporate dynamic controllers are also presented. Chapter 5 introduces the hair mechanosensory system for use as an alternative to dynamic controller framework for urban navigation, and the wide-field integration technique is used to generate relevant motion cues for planar and 3D navigation applications. Static compensation is employed and simulation studies are undertaken for the use of the mechanosensory arrays in conjunction with the optic flow outputs for two different applications - as a stability augmentation system for planar motion in a corridor and as a gust rejection system for 3D urban navigation application. A biomimetic sensorimotor architecture is developed that is patterned on the insect visuomotor system. The hair sensor arrays are shown to help improve system performance and bandwidth, by helping overcome limitations of the optic flow outputs for planar navigation. Additionally, hair sensor arrays are shown to provide accurate relative wind velocity estimates, and simulation studies are carried out to study the efficacy of the hair sensor system for the purpose of gust rejection in 3D urban navigation applications. Conclusions, limitations and areas of future work are discussed in Chapter 6.

Chapter 2

Review of Bio-Inspired Information Extraction from Optic Flow

In this chapter, the mathematical formalism of the technique of *wide-field integration* (WFI) is presented as an information extraction procedure from instantaneous patterns of optic flow. Previous efforts using WFI have either involved an ad-hoc analytical approach or have been restricted to analysis in known simplified planar environments. This chapter seeks to extend the use of WFI to both planar and 3D unmapped environments, and the information extraction approach will be presented as part of the controller synthesis framework outlined in the previous chapter. The idea is to use spatial decomposition of instantaneous optic flow patterns to generate navigationally relevant motion cues. Towards that end, an optic flow model is developed based on the parameterization of a set of expected 3-D environments. Small perturbation techniques are then applied to the optic flow output model, which are a function of motion cues such as relative proximity and velocity with respect to the parameterized environments. Weighting patterns that link motion cues to the optic flow outputs are then generated.

2.1 Review of Spherical Optic Flow

True optic flow refers to the angular velocity field induced by the movement of images of objects in the environment that are projected onto the spherical retina.

The velocity field depends on the geometry of the retinal surface, motion and the spatial distribution of objects in the environment. Optic flow encodes relative motion cues as it is a consequence of relative motion of material points in the environment. Optic flow cannot be measured directly, and estimation algorithms typically involve comparing spatiotemporal patterns of luminance over successive camera frames from an image sequence.

Mathematically, optic flow is the tangential component of the relative velocity vector of material points in the environment projected into the imaging surface (Fig. 2.1). In a stationary environment, it is a function of observer translational and rotational motion, along with relative proximity to surrounding objects. If the optic flow field and the spatial distribution of objects in the environment are modeled as a continuous function of the body-referred viewing angles γ and β, denoting azimuth and elevation respectively, the optic flow field $\dot{\mathbf{Q}}$ on a spherical surface S^2 can be written as [20]

$$\dot{\mathbf{Q}}(\gamma,\, \beta,\, \mathbf{x}) = -\boldsymbol{\omega} \times \mathbf{r} - \mu(\gamma,\, \beta,\, \mathbf{q})[\mathbf{v} - \langle\, \mathbf{v},\, \mathbf{r}\rangle \mathbf{r}]\,, \tag{2.1}$$

where $\dot{\mathbf{Q}} = \dot{Q}_\gamma \hat{\boldsymbol{\gamma}} + \dot{Q}_\beta \hat{\boldsymbol{\beta}}$ has components along the azimuth and elevation directions. $\boldsymbol{\omega}$, $\mathbf{v}$ are respectively the rotational and translational velocity of the vantage point, $\mu(\gamma,\, \beta,\, \mathbf{q}) = 1/d(\gamma,\, \beta,\, \mathbf{q})$ is the nearness function representing the distribution of objects in the surrounding environment, $d(\gamma,\, \beta,\, \mathbf{q})$ is the radial distance to the nearest object in the environment at the viewing station $\mathbf{r}(\gamma,\, \beta)$ and $\mathbf{q}$ is the observer pose with respect to the environment. The optic flow model is dependent on the observer state $\mathbf{x} = (\mathbf{q},\, \dot{\mathbf{q}})$, with $\dot{\mathbf{q}}$ being the relative velocity in the body frame.

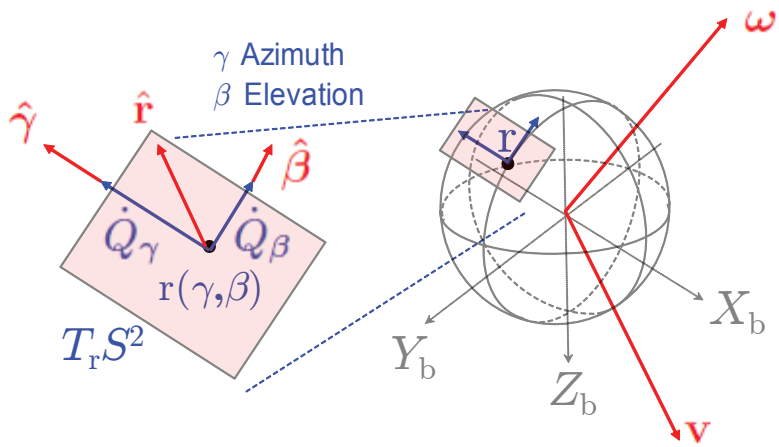

Figure 2.1: Spherical optic flow. Optic flow is the projection of relative velocity on the tangent plane T_rS^2 of the sphere.

Given the components of the translational and rotational velocity $\mathbf{v} = \{u,\, v,\, w\}$, $\boldsymbol{\omega} = \{p,\, q,\, r\}$ in the body frame $\mathcal{B} = \{X_\mathrm{b},\, Y_\mathrm{b},\, Z_\mathrm{b}\}$, the azimuthal and elevation components of optic flow can be shown to be

$$\begin{aligned}
\dot{Q}_\gamma &= p\cos\beta\cos\gamma + q\cos\beta\sin\gamma - r\sin\beta + \mu(u\sin\gamma - v\cos\gamma) \\
\dot{Q}_\beta &= p\sin\gamma - q\cos\gamma + \mu(-u\cos\beta\cos\gamma - v\cos\beta\sin\gamma + w\sin\beta) \qquad (2.2)
\end{aligned}$$

The optic flow vector as derived above assumes the complete spherical surface to be available for measurement, which is appropriate for 3-dimensional motion of the 6DOF vehicle. However, navigational quantites of interest can also be obtained by considering optic flow over smaller domains. For motion restricted to a plane, the spherical optic flow components (2.2) can be reduced to planar optic flow for the yaw ring. If the yaw ring is aligned with the body axis of the vehicle, then for planar motion of the 3DOF vehicle, the yaw-ring specific optic flow field is obtained for the case $\beta = \frac{\pi}{2}$, and is given by,

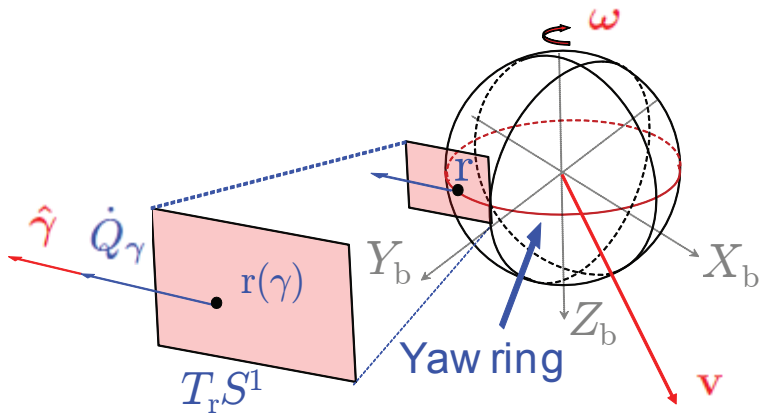

Figure 2.2: Planar optic flow. Optic flow is the projection of relative inplane velocity on the tangent plane T_rS^1 of the yaw ring.

$$\dot{Q}_\gamma \quad = -r + \mu(u \sin\gamma - v \cos\gamma) \tag{2.3}$$

where the nearness function μ respresents the spatial distribution of surrounding objects in the constrained plane.

2.2 Parameterization of the Urban Environment

The nearness function is assumed to be bounded and piecewise continuous with a finite number of discontinuities. Simplifying assumptions are required on the shape of the nearness function $\mu(\gamma,\, \beta,\, \mathbf{q})$ to completely characterise the optic flow pattern (2.2) in closed form. The vehicle pose is given by $\mathbf{q} = \{x,\, y,\, z,\, \phi,\, \theta,\, \psi\}$, where $(x,\, y,\, z)$ are the vantage point coordinates in the inertial frame $\mathcal{F} = \{X,\, Y,\, Z\}$, and $(\phi,\, \theta,\, \psi)$ are the 3-2-1 Euler angles, representing the attitude of the body frame $\mathcal{B}$ relative to $\mathcal{F}$. Assume the environment to be a cube enclosing the viewing surface

(Fig. 2.3a), with the reference position of the vehicle represented by the distance of the vehicle to the walls in the various directions, denoted by a_E, a_W, g_N, g_S, h_U, h_D. The deviation from this reference state is captured by the proximity quantities along the three orthogonal directions (x, y, z). For this environment model, the nearness function can be shown to be a piecewise continuous function given by

$$\mu(\gamma,\, \beta,\, \mathbf{q}) = \begin{cases} \dfrac{\sin\beta[\cos\psi\cos\theta\cos\gamma+\sin\gamma(\sin\phi\sin\theta-\cos\phi\sin\psi\cos\theta)]+\cos\beta(\sin\phi\sin\psi\cos\theta+\cos\phi\sin\theta)}{g_N-x} & \text{north} \\ -\dfrac{\sin\beta[\cos\psi\cos\theta\cos\gamma+\sin\gamma(\sin\phi\sin\theta-\cos\phi\sin\psi\cos\theta)]+\cos\beta(\sin\phi\sin\psi\cos\theta+\cos\phi\sin\theta)}{g_S+x} & \text{south} \\ \dfrac{\sin\beta(\cos\gamma\cos\theta\sin\psi+\sin\gamma[\sin\phi\sin\theta\sin\psi+\cos\phi\cos\psi])+\cos\beta(\cos\phi\sin\theta\sin\psi-\sin\phi\cos\psi)}{a_E-y} & \text{east} \\ -\dfrac{\sin\beta(\cos\gamma\cos\theta\sin\psi+\sin\gamma[\sin\phi\sin\theta\sin\psi+\cos\phi\cos\psi])+\cos\beta(\cos\phi\sin\theta\sin\psi-\sin\phi\cos\psi)}{a_W+y} & \text{west} \\ \dfrac{\sin\beta(\sin\phi\cos\theta\sin\gamma-\sin\theta\cos\gamma)+\cos\beta\cos\phi\cos\theta}{h_D-z} & \text{ground} \\ -\dfrac{\sin\beta(\sin\phi\cos\theta\sin\gamma-\sin\theta\cos\gamma)+\cos\beta\cos\phi\cos\theta}{h_U+z} & \text{ceiling} \end{cases}$$

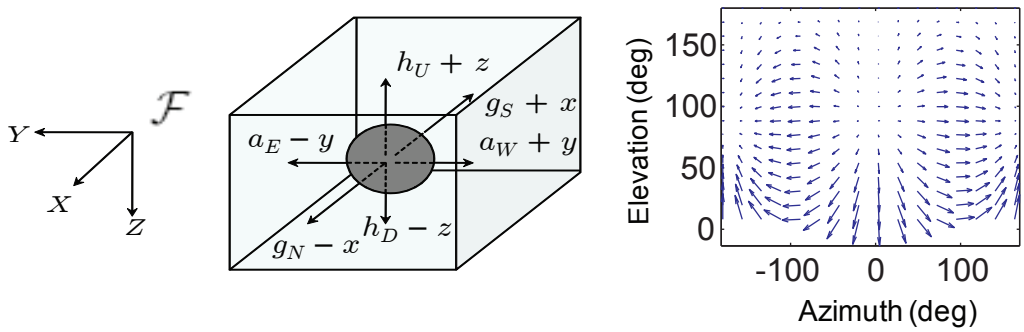

Figure 2.3: (a) 3-D environment parameterization; (b) Nominal optic flow pattern.

The derivation of the nearness function above has previously been presented in detail [62]. Owing to numerical complexity, the bounds on the nearness function,

specifying the location of intersection of the various surfaces, and hence the optic flow components are computed numerically. The generic environment described above can be simplified to environments useful for outdoor navigation. It is pertinent to note the continuous variation of the nearness function as a function of the nominal wall distance in various directions. A typical urban environment can now be modeled as a series of limiting cases, where each limiting case represents one extremum of the family of modeled environments. Flight past a left sided wall with a minimum nominal wall clearance of a_W is modeled by the case for which $(a_E,\, g_N,\, g_S,\, h_U) \to \infty$. Similarly, if there is an east side obstacle with a designated nominal clearance of a_E, then $(a_W,\, g_N,\, g_S,\, h_U) \to \infty$. For the case with obstacles at equal distances on both sides (nominal clearance a), $a_E = a_W = a$, $(g_N,\, g_S,\, h_U) \to \infty$. Parameterization of the environment in this manner then requires that the design the feedback loop provide stability for the set of limiting cases. Demonstrating robust stability of a vehicle to the set of limiting environments then translates to the vehicle being stable when traversing the urban environment. This is the central idea behind the design of the stable feedback controller, which is demonstrated in Chapter 4.

The nominal optic flow pattern for a vehicle flying at a constant forward speed in a composite environment obtained as an unweighted mean of the above three environments is shown in Fig. 2.3b.

For motion restricted to the horizontal plane, the nearness function can be simplified as,

$$\mu(\gamma, \mathbf{q}) = \begin{cases} \frac{\sin(\gamma+\psi)}{a_W - y}, & 0 \leq \gamma + \psi \leq \pi\,, \\ -\frac{\sin(\gamma+\psi)}{a_E + y}, & \pi \leq \gamma + \psi \leq 2\pi\,. \end{cases}$$

2.3 Measurement Model with Environment Uncertainty

The tangential cells of insects reside in the lobula plate which pool vast quantities of optic flow patterns and respond with graded membrane potentials whose magnitude is highly directionally selective [24, 25], with the response being depolarizing if the motion is progressive and hyperpolarizing if the motion is regressive. The optic flow outputs are generated by making a comparison between the preferred sensitivity pattern of the tangential cell interneurons and the pattern of the visual stimulus [26, 27], with the output being modeled as an inner product $\langle \mathbf{a}, \mathbf{b} \rangle$ of two vectors, representing the projection of $\mathbf{b}$ along $\mathbf{a}$ or vice-versa. As a consequence, patterns that are orthogonal to one another generate null output. For 3-D motion, the patterns $\dot{\mathbf{Q}}$ are assumed to reside in $L_2(S^2, \mathbb{R}^2)$, the vector-valued space of piecewise continuous and square-integrable functions on the sphere S^2, given by,

$$L_2(S^2,\, \mathbb{R}^2) = \left\{ \mathbf{f} = \begin{bmatrix} f_1(\mathbf{r}) \\ f_2(\mathbf{r}) \end{bmatrix} : \mathbf{r} \in S^2,\; f_k(\mathbf{r}) \in L_2(S^2),\; k = 1,\, 2 \right\}$$

The matched filter concept can then be mathematically written as

$$\langle \dot{\mathbf{Q}}, \mathbf{F}(\gamma,\, \beta) \rangle = \int_{S^2} \dot{\mathbf{Q}} \,.\, \mathbf{F}(\gamma,\, \beta)\, d\Omega. \tag{2.4}$$

$\mathbf{F}(\gamma,\, \beta) = F_\gamma \hat{\boldsymbol{\gamma}} + F_\beta \hat{\boldsymbol{\beta}}$ represents any piecewise continuous, square-integrable weighting function, . denotes the dot product in $\mathbb{R}^2$, $d\Omega = \sin\beta d\beta d\gamma$ represents the solid angle of the sphere and the output resulting from the comparison represents the

decomposition of the motion field into state perturbations from the desired pattern [26].

Real spherical harmonics, being orthogonal functions on $L_2(S^2)$, are particularly well suited for use as weighting functions along the azimuthal and elevation directions. These functions are given by:

$$Y_{l,m}(\gamma,\, \beta) = N_l^m \Phi_l^m(\cos\beta) \begin{cases} \cos m\gamma & m \geq 0\,, \\ \sin |m|\gamma & m < 0. \end{cases}$$

where $\Phi_l^m(\cos\beta)$ is the associated Legendre function, $\{l,\, m\} \in \mathbb{Z}$ with $l \geq 0$, $|m| \leq l$, and N_l^m is the normalization coefficient. The optic flow outputs representing the spatial decomposition of the optic flow patterns for component weighting functions $\mathbf{F}_{l,m}^k = Y_{l,m}\hat{\mathbf{k}}$ for $k \in \{\gamma,\, \beta\}$ are then given by,

$$y_{l,m}^k(\mathbf{x}) = \int_0^{2\pi} \int_0^{\pi} \dot{Q}_k(\mathbf{x}) Y_{l,m}^k \sin\beta \, d\beta \, d\gamma \tag{2.5}$$

For the case of a vehicle undergoing planar motion while traversing the length of a corridor (half width a) with a reference forward velocity u_0, with perturbations in the lateral direction and about the yaw axis, the planar optic flow outputs $y_{a_0}, y_{a_1}, y_{a_2}$ and the corresponding linearized terms are listed in table 2.1 [26, 59]. It is pertinent to note that the optic flow outputs negatively couple lateral velocity $\dot{y}$ and heading ψ (y_{a_1} in table 2.1) and hence couple the lateral and yaw dynamics. This imposes severe limitations on the closed loop performance as the poles of the linear system can no longer be placed arbitrarily. This limitation is a characteristic feature of planar optic flow outputs. The optic flow outputs for the case $a_E \neq a_W$ can be

Table 2.1: Inertial planar optic flow outputs $y(\mathbf{x})$ ($a_E = a_W = a$)

Sensitivity pattern, $F(\gamma)$	WFI sensory output	Linearization
1	$y_{a_0} = -\sqrt{2}r + \frac{y}{\sqrt{2}(a^2-y^2)}u$	$-\sqrt{2}r + \frac{u_0}{\sqrt{2}a^2}y$
$\cos\gamma$	$y_{a_1} = \frac{4a}{3\pi(a^2-y^2)}(2u\sin\psi - \dot{y}\cos\psi)$	$\frac{4}{3\pi a}(2u_0\psi - \dot{y})$
$\cos 2\gamma$	$y_{a_2} = -\frac{y}{2(a^2-y^2)}(u\cos 2\psi + \dot{y}\sin 2\psi)$	$-\frac{u_0}{2a^2}y$

derived in a manner similar to the outputs shown in table 2.1. Safe planar navigation in an uncertain environment compounded by gusts then requires the development of estimation and control algorithms that helps generate estimates of the coupled inplane states. State feedback then allows for placement of poles in an optimal manner. This is one of the basic objectives of current research, which is undertaken in Chapter 3 which deals with feedback loop design.

Optic flow is inferred indirectly from spatiotemporal patterns of luminance incident on the spherical imaging surface. The optic flow estimation process then introduces errors in measurements that is further corrupted by sensor noise as well as contrast and texture variations in the environment. Furthermore, variation in the distribution of obstacles in the surrounding environment, characterised by the the nearness function, adds uncertainty to the measurement model. Given $p \geq n$ spherical harmonics $\mathbf{F} = \{\mathbf{F}_j,\ j = 1...p\}$, for small perturbations about the reference flight condition $\mathbf{x}_{\text{ref}}$, the linear optic flow outputs - accounting for environment uncertainty and measurement noise - can be written in the form

$$\tilde{\mathbf{y}} = C\mathbf{x} + \mathbf{w};\ C = C_{\text{m}} + \Delta C \tag{2.6}$$

where, $\tilde{\mathbf{y}} \in \mathbb{R}^p$ are the measured optic flow outputs, the noise $\mathbf{w}$ is zero mean $E\{\mathbf{w}\} = 0$ with known covariance $E\{\mathbf{w}\mathbf{w}^T\} = R_{\mathbf{w}}$. The quantity ΔC is assumed to be zero mean random perturbation $E\{\Delta C\} = 0$, which captures the variation in the nearness function $\mu(\gamma,\, \beta,\, \mathbf{q})$ from the baseline environment. Furthermore, it is assumed that $E\{\mathbf{w}\Delta C^T\} = 0$. The quantity C_{m} is approximated as an unweighted average of the three cases described in section 2.2:

$$C_{\mathrm{m}} = \frac{1}{3}[C(a_E = 1, a_W = \infty) + C(a_E = \infty, a_W = 1) + C(a_E = 1, a_W = 1)] \quad (2.7)$$

where $a_{E,W} = 1$ m defines the minimum nominal wall clearance or halfwidth of a corridor the vehicle is likely to encounter.

The solution to the static estimation problem of the overdetermined, inconsistent set of linear equations (2.6) is given by the weighted least squares estimator, $C^\dagger = (C_{\mathrm{m}}^T W C_{\mathrm{m}})^{-1} C_{\mathrm{m}}^T W$, which is used to generate optimal estimates $\hat{\mathbf{x}} = C^\dagger \tilde{\mathbf{y}}$ that minimises noise and uncertainty throughput. The weighting matrix W that acts to penalize high measurement noise and environment uncertainty is $W = (R_{\mathbf{w}} + R_{\Delta C})^{-1}$, where $R_{\mathbf{w}}$, $R_{\Delta C}$ represent noise and uncertainty covariance respectively. Optic flow estimates across the imaging surface are assumed to be affected by zero mean additive noise $\boldsymbol{\eta}(\gamma,\, \beta)$ with variance σ_n^2 with no correlation between measurement nodes or with signal amplitude. Measurement noise at the output can then be written as $\mathbf{w} = \langle \boldsymbol{\eta},\, \mathbf{F} \rangle$. Using linearity of the WFI operator (2.4) and the properties of the covariance matrix, we have,

$$R_{\mathbf{w}ij} = \Delta\beta\, \Delta\gamma \sigma_n^2 \langle \mathbf{F}_i,\, \mathbf{F}_j \rangle \quad (2.8)$$

where $\Delta\gamma$, $\Delta\beta$ is the spacing between successive viewing stations along the azimuthal

and elevation directions respectively. For the present application, $\Delta\gamma, \Delta\beta$ are set to 9 deg. The uncertainty covariance matrix $R_{\Delta C}$ is computed as,

$$R_{\Delta C ij} = \sigma_n^2 \sum_{k=1}^{n} \mathrm{Cov}(\Delta C_{ik})(\Delta C_{jk}) \tag{2.9}$$

Based on the model of environments considered in section 2.2, $R_{\Delta C}$ is conservatively approximated using ΔC matrices corresponding to the three limiting cases.

The relative state estimates $\hat{\mathbf{x}}$ are optimal with respect to the span of the basis function set $\mathbf{F}$. Inclusion of spherical harmonics to a high degree is sufficient to achieve convergence to the global optimum over $L_2(S^2, \mathbb{R}^2)$. For the relative state estimates $\hat{\mathbf{x}} = C^{\dagger}\tilde{\mathbf{y}}$ with $\tilde{\mathbf{y}} = \langle \dot{\mathbf{Q}}, \mathbf{F} \rangle$, the linearity of the WFI operator allows computing state estimates using the state extraction pattern $\mathbf{F}_{\hat{\mathbf{x}}}$, given by,

$$\hat{\mathbf{x}} = \langle \dot{\mathbf{Q}}, \mathbf{F}_{\hat{\mathbf{x}}} \rangle, \; \mathbf{F}_{\hat{\mathbf{x}}} = C^{\dagger}\mathbf{F} \tag{2.10}$$

The optimal state extraction patterns are shown in Fig. 2.4. The state extraction patterns could be used to extract motion state estimates (vehicle pose, proximity, velocity, angular rate) that are embedded in instantaneous optic flow patterns, with minimal noise and uncertainty throughput. The state extraction patterns thus act to remove the coupling between non-orthogonal states that impose perturbations on the nominal optic flow pattern (Fig. 2.3b).

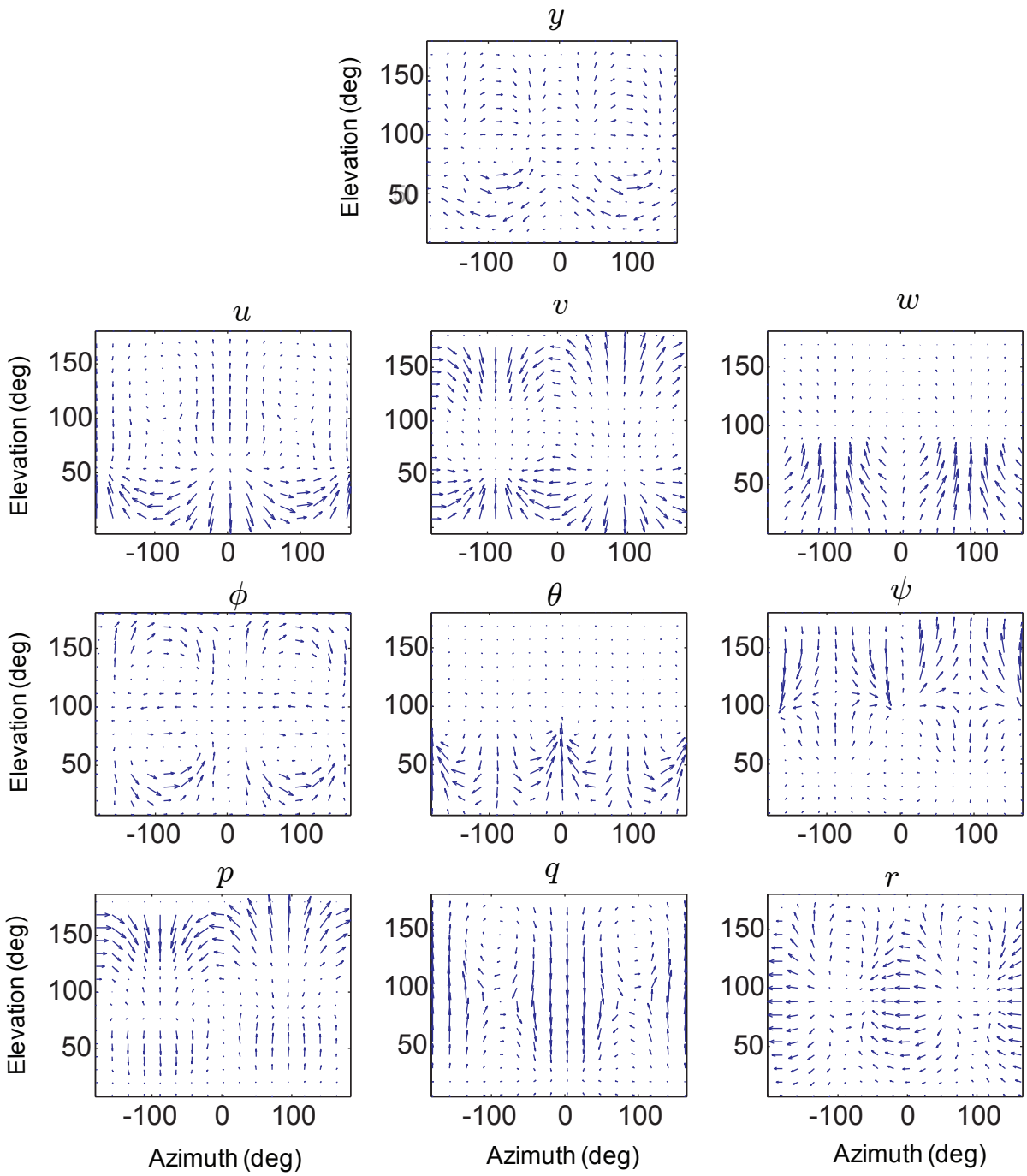

Figure 2.4: Optimum state extraction patterns $\mathbf{F}_{\hat{\mathbf{x}}}$.

Chapter 3

H_∞ Loop Shaping Design

In this chapter, the inner product model for tangential cell analogs previously developed is coupled with the H_∞ loop shaping procedure for designing feedback gains that are robust to environmental uncertainities as well as gusts for safe obstacle avoidance and terrain following behavior. For a vehicle to navigate a gusty environment in a safe manner, the flight controller needs to be designed for good command tracking and gust mitigation. In addition, the vehicle is required to be robustly stable to disturbances associated with a visually uncertain environment. The objective is to regulate relative state estimates $\hat{\mathbf{x}}$ provided by WFI (2.10) to desired reference values $\mathbf{x}_{\text{ref}}$ resulting in safe navigation in an obstacle-laden environment. This chapter presents a feedback design approach that helps achieve the twin objectives of good nominal performance (gust disturbance rejection, command tracking) as well as sufficient robust stability in a simple and straightforward manner. The computationally efficient loop shaping approach results in a feedback gain that is a low-order dynamic controller that is physically realizable onboard an aerial micro-system.

In the first section, a typical dynamic controller framework is presented and the general requirements on the feedback gain for achieving good nominal performance are delineated. Subsequently, the loop shaping framework is developed for planar

navigation in an urban environment. The limitation of planar optic flow, that was outlined in chapter 2, impose unique constraints on optic-flow based planar navigation that require an alternate loop shaping approach to the design of feedback gain. In the final section, the loop shaping framework for a 6DOF vehicle navigating in three dimensional environments is introduced and the process of designing feedback gains for achieving good nominal and robust performance is delineated.

3.1 General Dynamic Controller Framework

The implementation structure of a general dynamic controller framework for MAV navigation applications is shown in Fig. 3.1. The objective is to regulate the plant output $\mathbf{y}$ to the desired output $\mathbf{y}_{\text{ref}}$, in the presence of gust $\mathbf{d}$. The vehicle dynamics is represented by the open loop transfer function G. The plant output $\mathbf{y}$ is corrupted by measurement noise $\mathbf{w}$. The open loop gust transfer function G_{d} links the gust disturbance to the plant output. If the plant is internally stable, the following equation for the closed loop system holds:

$$\mathbf{y} = \frac{GK}{1+GK}\mathbf{y}_{\text{ref}} + \frac{G_{\text{d}}}{1+GK}\mathbf{d} - \frac{GK}{1+GK}\mathbf{w} \tag{3.1}$$

Let the closed loop gust transfer function be defined as $G_{\text{d}_{\text{cl}}} = \frac{G_{\text{d}}}{1+GK}$. As stated, the objective is to design the feedback gain K that helps regulate plant output $\mathbf{y}$ to the desired value $\mathbf{y}_{\text{ref}}$, in the presence of gust $\mathbf{d}$ and measurement noise $\mathbf{w}$. From (3.1), it is apparent that $\mathbf{y}$ approaches $\mathbf{y}_{\text{ref}}$ if good gust mitigation and command tracking characteristics are achieved ($GK >> 1$), together with adequate noise attenuation ($GK << 1$). Gust mitigation and command tracking are neces-

sary only at low frequencies and noise attenuation only at high frequencies. Hence, good nominal performance requires large loop gain (denoted by GK) at low frequency, small loop gain at large frequency and moderate roll-off rate at crossover frequency ensuring good command tracking, gust mitigation and noise attenuation characterisitics [63]. These requirements are summarized in Fig. 3.2.

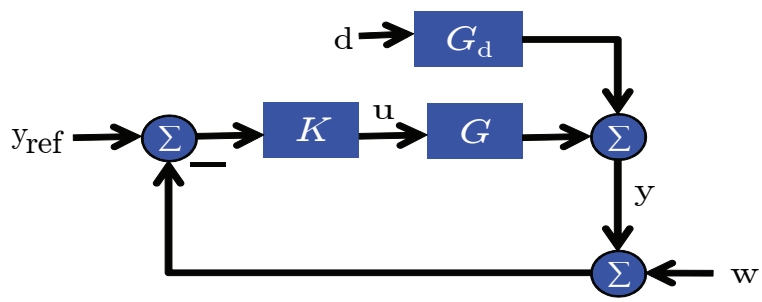

Figure 3.1: Typical feedback control architecture.

3.2 H_∞ Controller Synthesis Framework for Planar Navigation Applications

In this section, based on the general requirements of a feedback gain for good nominal performance, the loop shaping approach to the design of the controller for the specific case of optic-flow based planar navigation in urban environments is looked at. As seen from table 2.1, optic flow outputs couple the inplane states - lateral vehicle velocity $\dot{y}$ with attitude ψ - that necessitates the development of an observer-based loop shaping framework for the design of feedback gains. Unlike the case with three-dimensional navigation where the static estimator $C^\dagger$ links the relative state estimates $\hat{\mathbf{x}}$ to the optic flow outputs $\mathbf{y}$, an exact observer based loop

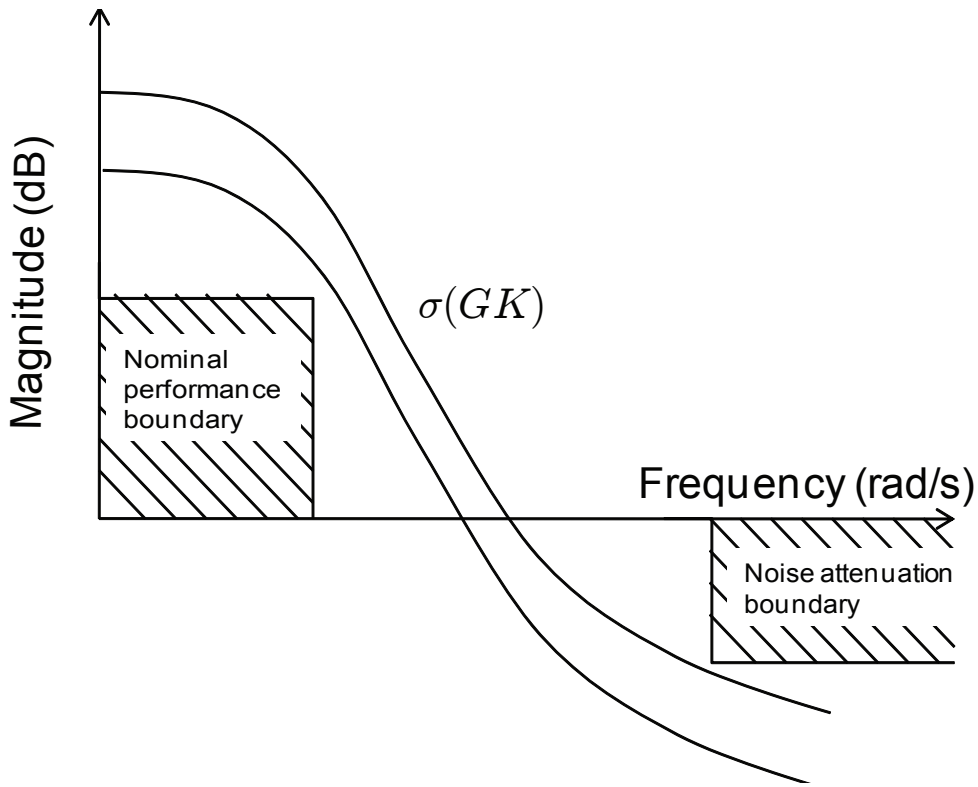

Figure 3.2: Loop gain design specifications.

shaping framework that uses a dynamic model to link outputs $\mathbf{y}$ to estimate $\hat{\mathbf{x}}$ needs to be looked at. For the purposes of feedback controller design, the vehicle is assumed to be governed by the linear dynamics model, given by,

$$\dot{\mathbf{x}} = A\mathbf{x} + B\mathbf{u} + D\mathbf{d}$$

Accordingly, the observer form structure of the loop shaping controller can be written as the combination of an exact plant observer and state feedback controller [64]. For the vehicle dynamics given by (3.2) and the optic flow outputs given by (2.6), the observer form structure of the loop shaping controller for the nominal plant can then be written as

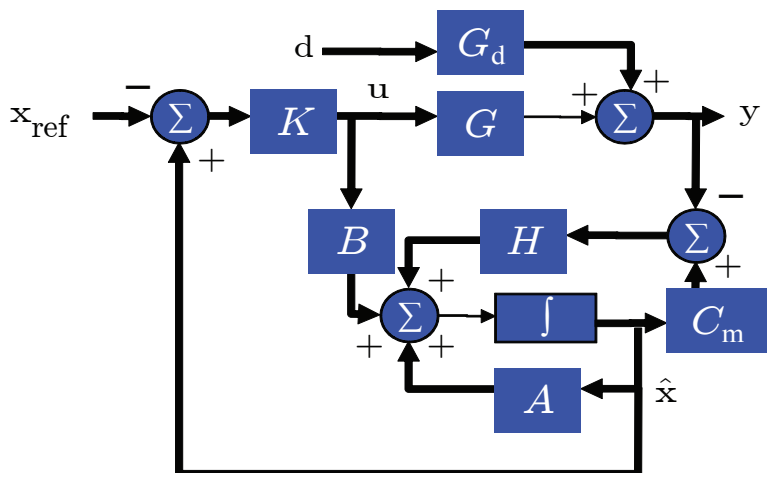

Figure 3.3: Observer form implementation of H_∞ loop shaping controller.

$$\begin{aligned} \dot{\hat{\mathbf{x}}} &= A\hat{\mathbf{x}} + B\mathbf{u} + H(C_{\mathrm{m}}\hat{\mathbf{x}} - \mathbf{y}) \,, \\ \mathbf{u} &= K(\hat{\mathbf{x}} - \mathbf{x}_{\mathrm{ref}}) \,, \end{aligned} \tag{3.2}$$

where $\hat{\mathbf{x}}$ is the state estimate, $\mathbf{u}$ and $\mathbf{y}$ are the plant input and output respectively, and

$$\begin{aligned} H &= -ZC_{\mathrm{m}}^T \,, \\ K &= -B[I - \gamma^{-2}I - \gamma^{-2}XZ]^{-1}X \,, \end{aligned} \tag{3.3}$$

Z and X are solutions of the uncoupled complementary Riccati equations

$$\begin{aligned} AZ + ZA^T - ZC_{\mathrm{m}}^T C_{\mathrm{m}} Z + BB^T &= 0 \,, \\ A^T X + XA - XBB^T X + C_{\mathrm{m}}^T C_{\mathrm{m}} &= 0 \,. \end{aligned} \tag{3.4}$$

Furthermore, the nominal and the uncertainty plant as well as the gust transfer

functions can be written as

$$\begin{aligned} G &= C_{\mathrm{m}}(sI - A)^{-1}B, \\ \Delta G &= \Delta C(sI - A)^{-1}B\,, \\ G_d &= C_{\mathrm{m}}(sI - A)^{-1}D\,. \end{aligned} \tag{3.5}$$

Robust stability can then be demonstrated by considering the normalised left coprime factorisation of the nominal and the perturbed plant. For the nominal plant G with a left coprime factorisation given by,

$$G = M_l^{-1}N_l, \tag{3.6}$$

an uncertain plant model G_p can then be written as

$$G_p = G + \Delta G = (M_l + \Delta_M)^{-1}(N_l + \Delta_N)\,, \tag{3.7}$$

where Δ_M and Δ_N are stable transfer functions that represent the uncertainty in the nominal plant G. Robust stability can again be demonstrated if the small gain theorem is satisfied, which requires that

$$||M\Delta||_\infty < 1\,, \tag{3.8}$$

where the blocks M and Δ represent the nominal closed loop system and the influence of uncertainty respectively, as shown in Fig. 3.4. The dynamic gain matrix K_∞ can then be easily obtained from (3.2) and can be shown to be

$$K_\infty(s) = -K[sI - (A + BK + HC_{\mathrm{m}})]^{-1}H\,. \tag{3.9}$$

For each of the limiting cases, one can numerically determine Δ_M and Δ_N from

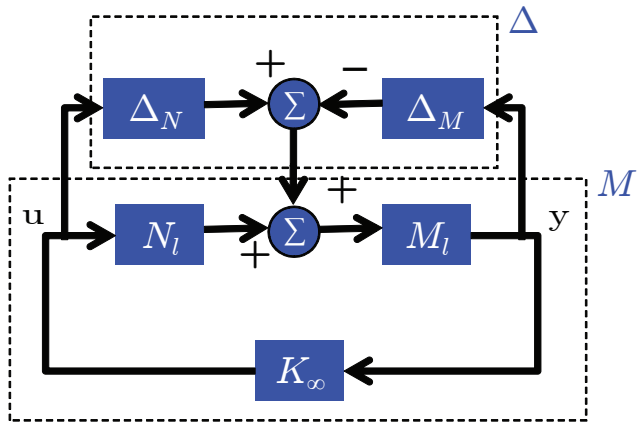

Figure 3.4: Normalized uncertainty coprime factorization.

(3.17), (3.18) and demonstrate (3.19). Satisfaction of (3.19) for each limiting case again ensures robust stability for a more complex urban-like environment. Thus, the control objective is to regulate the relative state estimates provided by the visuo-motor system to reference values, while simultaneously alleviating gust effects and demonstrating robust stability across a range of simplified environments, resulting in stable obstacle avoidance behavior with adequate gust mitigation in a complex, urban-like environment. Leveraging linearity of the WFI operator (2.4), the input sensitivity function $\mathbf{F_u}$ can be written as,

$$\mathbf{F}_u(\gamma,\, s) = K_\infty(s)\mathbf{F}(\gamma)\,. \tag{3.10}$$

These patterns are spatio-temporal in nature and help reduce a large set of distributed optic flow sensor measurements to a handful of actuator commands. $\mathbf{F_u}$ thus helps minimise computational complexity of the H_∞ framework by linking the incident optic flow pattern to the vehicle actuator inputs directly, as seen in Fig. 3.5.The plots of $\mathbf{F_u}$ for a vehicle undergoing planar motion in an urban environment

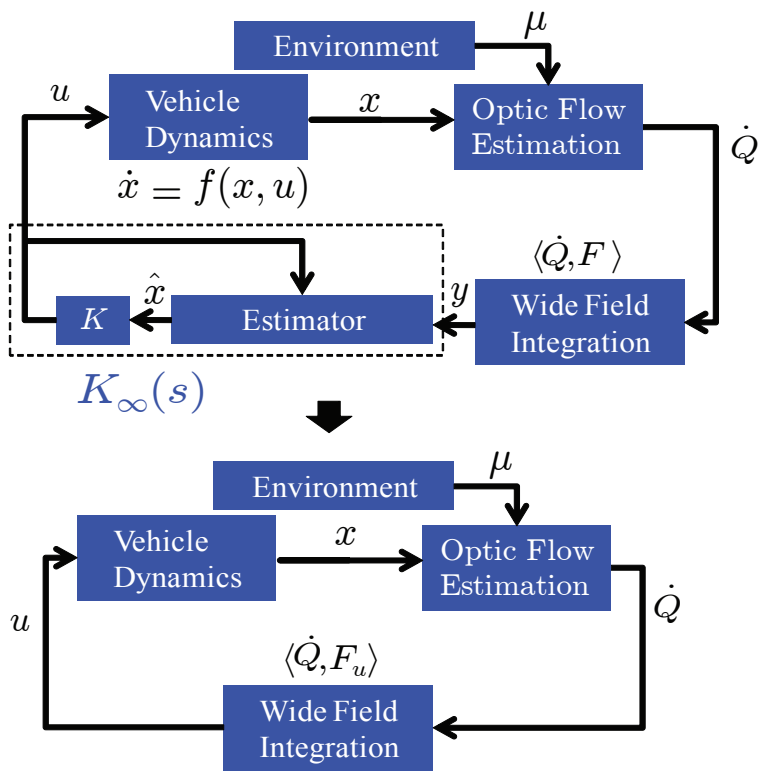

Figure 3.5: Control architecture with dynamic input sensitivity pattern.

are looked at in chapter 4. Additionally, for the observer form structure of the loop shaping controller (Fig. 3.3), the size of the controller K_∞ equals the size of the open loop plant G. This results in a feedback gain that is a low-order dynamic controller that is potentially physically realizable onboard an aerial micro-system.

Finally, the closed loop gust transfer function $G_{\mathrm{d_{cl}}}$, that link the gust disturbance $\mathbf{d}$ to the output $\mathbf{y}$, can be obtained from (3.1) in a straightforward manner,

$$G_{\mathrm{d_{cl}}} = \frac{G_{\mathrm{d}}}{1 - GK_\infty}\,. \tag{3.11}$$

The singular values of $G_{\mathrm{d_{cl}}}$ in the low frequency range provide a measure of the degree of gust mitigation. Smaller the singular values of $G_{\mathrm{d_{cl}}}$, greater the gust

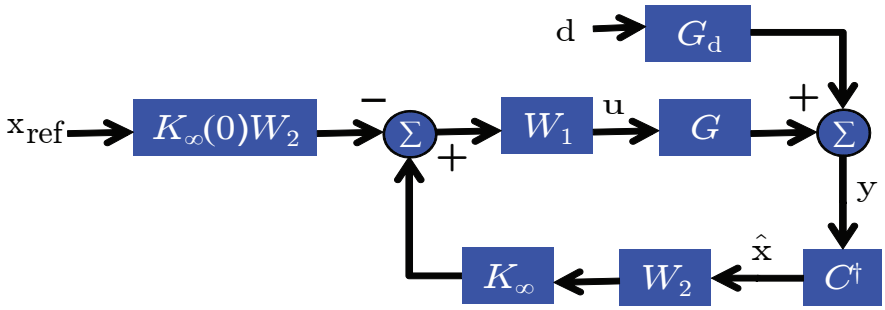

Figure 3.6: Implementation structure of H_∞ loop shaping controller.

attenuation and vice-versa.

3.3 H_∞ Controller Synthesis Framework for Three-Dimensional Navigation Applications

In this section, the loop shaping approach to the design of the feedback controller is undertaken for good nominal and robust performance of a 6DOF vehicle navigating with the aid of optic flow in three dimensional environments. The conventional implementation structure for H_∞ loop shaping controller is shown in Fig. 3.6. The loop shaping approach is essentially a two-stage process. In the first stage, weighting functions W_1 and W_2 are used to shape the singular values of the open loop plant G to achieve desired nominal closed loop performance. The weighting functions are chosen such that the plant attains large gain at low frequency, small gain at large frequency and moderate roll-off rate at crossover frequency ensuring good command tracking, gust mitigation and noise attenuation characterisitics.

The optic flow output equation is given by (2.6). For the aerial micro-system

under consideration, with relative state estimates $\hat{\mathbf{x}}$ as the plant output, the nominal open loop and uncertainty plant as well as gust transfer functions can be written as,

$$\begin{aligned} G &= (sI - A)^{-1}B, \\ \Delta G &= C^{\dagger}\Delta C(sI - A)^{-1}B\,. \end{aligned} \tag{3.12}$$

The transfer functions for the shaped plant are then given by,

$$\begin{aligned} G_s &= W_2(sI - A)^{-1}BW_1, \\ \Delta G_s &= W_2C^{\dagger}\Delta C(sI - A)^{-1}BW_1\,. \end{aligned} \tag{3.13}$$

The next stage involves computation of the controller block K_∞ that robustly stabilises the vehicle in the presence of environmental uncertainties. For the plant G_s with the minimal realisation $[A_s,\, B_s,\, C_s,\, 0]$, the central controller is given by

$$K_\infty = C_\infty(sI - A_\infty)^{-1}B_\infty \tag{3.14}$$

$$\begin{aligned} A_\infty &= A_s + B_sF + \gamma^2(L^T)^{-1}ZC_s^T(C_s), \\ B_\infty &= \gamma^2(L^T)^{-1}ZC_s^T,\, C_\infty = B_s^TX \end{aligned} \tag{3.15}$$

where γ is set to $1.1/\epsilon_{\max}$, $F = -B_s^TX$, $L = (1-\gamma^2)I + XZ$. Z and X are solutions of the uncoupled complementary Riccati equations

$$\begin{aligned} A_sZ + ZA_s^T - ZC_s^TC_sZ + B_sB_s^T &= 0\,, \\ A_s^TX + XA_s - XB_sB_s^TX + C_sC_s &= 0\,. \end{aligned} \tag{3.16}$$

Robust stability can then be demonstrated by considering the normalised left coprime factorisation of the nominal and the perturbed plant. A normalised coprime

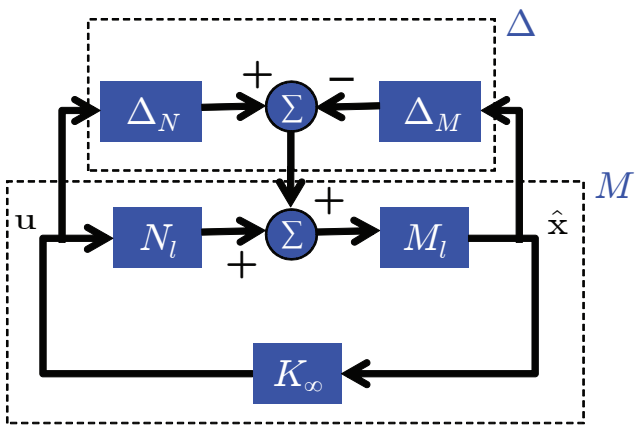

Figure 3.7: Normalized uncertainty coprime factorization.

factorisation for the nominal shaped plant can be written as [65]

$$G_s = M_l^{-1} N_l, \tag{3.17}$$

an uncertain plant model G_p can then be written as

$$G_p = G_s + \Delta G_s = (M_l + \Delta_M)^{-1}(N_l + \Delta_N)\,, \tag{3.18}$$

where Δ_M and Δ_N are stable transfer functions that represent the uncertainty in the nominal plant G_s. Robust stability can then be demonstrated if the small gain theorem is satisfied [66], which requires that

$$||M\Delta||_\infty < 1\,, \tag{3.19}$$

where the blocks M and Δ represent the nominal closed loop system and the influence of uncertainty respectively, as shown in Fig. 3.7. For each of the limiting cases considered in section 2.2, as before, one can then numerically determine Δ_M and Δ_N from (3.17), (3.18) and demonstrate (3.19). Satisfaction of (3.19) for each limiting case then ensures robust stability for a more complex urban-like environment. Thus,

the control objective is to regulate the relative state estimates provided by the visuomotor system to reference values, while simultaneously alleviating gust effects and demonstrating robust stability across a range of simplified environments, resulting in stable obstacle avoidance behavior with adequate gust mitigation in a complex, urban-like environment. This methodology leverages the design philosophy adopted by Hyslop *et al.* [62], where static compensation is employed to regulate relative state estimates generated from the visuomotor system and achieve stable behaviour across a range of different environments.

Finally, it is of interest to consider closed loop gust transfer function $G_{\mathrm{d_{cl}}}$, given by,

$$G_{\mathrm{d_{cl}}} = \frac{C^{\dagger} G_{\mathrm{d}}}{1 - G W_1 K_{\infty} W_2} \,. \tag{3.20}$$

The closed loop gust transfer function links the gust disturbance $\mathbf{d}$ to the relative state estimate $\hat{\mathbf{x}}$. The singular values of $G_{\mathrm{d_{cl}}}$ at low frequency provide a measure of the influence of gust on the relative state estimates, and hence provide a measure of the degree of gust mitigation. Smaller the singular values of $G_{\mathrm{d_{cl}}}$, greater the degree of gust mitigation and vice-versa.

Chapter 4

Validation

In this chapter, simulation-based validation studies are carried out with the dynamic feedback gains designed on the basis of the H_∞ controller synthesis framework for the purposes of achieving safe reflexive navigation behavior. Optic flow estimates provide important motion cues for stabilization and navigation of the vehicle in flight. The spatial decompositions of time-dependent optic flow patterns are coupled with a H_∞ controller to enable a micro-helicopter to autonomously navigate a three dimensional urban-like environment. Both planar and three-dimensional navigation applications are considered. The controller is shown to help the vehicle achieve good nominal and robust performance in the presence of gusts and environment uncertainty, resulting in safe reflexive obstacle avoidance and terrain following behavior.

The vehicle chosen for simulation is the 390g E-Sky hobby helicopter, with a 50.5 cm main rotor diameter and a 14.5 cm tail rotor Fig. 4.1. System identification technique was employed in a prior study to generate the linear flight dynamics model with the U.S. Army's CIFER software package [67]. The vehicle is assumed to be subjected to sustained gust throughout its time of travel. The wind gust model as well as the flight dynamics model for both planar and 3D applications are given below.

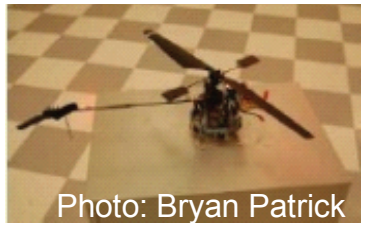

Figure 4.1: Honeybee micro-helicopter.

4.1 Wind Gust Model

The wind gust model for both planar and 3D navigation is derived from the Dryden model, and is obtained as the summation of a large number of sinusoidal excitations,

$$d(t) = \sum_{i=1}^{200} a_i \sin(\Omega_i t + \eta_i)\,, \tag{4.1}$$

where d is the time dependent wind gust vector, and Ω_i, η_i are randomly selected frequencies and phase shifts (uniform distribution assumed with $\eta_i \in [0,\, 2\pi]$) with amplitude a_i. The values of Ω_i are taken in the range 0.05-1.5 rad/s [12]. The amplitude a_i is given by $a_i = \sqrt{\Delta\Omega_i \Phi(\Omega_i)}$, where $\Delta\Omega_i$ is the interval between successive frequencies, and $\Phi(\Omega_i)$ is the power spectral density, given in military handbook MIL-F-8785C and MIL-HDBK-1797 [68, 69]. The gust profiles are shown in Fig. 4.2.

The micro-helicopter encounters a strong gust field with magnitude comparable to the vehicle nominal forward speed of $u_{\text{ref}} = 1$ m/s, causing substantial buffeting and exerting a strong influence on the vehicle dynamics.

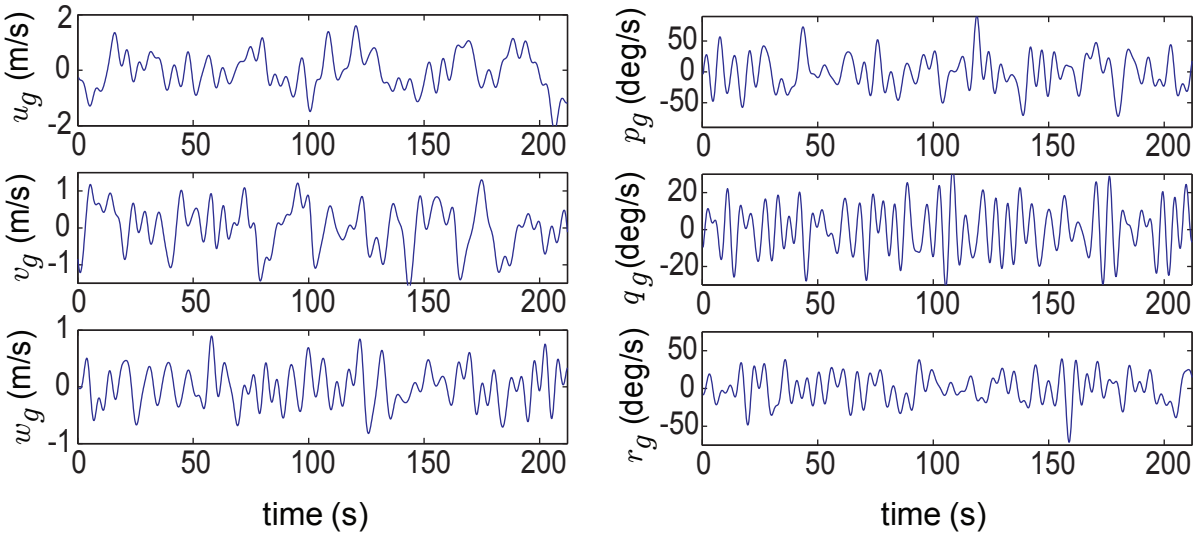

Figure 4.2: Time history of translational and rotational gust.

4.2 Simulation

The simulation environment considered in the present study provides visualization capabilities as well as the ability to compute optic flow from simulated cameras. The virtual micro-helicopter deploys six cameras, each with a 90 × 90 deg field of view and a resolution of 128 × 128 pixels. The cameras cover six sides of a cube, such that the full three dimensional viewing arena is imaged. Aliasing is removed by passing the captured imagery through a Gaussian blurring function that eliminates high frequency noise. The three dimensional image is generated by combining images from the six cameras which is followed by the computation of optic flow using the resolution-iterative Lucas-Kanade algorithm [62] at 60 fps for 800 image points uniformly distributed across the panorama. The points are mapped from the spherical surface to the flat camera surfaces using geometric projection. Spatial averaging and desampling of the resultant optic flow measurements is then

undertaken to reduce noise, with outlier measurements that generate implausibly large shift estimates ignored in the averaging process. The simulation process for planar and 3D navigation are depicted in Figs. 4.4, 4.13.

4.3 Planar Navigation of the Micro-Helicopter

In this section, planar navigation of the micro-helicopter is considered. The task was to enable a micro-helicopter undergoing planar motion to autonomously navigate an urban-like environment using estimates of relative proximity and velocity derived by coupling spatial decompositions of time-dependent optic flow patterns with the obsrever form structure of the H_∞ loop shaping framework (Fig. 3.3). This methodology was used to design feedback gains for the purposes of adequate gust and noise attenuation, good command tracking as well as provide stability for the complex urban-like environment, resulting in safe reflexive obstacle avoidance behavior. Several basic assumptions were made regarding the problem. The side walls and the floor of the environments considered require sufficient texture with adequate lighting conditions for optic flow patterns to be detected. Independent regulation of altitude allows the vehicle motion to remain planar.

4.3.1 Flight Dynamics Model

The vehicle is assumed to travel at an altitude 1 m above ground. Furthermore, a constant forward velocity $u_0 = 1$ m/s is assumed that generates consistent optic flow. The lateral and yaw dynamics of the helicopter subjected to gusts and

linearized about the reference flight condition $\mathbf{x}_{\text{ref}} = [0, 0, 0, 0]^T$ are given by the state equation:

$$\dot{\mathbf{x}} = \mathrm{A}\,\mathbf{x} + \mathrm{B}\,\mathbf{u} + \mathrm{D}\,\mathbf{d}, \tag{4.2}$$

where $\mathbf{x} = [y,\, v,\, \psi,\, r]^T$, $\mathbf{u} = [\phi,\, u_\psi]^T$, $\mathbf{d} = [v_g,\, r_g]^T$, and

$$\mathrm{A} = \begin{bmatrix} 0 & 1 & u_0 & 0 \\ 0 & Y_v & 0 & -u_0 \\ 0 & 0 & 0 & 1 \\ 0 & 0 & 0 & N_r \end{bmatrix}, \mathrm{B} = \begin{bmatrix} 0 & 0 \\ g & 0 \\ 0 & 0 \\ 0 & N_{\mu_y} \end{bmatrix}, \mathrm{D} = \begin{bmatrix} 0 & 0 \\ -Y_v & 0 \\ 0 & 0 \\ 0 & -N_r \end{bmatrix}.$$

y, v are lateral displacement and lateral velocity, ψ and r are vehicle heading and yaw rate respectively, ϕ, u_ψ are the roll and torque inputs to the vehicle respectively and v_g, r_g are respectively the inplane translational and rotational components of gust $\mathbf{d}$ buffeting the vehicle. The body stability derivatives are $Y_v = -0.4799$, $N_r = -0.8786$, $N_{\mu y} = 39.06$, and gravity $g = 9.81$ m/s^2.

4.3.2 Results

For the micro-helicopter under consideration, the observer form structure of the loop shaping controller (Fig. 3.3) results in a stability margin $\epsilon_{\max} = 0.3$, which has been shown to provide adequate gust and noise attenuation as well as good command tracking characteristics [70]. For the resulting feedback gain, the methodology and results are presented for simulation of a helicopter flying in a corridor and an outdoor urban-like environment. The spatial decompostion of optic flow signals coupled with H_∞ loop shaping approach is used to extract sufficient information that

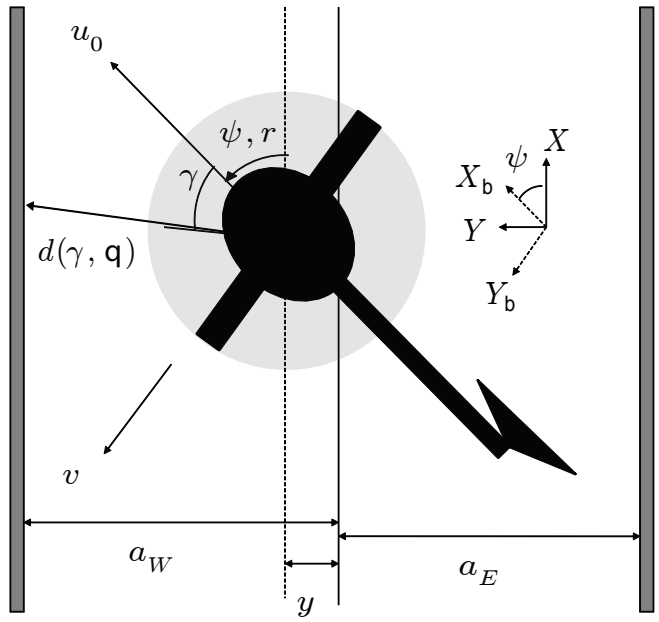

Figure 4.3: Planar corridor coordinate definition.

provides stability and demonstrates safe navigation with the linear vehicle model in the presence of measurement noise, gusts and environmental uncertainty. The simulation process is shown in Fig. 4.4.

4.3.2.1 Corridor Navigation

The flight behaviour of the helicopter is studied for a set of trials chosen with initial perturbations having a mean of $[y_0, v_0, \psi_0, r_0]^T = [0.4\,\text{m},\ 0.18\,\text{m/s},\ 3\,\text{deg},\ 17\,\text{deg/s}]^T$. The simulation of the helicopter flying in a quiescent environment along the length of a corridor (half-width 1.5 m) with no external gusts is constructed. The simulation replicates the actual flight of a micro-helicopter with the dynamics given by (4.3) with the planar optic flow yaw ring attached. The planar optic flow equation as the vehicle navigates the corridor is given by (2.3). The optic flow estimates generated

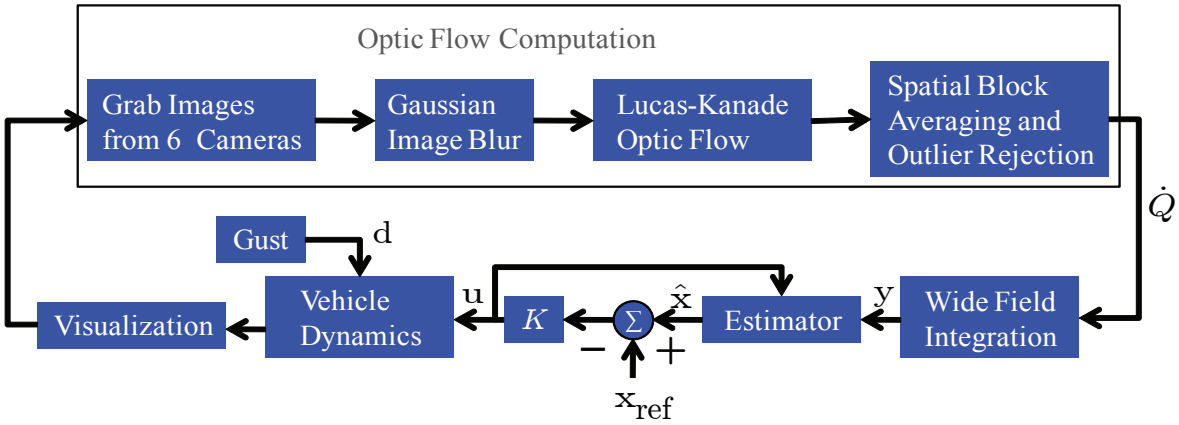

Figure 4.4: Operational flow chart for planar navigation.

by the simulation correspond to true optic flow estimates as the vehicle navigates the length of the corridor, with the attendant characteristics of being nonlinear and embedding noise. A snapshot of the corridor the helicopter navigates in and used in the simulation is shown in Fig. 4.5A.

The results for 20 different trials are as shown in Fig. 4.5B and the time history comparison of the true states and their estimates for a sample trajectory are shown in Fig. 4.6. The time history comparison of the vehicle inplane states shows good convergence between the true states and the corresponding estimates. In particular, the negative coupling between the lateral velocity v and the attitude ψ manifests as a 180° phase difference between the corresponding estimates. Furthermore, from the plots of the closed loop dynamics, we see that the observer form implementation of H_∞ loop shaping controller results in a marked decrease both in the transient decay time and the deviation from the mean - as depicted by the sparse band around the

solid line - in relation to [71]. Hence, there is significant alleviation of the problems of performance and bandwidth limitations associated with optic flow guided planar navigation.

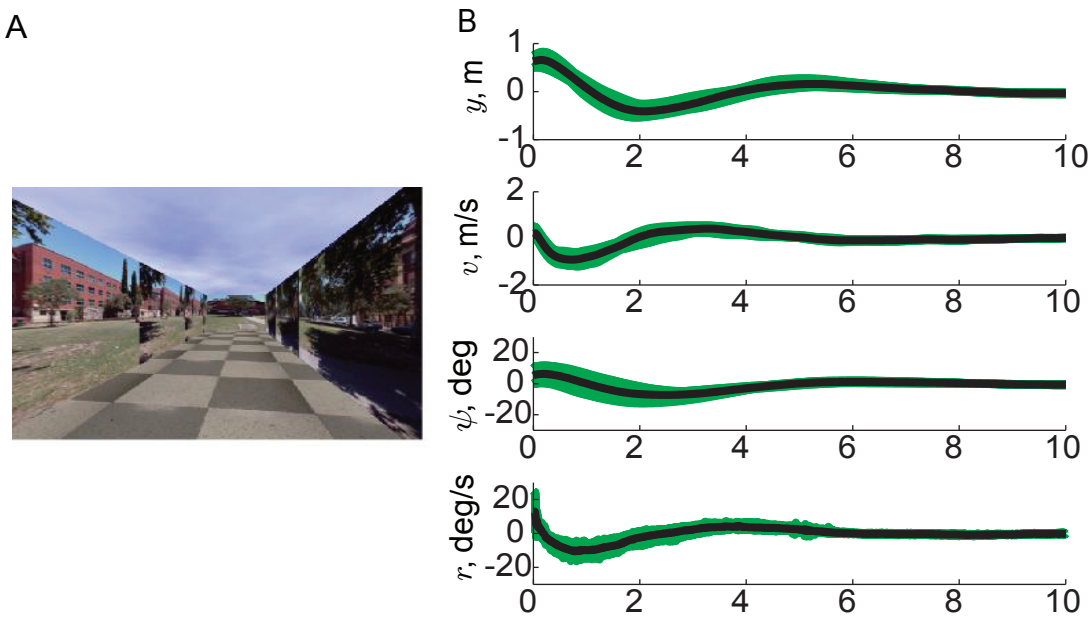

Figure 4.5: (A) Snapshot of the corridor with wall textures used in simulation; (B) Lateral, Yaw dynamics for small perturbations with trajectories (and mean) for 20 trials; Band and solid line represent combined trajectories and mean respectively.

4.3.2.2 Urban Navigation

A snaphot of the urban environment the vehicle traverses in is shown in Fig. 4.7. Fig. 4.12 illustrates the characteristics of the open and closed loop systems. The singular values of the open loop plant are shown in Fig. 4.8A. Large gain at low frequency, moderate roll off rate at crossover frequency and small gain at large frequency result in good nominal response. In particular, Fig. 4.8C illustrates

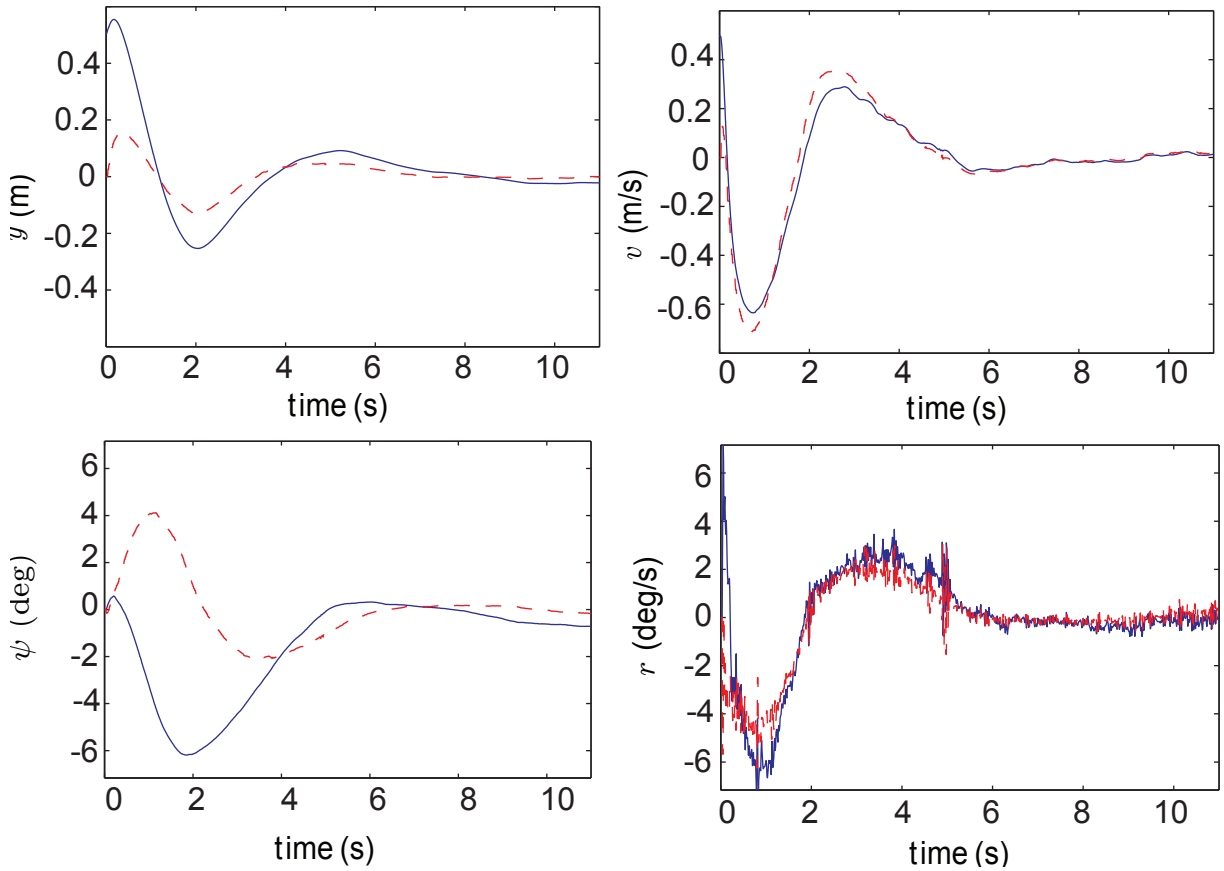

Figure 4.6: Time history comparison of vehicle inplane states; Blue solid line represents true state, red broken line represents state estimate.

the large degree of gust mitigation achieved with the loop shaping gain, as can be seen with small singular values of the closed loop gust transfer function $G_{d_{cl}}$ at low frequency, enabling safe navigation behavior even in the presence of strong gusts. Fig. 4.8B illustrates the concept of robust stability, where (3.19) is satisfied for the three limiting cases considered in section 2.2. The vehicle attempts to track a symmetric path between obstacles in the environment, thus ensuring safe navigation behavior in a complex, cluttered urban-like environment.

Fig. 4.9A shows that in the presence of sustained gust, from 20 different initial

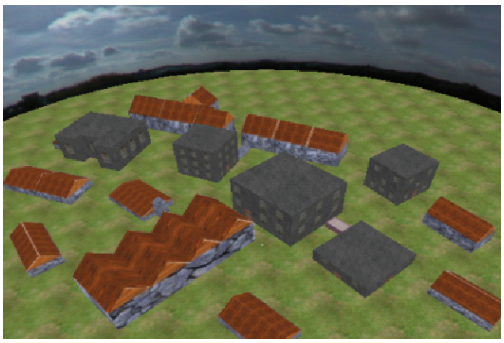

Figure 4.7: Snapshot of the urban-like environment.

headings and locations (X, Y), the helicopter is able to successfully avoid the obstacles in flight. This is achieved almost entirely with optic flow-based measurements, with the exception of a laser rangefinder that is used to sense frontal proximity and initiate emergency turn away from an obstacle when proximity becomes unsafe. This is particularly the case where the probability of a collision with a symmetric obstacle is finite as such trajectories are unstable [72]. There are several close encounters in Fig. 4.9A, with the optic flow system initiating an evasive maneuver resulting in safe navigation behavior in most instances. The instances when the vehicle flies into a symmetric obstacle is rendered safe due to emergency turn initiated by the presence of laser rangefinder. Fig. 4.9B again shows good convergence between the true vehicle velocity states and their corresponding estimates for a sample trajectory. The spikes in the velocity profiles denote instances when the vehicle initiates an emergency turn away from an obstacle directly in front.

4.3.3 Discussion

The results demonstrate that optic flow-guided navigation based on the coupling of spatial decompositions of optic flow patterns with H_∞ loop shaping approach can be used to design a dynamic controller that ensures safe navigation behavior in the presence of environmental uncertainties and strong gusts. The observer form structure of H_∞ loop shaping is used to obtain relative proximity and velocity estimates from measurements of the 2-D optic flow patterns, which are accurate and reliable enough for vehicle stabilization and navigation in an unknown, complex and cluttered environment subjected to gusts. Robust stability is explicitly demonstrated for a family of simple 2-D corridor-like environments which is shown to be sufficient in ensuring safe navigation behavior in more complex environments. For the micro-helicopter undergoing planar motion while flying at a constant forward speed and subject to lateral and yaw perturbations, H_∞ loop shaping results in a low order dynamic controller (2 outputs, 3 inputs and 4 internal states), which is potentially physically realizable on the MAV.

The input sensitivity function, given by (3.10), is completely characterised by the time-domain impulse response and the frequency domain magnitude response plots, as shown in Fig. 4.11. The azimuthal variation of the time invariant plot of the sensitivity function, obtained as a simple time average, is also included. These plots resemble the elementary-motion sensing spatio-temporal action fields obtained from fly figure tracking experiments [73] for regulating flight behavior.

4.4 6 DOF Micro-Helicopter with Spherical Optic Flow

In this section, the dynamics of the 6DOF micro-helicopter is considered and 3D navigation in an urban-like environment is looked at. The task was to enable a micro-helicopter to autonomously navigate the three dimensional environment using estimates of relative proximity and velocity obtained from the visuomotor system and coupling it with the feedback gains resulting from the controller synthesis framework from section 3.3. The objective is to demonstrate good nominal (gust mitigation and command tracking characteristics) and robust performance, thus ensuring safe obstacle avoidance and terrain mapping behavior. The WFI generated state estimates, based on the parameterization of a typical 3-D environments, are shown to be reliable and accurate enough for vehicle navigation in a cluttered environment. The H_∞ controller synthesis framework is used to explicitly demonstrate robust stability for a family of simple 3-D corridor-like environments, and simulation studies of a micro-helicopter in a cluttered arena subjected to gusts demonstrate safe navigation behavior in more complex environments.

4.4.1 Flight Dynamics Model

The 6DOF micro-helicopter vehicle dynamics are again obtained using system identification techniques in a prior study with the U.S. Army's CIFER software package [67]. The vehicle state is given by $\mathbf{x} = \{y,\, z,\, u,\, v,\, w,\, \phi,\, \theta,\, \psi,\, p,\, q,\, r,\, \zeta,\, \chi,\, \Omega_{\mathrm{mr}}\}^T$, with the final three states being the actuator states of the helicopter. The helicopter attains a nominal forward speed of 1 m/s and the vehicle dynamics and kinematics

are linearized about the reference flight condition $\mathbf{x}_{\text{ref}} = \{0,\ 0,\ 1,\ 0,\ -0.05, 0,\ -0.05,\ 0,\ 0,\ 0,\ 0,\ 0,\ 0,\ 0.21\}^T$ for the design of H_∞ feedback controller. The full nonlinear kinematic equations are used for simulation. The dynamics of the helicopter subjected to gusts are given in (4.3). The actuator saturation limits are $|\Lambda_{\text{lat}}| < 1$, $|\Lambda_{\text{lon}}| < 1$, $|\Lambda_{\text{yaw}}| < 1$, $|\Lambda_t| < 0.5$. The characteristic stability derivatives are defined in table 4.1.

$$
\begin{aligned}
\dot{u} &= -g\theta + X_u(u - u_g), \qquad \dot{v} = g\phi + Y_v(v - v_g) - u_{\text{ref}} r \\
\dot{w} &= Z_w(w - w_g) + Z_{\Omega_{mr}}\Omega_{mr} + u_{\text{ref}} q, \qquad \dot{p} = L_v(v - v_g) + L_\zeta \zeta \\
\dot{q} &= M_u(u - u_g) + M_\chi \chi, \qquad \dot{r} = N_r(r - r_g) + N_{\Lambda_{\text{yaw}}}\Lambda_{\text{yaw}} \\
\dot{\zeta} &= -(p - p_g) - \frac{1}{\tau_f}\zeta + \frac{\zeta_\chi}{\tau_f}\chi + \frac{\zeta_{\text{lat}}}{\tau_f}\Lambda_{\text{lat}} + \frac{\zeta_{\text{lon}}}{\tau_f}\Lambda_{\text{lon}} \\
\dot{\chi} &= -(q - q_g) + \frac{\chi_\zeta}{\tau_f}\zeta - \frac{1}{\tau_f}\chi + \frac{\chi_{\text{lat}}}{\tau_f}\Lambda_{\text{lat}} + \frac{\chi_{\text{lon}}}{\tau_f}\Lambda_{\text{lon}} \\
\dot{\Omega}_{\text{mr}} &= T_{\Omega_{\text{mr}}}\Omega_{\text{mr}} + T_{\Lambda_t}\Lambda_t
\end{aligned} \tag{4.3}
$$

The linearized vehicle model is then written as $\dot{\mathbf{x}} = \mathrm{A}\,\mathbf{x} + \mathrm{B}\,\mathbf{u} + \mathrm{D}\,\mathbf{d}$, where $\mathbf{d} = \{u_g,\ v_g,\ w_g,\ p_g,\ q_g,\ r_g\}^T$ is the six-component gust disturbance vector, and A, B, D matrices have their usual meaning. The implementation strucuture of the H_∞ controller framework (Fig. 3.6) is used to design the feedback gain K_∞. The precompensator $W_1(s) = 10s\frac{(s+0.5)}{(s+5)}$ is chosen to add integral action along each input channel which helps improve low frequency command tracking and gust rejection performance. Additional dynamics is included to bring the cut-off to 5 rad/s which is typical for rotorcraft contollers. Postcompensator W_2 is used to provide relative weights to the outputs of the open loop plant, and can be used to help finetune system robust stability as well as control actuation characteristics. The postcom-

Table 4.1: MAV Stability Derivatives

Helicopter stability derivatives	Actuator dynamics derivatives
$X_u = -0.52, Y_v = -0.48$	$\tau_f = 0.15, \zeta_\chi = 1.55$
$Z_w = -0.68, Z_{\Omega_{\mathrm{mr}}} = 0.17$	$\zeta_{\mathrm{lat}} = 0.245,\ \zeta_{\mathrm{lon}} = 0.043$
$L_v = -8.26, L_\zeta = 1273$	$\chi_\zeta = -2.82, \chi_{\mathrm{lat}} = 0.044$
$M_u = 3.6, M_\chi = 341.6$	$\chi_{\mathrm{lon}} = -0.202, T_{\Omega_{\mathrm{mr}}} = -6.182$
$N_r = -0.88, N_{\Lambda_{\mathrm{yaw}}} = 39.06$	$T_{\Lambda_t} = 1449,\ g = 9.81$

pensator was set to $W_2 = \mathrm{diag}(1,\ 4,\ 4,\ 2,\ 4,\ 1,\ 1,\ 2,\ 1,\ 1,\ 1,\ 10^{-15},\ 10^{-15},\ 10^{-15})$ resulting in a stability margin $\epsilon_{\max} = 0.23$, which has been shown to provide adequate gust and noise attenuation as well as good command tracking characteristics [70]. The singular value plots of the open loop and shaped plant are shown in Fig. 4.12A.

The singular values of the loop gain $M\Delta$ for the closed loop incorporating uncertainty for the various limiting cases are shown in Fig. 4.12B. As can be seen from the plot, robust stability is indeed achieved for the family for modeled environments.

4.4.2 Results

In this section, the methodology and results are presented for simulation of the micro-helicopter flying in an outdoor urban-like environment (Fig. 4.7). The simulation replicates the actual flight of a micro-helicopter with the dynamics, given by (4.3), with the spherical optic flow sensor pod attached (Fig. 2.1). The spatial decompostion of optic flow signals coupled with H_∞ loop shaping approach is used

to successfully demonstrate safe navigation behavior in the presence of measurement noise, gusts and environmental uncertainty.

4.4.2.1 Methodology

The proposed methodology assumes that a sonar is available for altitude measurement $\bar{z}$, along with the vehicle actuator states (ζ, χ, Ω_{mr}) for feedback. The estimates of the remaining 10 relative states are generated using the optimal weighting function $\mathbf{F_x} = C^{\dagger}\mathbf{F}$:

$$\hat{x}_i = \langle \dot{\mathbf{Q}},\, \mathbf{F}_{\hat{x}_i} \rangle + C^{\dagger}_{i,\,p+1}\bar{z} \tag{4.4}$$

$\mathbf{F}$ is a $(p+1) \times 2$ matrix representing the component spherical harmonic weighting functions, and the $p+1$ column of $C^{\dagger}$ corresponds to the sonar estimate $\bar{z}$. The desired reference state for the state vector $\mathbf{x}$ is given by

$$\mathbf{x}_{\text{ref}} = (0,\, -K_{z,\theta}(\hat{\theta} - \theta_{\text{ref}}),\, 1,\, 0,\, -0.05,\, 0,\, -0.05,\, 0,\, 0,\, 0,\, 0,\, 0,\, 0,\, 0.21) \tag{4.5}$$

In order to prevent unacceptable speed loss during climb over steep terrain, the target altitude is set as $z_{\text{ref}} = -K_{z,\theta}(\hat{\theta} - \theta_{\text{ref}})$ which is a function of the WFI pitch estimate (providing information of upcoming terrain) relative to its reference value. Furthermore, the range is restricted to (-1, 0) to prevent large vertical velocities. $K_{z,\theta}$ was set to -10 for the simulation studies that follow. Finally, a pitch sensor is assumed to be available for accurate pitch estimates. The simulation process is shown in Fig. 4.13.

To account for variation in the initial conditions, the Monte-Carlo approach is employed. Twenty-three initial locations and headings were generated using a

uniform distribution across the entire layout of the environment, excluding areas covered by buildings.

4.4.2.2 Discussion

Fig. 4.14 shows that in the absence of gust, from all initial conditions, the helicopter is able to successfully avoid obstacles while maintaining a target height of 1 m above ground. This is achieved almost entirely with optic flow-based measurements, with the exception of independent pitch, altitude and actuator-related state measurements. The variable target altitude, induced by the pitch sensor and the WFI pitch estimate which provides an update of upcoming terrain, increases the reference offset temporarily which helps the vehicle climb obstacles over ground (Figs. 4.14B, C, D). The time history comparison of the true and the measured states are shown in Figs. 4.15, 4.16 for part of the broken line trajectory from Fig. 4.14A (corresponding to second major turn). Despite a large lateral offset, it is apparent that WFI state estimates closely track the true states as well as the target state during the course of the sharp maneuver. Near accurate pitch attitude and altitude estimates result from the use of pitch sensor and sonar respectively. Course correction during the sharp maneuver results in the optic flow field showing a strong lateral bias at the instant of lowest proximity, as seen in Fig. 4.15A.

Fig. 4.17 shows that in the presence of sustained gust, from all initial conditions, the helicopter is again able to successfully avoid obstacles while maintaining the desired height above ground. The gust exerts a significant influence on the vehi-

cle dynamics, as seen from two sample trajectories (broken line trajectories in Figs. 4.14A, 4.17A). The gust disturbance causes the vehicle to traverse entirely different trajectories, despite having the same origin. The vehicle surmounts obstacles over ground (Figs. 4.14B, C, D) despite strong gusts in the transverse direction. The time history comparison of the true and measured states are shown in Figs. 4.18 and 4.19 as the vehicle executes a right turn. It is again apparent that the state estimates closely track the true states as well as the target state of the vehicle despite the sharp maneuver. Course correction again results in the optic flow field showing a strong lateral bias at the instant of lowest proximity, as seen in Fig. 4.18A. There are several instances when the vehicle gets in close proximity to an obstacle before initiating an evasive maneuver resulting in large deviation from the target state. Such close encounters occur on fewer occasions in the absence of gust. The low noise levels in the relative state estimates $\hat{\mathbf{x}}$ can be ascribed to white-noise mitigation property of WFI, the spatial filtering of optic flow measurements and the associated outlier rejection step, and the noise attenuation property of the loop shaping approach.

The simulations as seen in this study demonstrate safe navigation behavior of the MAV in an uncertain, cluttered environment. The H_∞ controller synthesis framework for robust stability (Fig. 4.12B) is numerically validated by the obstacle avoidance and terrain following behavior of the vehicle flying in the absence of gust (Fig. 4.14), with the vehicle attempting to track a symmetric path between obstacles in the environment. Furthermore, the strong gust perturbations manifest as large deviation of the vehicle velocity from the nominal values (Fig. 4.19), and re-

sults in the vehicle traversing different routes from the same origin, as seen with the broken line trajectories in Figs.4.14A, 4.17A. The loop shaping framework generates a feedback gain that results in significant gust mitigation, as seen from the singular value plot of $G_{\mathrm{d_{cl}}}$ (Fig. 4.20), especially at low frequency. The vehicle manages to fly safely even in the presence of strong gust, validating the performance of the vehicle and demonstrating robustness to the combined influence of environmental uncertainties and gusts. Thus, accurate state estimation and good command tracking characteristics in the presence of such strong gust disturbance and environment structural uncertainty establishes the reliability of the WFI framework and loop shaping approach for navigation.

As noted above, there are several close encounters of the vehicle as it traverses the environment buffeted by gusts. This is particularly the case when the vehicle encounters symmetric obstacles in its flight path, where small lateral optic flow asymmetries grow larger when the vehicle nears collison, initiating an evasive maneuver before impact. The current environment model is restricted to detecting lateral proximity and excludes walls in the longitudinal direction, rendering the vehicle blind to such obstacles. Symmetric obstacles induce minimal optic flow across the visual field, suggesting the need for a forward pointing laser rangefinder or extend the current environment model to link longitudinal proximity to a continuous control capability for collision avoidance in such instances.

With regard to literature comparison, as optic flow is a scaled relative measure of speed/depth and does not provide explicit measure of the environment structure, most studies of MAV navigation with optic flow assume either prior knowledge of

vehicle motion [44] or prior knowledge of the environment [74, 51]. Furthermore, the ablity of the vehicle in the present study to navigate a cluttered environment successfully is superior to the methodology followed in [75, 62] which is restricted to regulating flight behavior in the absence of gusts. In addition, the current study uses the complete spherical viewing arena to generate navigation cues, making it superior to [76] where measurements were confined to the three orthogonal rings rendering the vehicle vulnerable to obstacles not appearing in either the pitch, yaw or the roll plane. The obstacle avoidance behavior in Figs. 4.14, 4.17 is achieved by jointly regulating vehicle pose and proximity, and hence outperforms earlier studies that only regulate proximity in the horizontal [39] and vertical [45, 46] plane. A disadvantage of using imaging devices is their unsuitability to low contrast environments, necessitating the use of feature tracking and detection based navigation algorithms [77]. However, the associated computational burden is too large for practical implementation onboard an MAV.

With regard to concept feasibility, note that an attractive property of WFI is the high computational simplicity in motion-state extraction. Typical SLAM algorithms that employ feature detection and tracking techniques for motion state extraction in unknown environments are typically more computationally expensive, thus requiring off-board implementation [56]. For instance, a typical iteration is implemented on an Intel Core 2×2 GHz processor that processes high resolution images (640×480) captured at 30 fps [78]. In contrast, WFI-based navigation strategies, being more computationally efficient, have been implemented onboard on a 500 MHz fixed point processor that processes low resolution images (160×120) captured at

55fps [26].

The methodology proposed in this chapter is certainly feasible as lightweight accelerometers, and sonar sensors or laser rangefinders have been used extensively on existing MAVs for accurate pitch and altitude estimation [79, 26]. Also, it is certainly practical to use optic flow to estimate the other nine states, particularly using just the lower hemisphere measurements which have been found to be sufficient in generating accurate relative state estimates [62]. The size of the dynamic controller equals the size of the vehicle model and the size of the precompensator. It may be beneficial to investigate model reduction techniques to reduce the size of the H_∞ controller, which is beyond the scope of study. Also, the dynamic compensation framework of the loop shaping approach requires a digital implementation supporting a floating point processor, which results in a greater payload as opposed to a static compensation framework. A reduced order H_∞ controller resulting in better vehicle performace coupled to a lower hemisphere optic flow sensor with reduced payload requirements is certainly a practical option for three-dimensional MAV navigation applications.

This section demonstrates that optic flow-guided navigation methodology based on the coupling of spatial decompositions of optic flow patterns with H_∞ loop shaping approach can be used to design a dynamic controller that ensures safe navigation behavior in a complex, three-dimensional urban environment subjected to gusts. Given the current lack of sensors with the required size and bandwidth capabilities, as well as computationally efficient estimation and control algorithms, coupling the optic flow sensor with the H_∞ dynamic controller provides an attractive alternate

paradigm for MAV navigation applications.

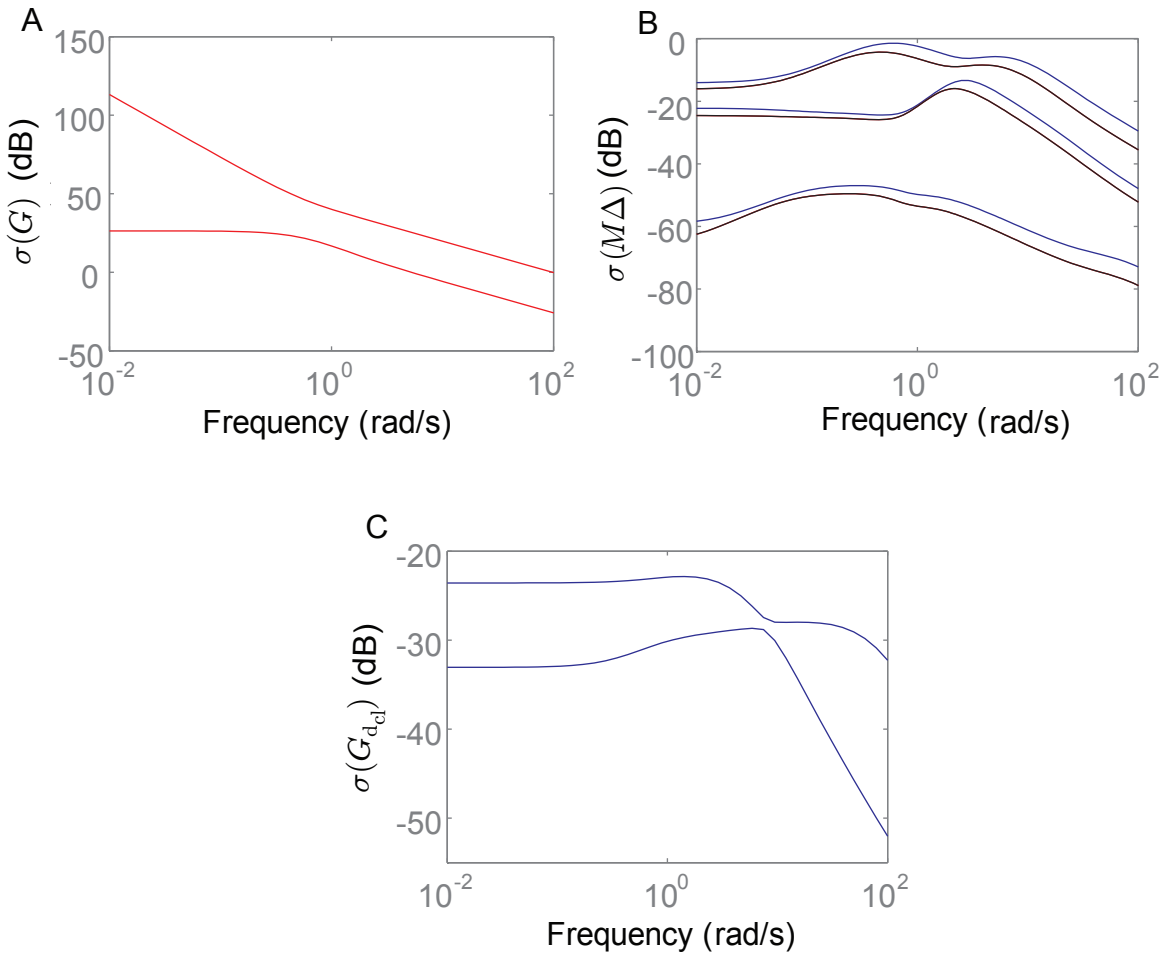

Figure 4.8: Singular value plots. (A) Open loop plant; (B) Loop gain for limiting cases of environment uncertainty discussed in section 2.2; (C) Closed loop gust transfer function.

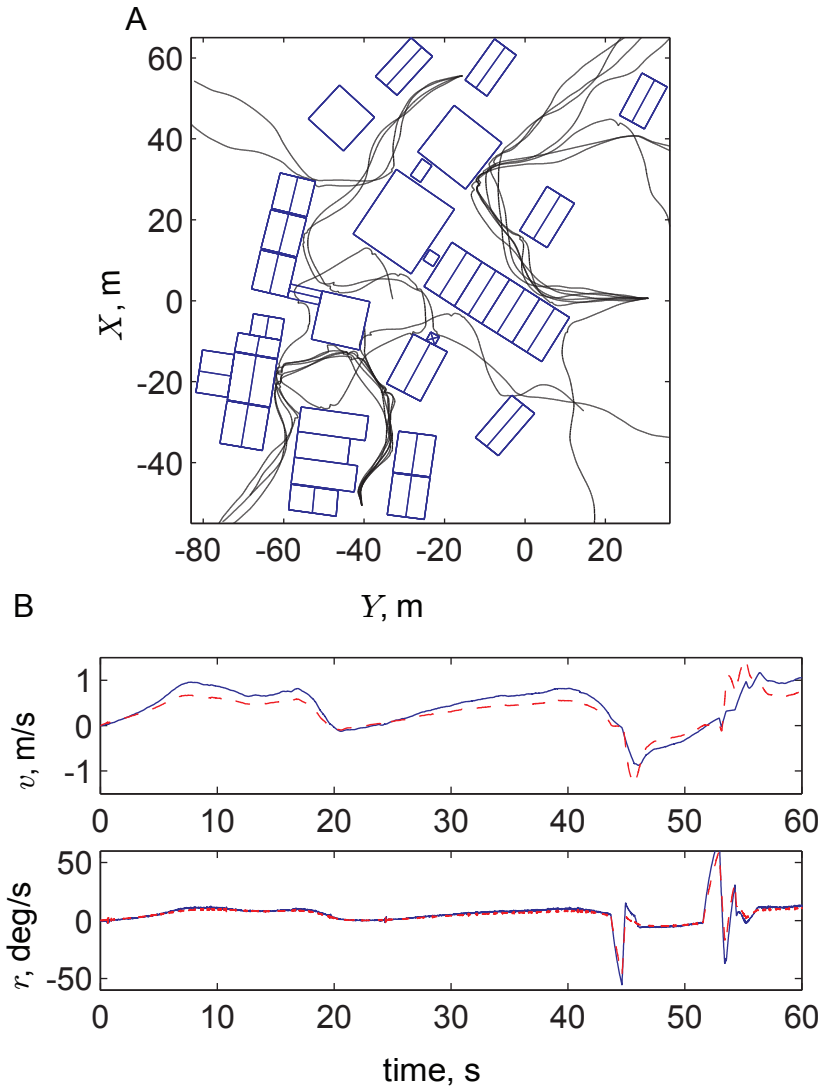

Figure 4.9: (A) Simulation results depicting top view of vehicle trajectories in the urban-like environment subjected to gusts; (B) Time history comparison of vehicle lateral velocity and yaw rate; Blue solid lines represent true states, red broken lines represent state estimates.

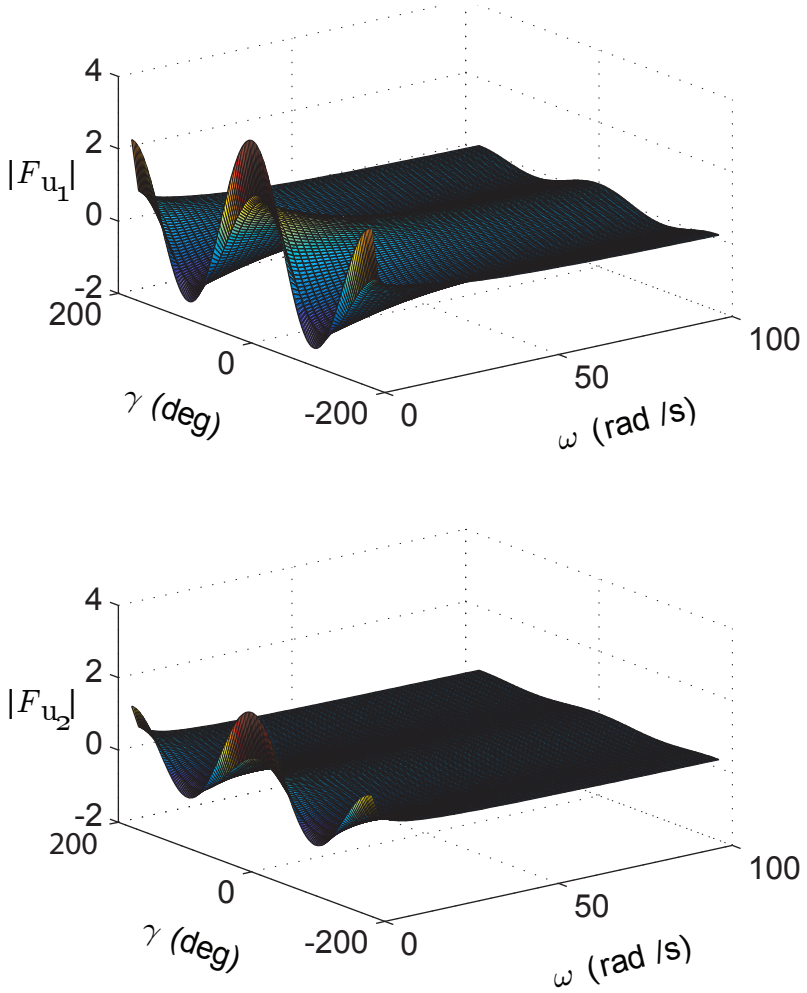

Figure 4.10: Frequency dependency of input extraction function $\mathbf{F_u}$.

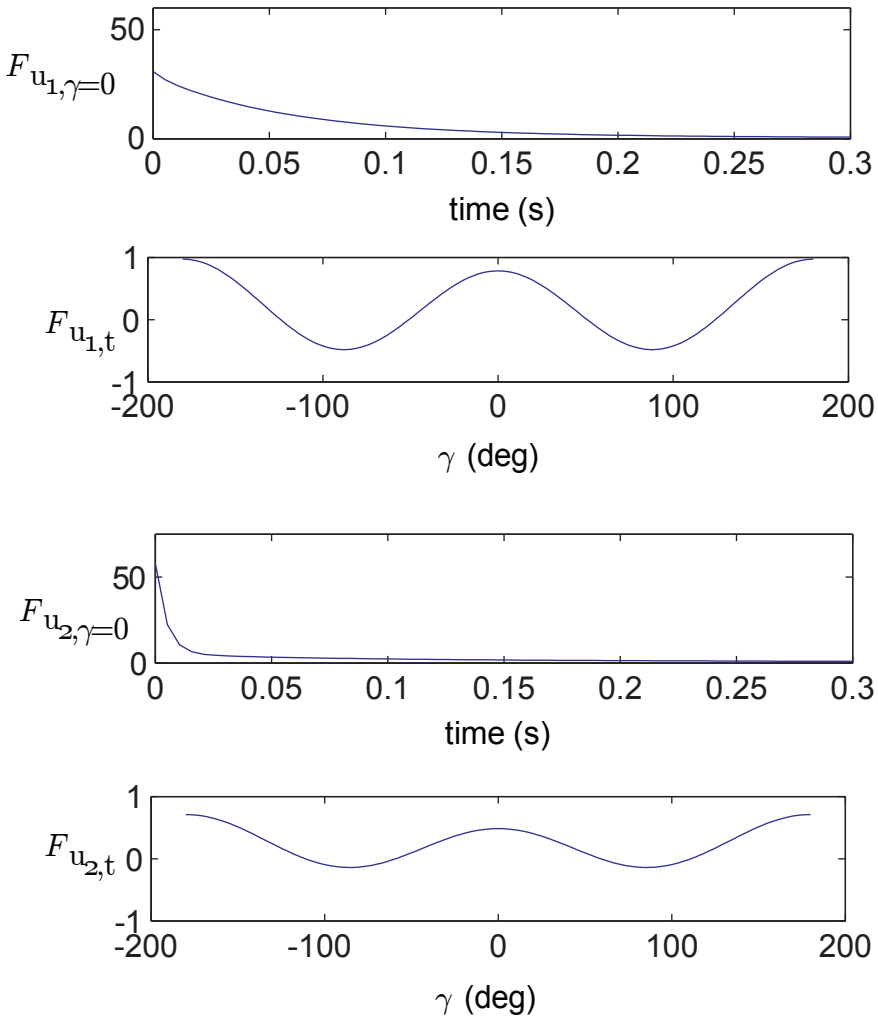

Figure 4.11: Time domain plots of $\mathbf{F_u}$.

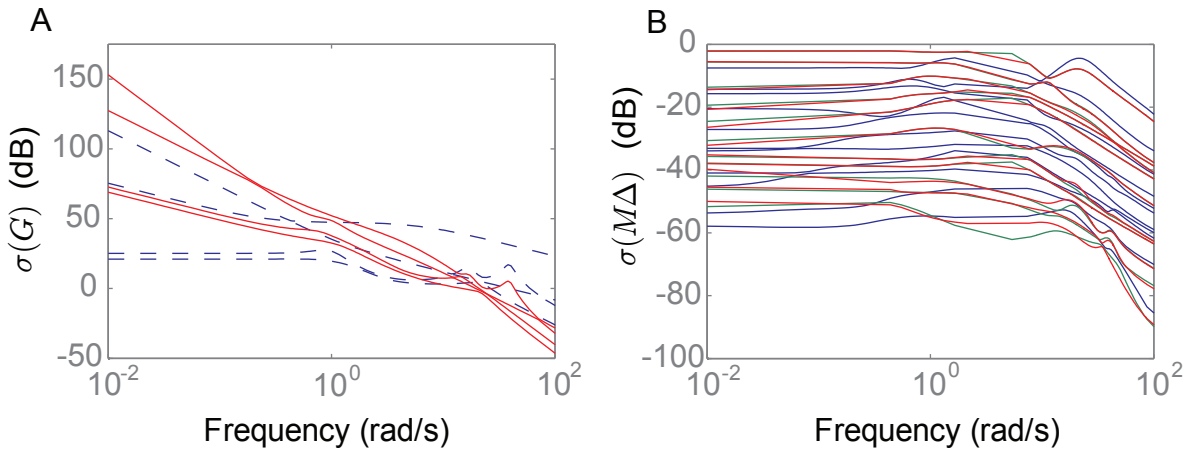

Figure 4.12: (A) Open loop and shaped plant singular value plot; Broken lines represent singular values of open loop plant G, solid lines represent singular values of shaped plant G_s (B) Singular values of loop gain of the closed loop plant incorporating uncertainty corresponding to the three limiting cases discussed in section 2.2.

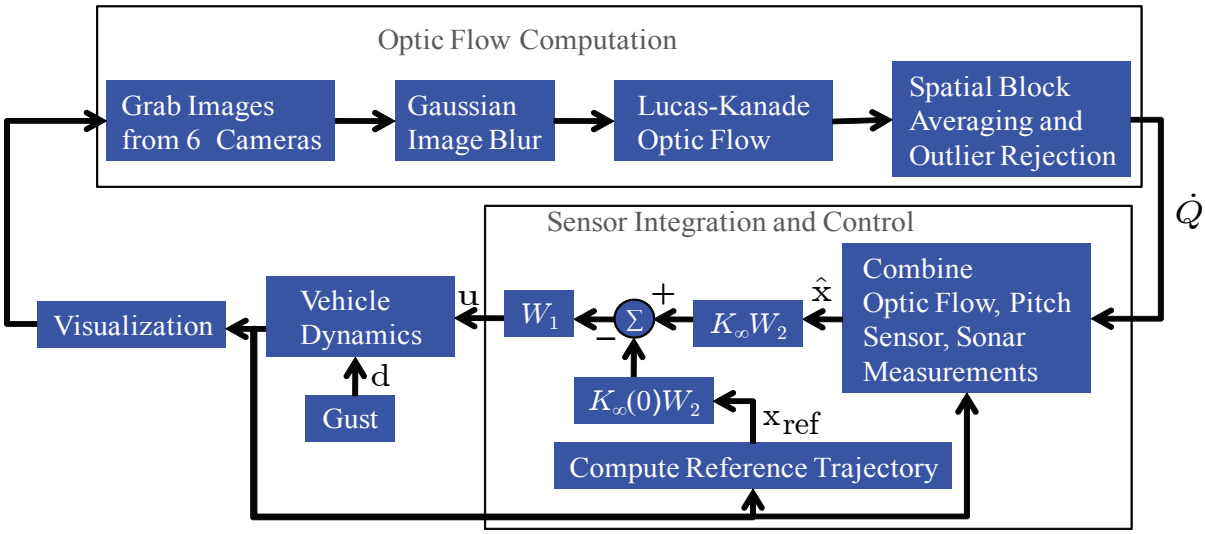

Figure 4.13: Operational flow chart for 3D navigation.

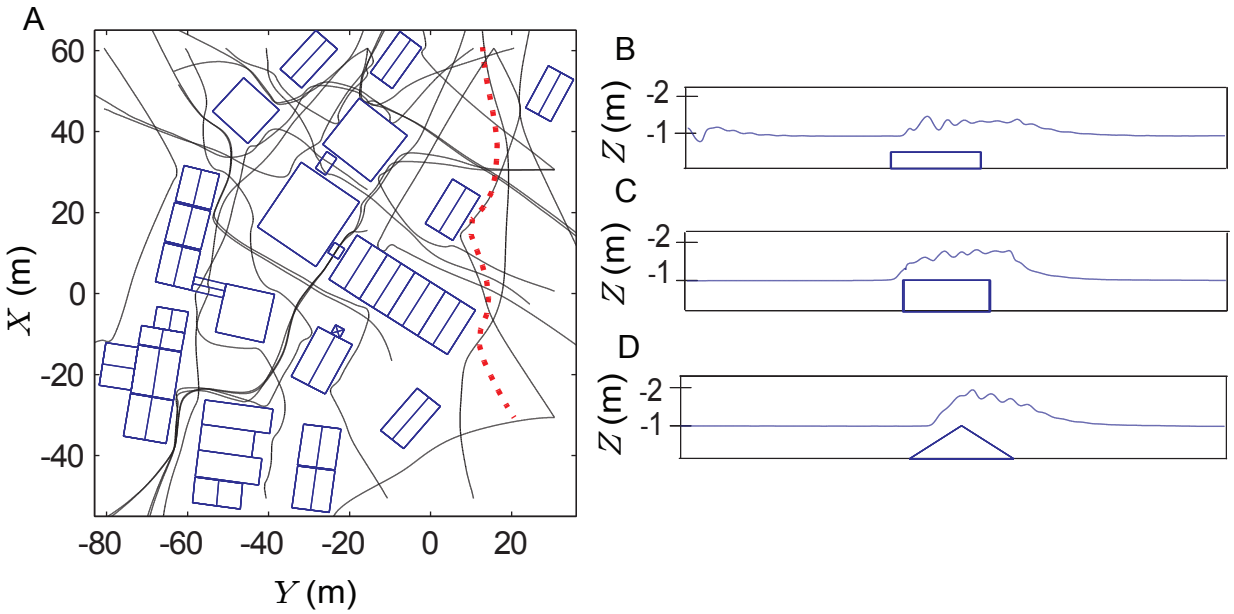

Figure 4.14: (A) Simulation results with trajectories in the absence of gust; (B) trajectory side-view during flight over a 0.5 m box; (C) 1 m box; (D) 1 m ramp.

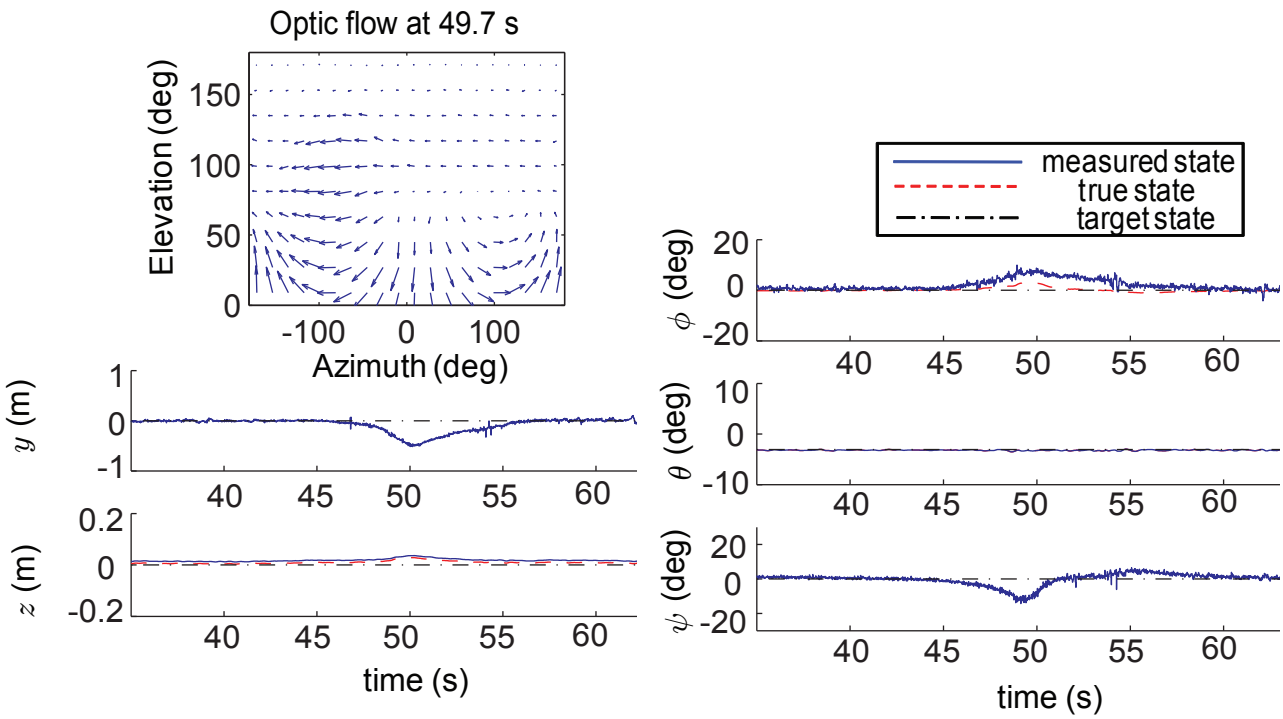

Figure 4.15: Time history comparison of vehicle proximity and pose of dashed-line trajectory from Fig. 4.14.

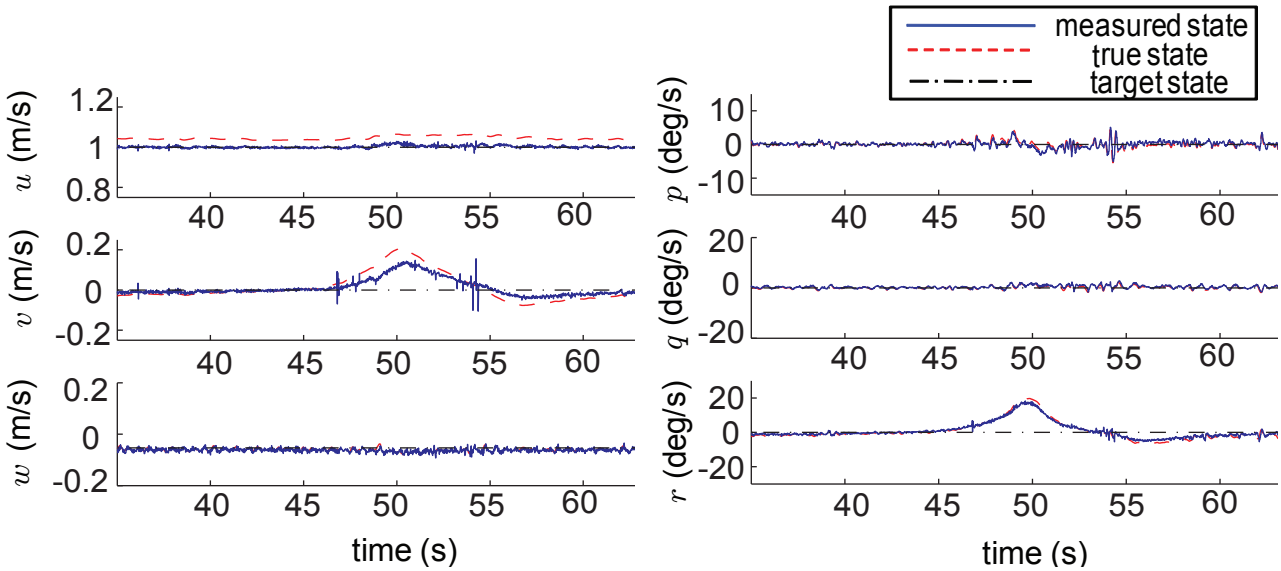

Figure 4.16: Time history comparison of vehicle velocity and rotational rate of dashed-line trajectory from Fig. 4.14.

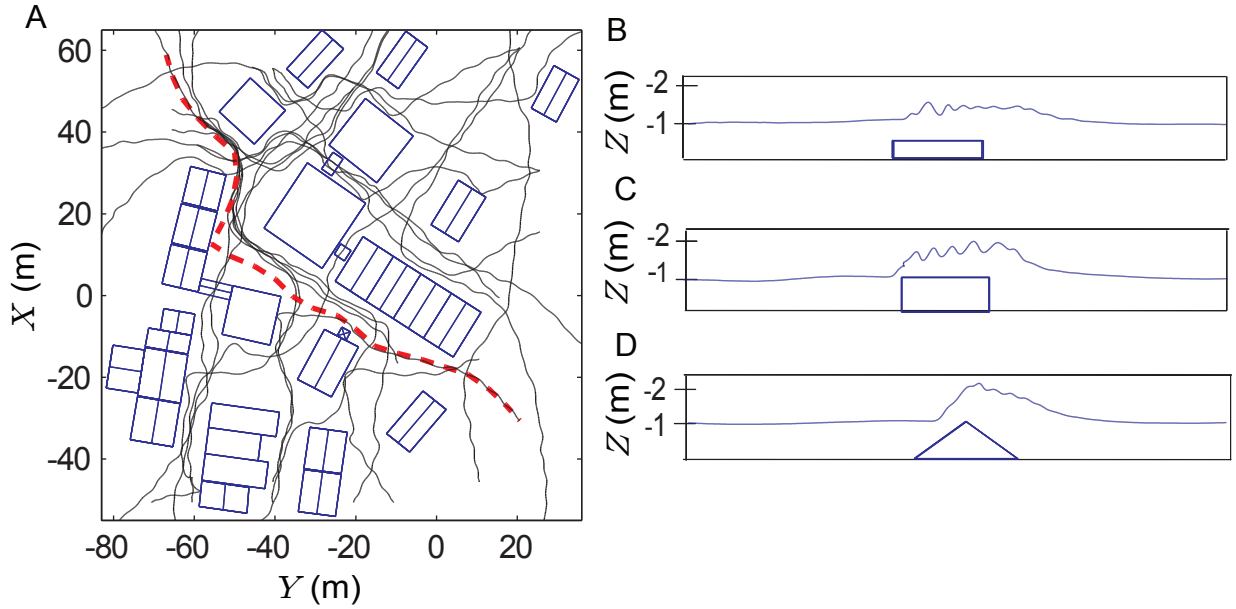

Figure 4.17: (A) Simulation results with trajectories in the presence of gust; (B) trajectory side-view during flight over a 0.5 m box; (C) 1 m box; (D) 1 m ramp.

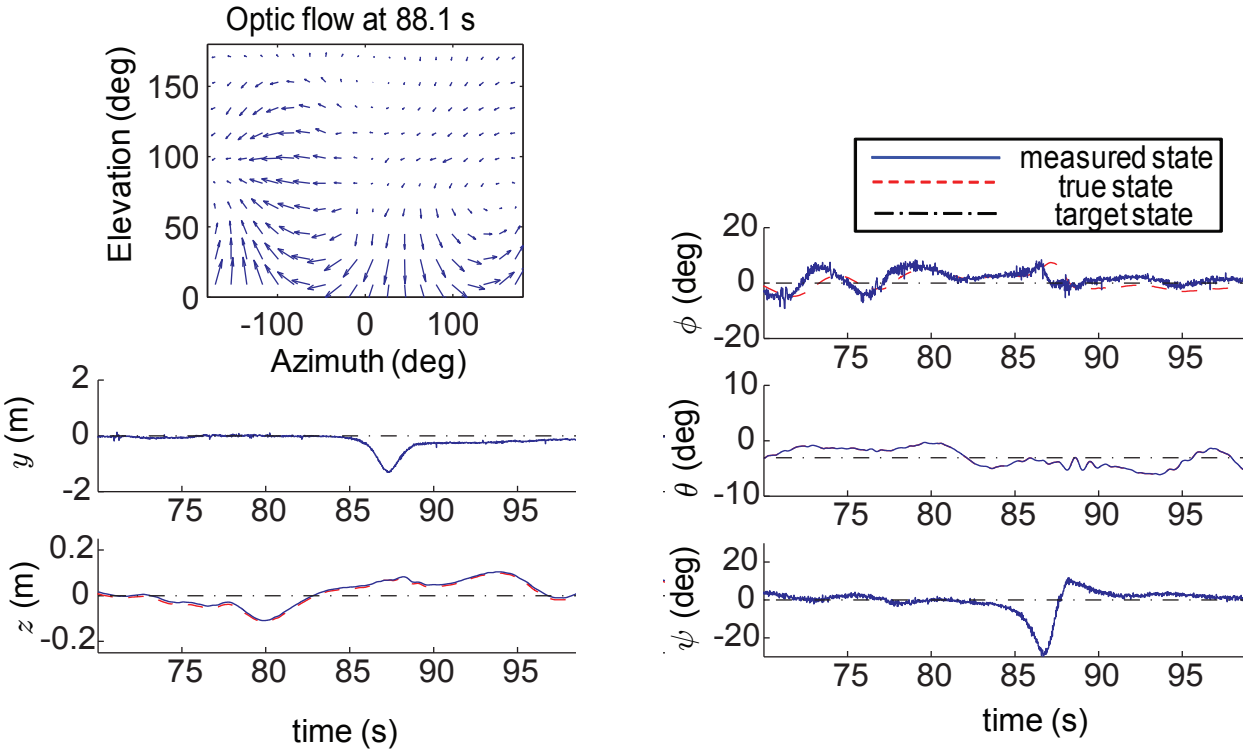

Figure 4.18: Time history comparison of vehicle proximity and pose of dashed-line trajectory from Fig. 4.17.

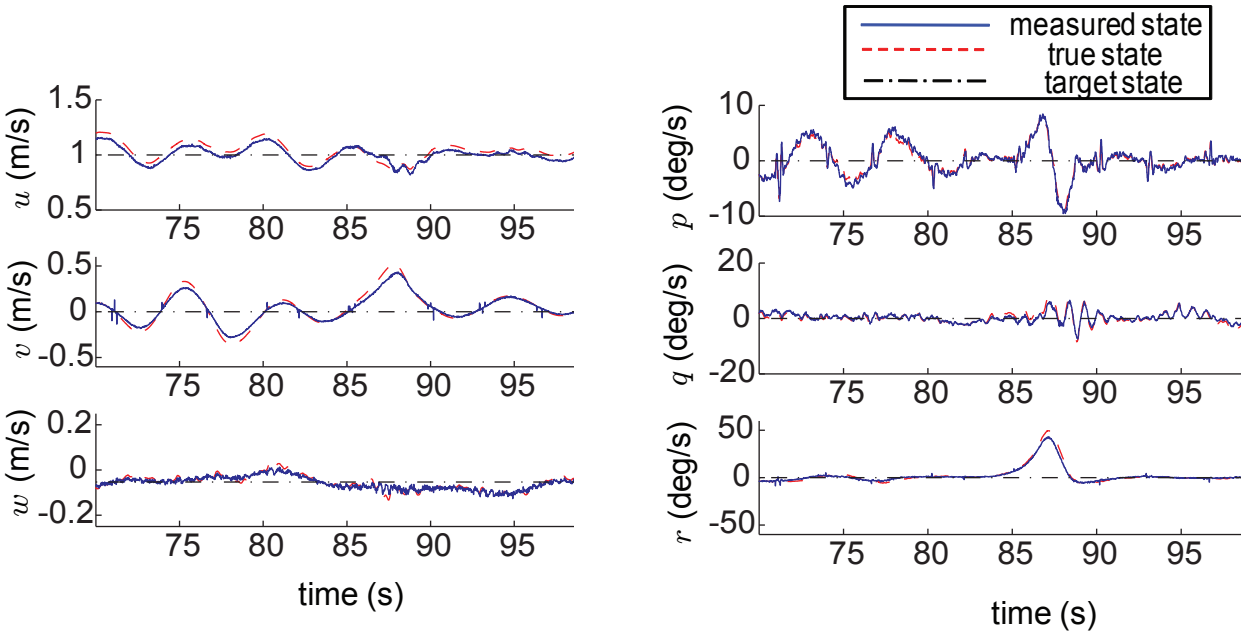

Figure 4.19: Time history comparison of vehicle velocity and rotational rate of dashed-line trajectory from Fig. 4.17.

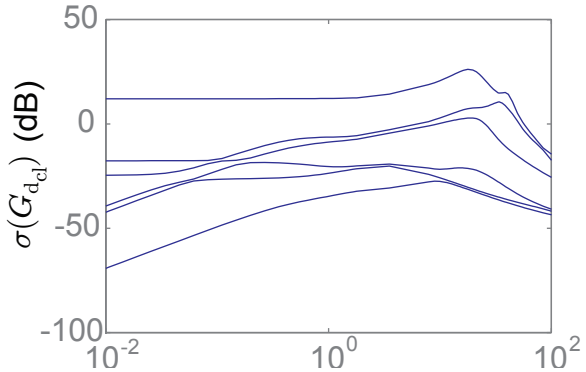

Figure 4.20: Singular value plot of closed loop gust transfer function.

Chapter 5

Hair Mechanosensory System

As noted previously, obtaining reliable translational and rotational velocity measurements for navigation of micro air vehicles is a challenge given the current state of sensing technology, with the need for novel sensors and sensory processing techniques if autonomous microsystems are to be successful. Also, the limitations of the optic flow system, especially for planar navigation, renders accurate velocity estimation necessary for good vehicle performance. In the previous few chapters, a H_∞ loop shaping based dynamic controller synthesis framework was presented for achieving the twin objectives of improved vehicle performance for planar navigation applications and safe reflexive 3D navigation in an obstacle laden environment that is subjected to gusts. This chapter presents an alternate approach of using hair mechanosensory arrays in conjunction with optic flow towards achieve the same objectives. Both planar and 3D navigation are considered. Static - as opposed to dynamic - compensation is employed, yielding a fast and efficient computation paradigm.

An isolated hair mechnosensory sensillum is a tactile sensor that responds to dynamic pressure and deflects in response to airflow. Consequently, the integrated hair array output can be used to detect relative wind velocity. In conjunction with the optic flow output, the hair array output can then be used to either augment

stability, resulting in better vehicle performance in planar navigation applications, or detect wind velocity, which can be used to negate gusts in a feedforward manner. Thus, for gust rejection applications, the tasks for the optic flow and the hair sensor systems can be neatly decoupled. Optic flow outputs are used to generate accurate estimates of vehicle proximity and velocity for navigation in an uncertain environment, while hair array outputs are used to generate wind velocity estimates for gust rejection. A miniature hair sensor array satisfying the size, weight and power constraints of a micro flying platform and which provides relative wind velocity estimates would be invaluable when embedded in such a platform and used in conjunction with processed outputs from the visuomotor system for flight stability, control and navigation.

5.1 Review of Insect Hair Sensor Array-Based Navigation

The insect flight control system is an excellent example of how stimuli from multiple sensory modalities are parsed and integrated into a common neural code that shapes the organism's behavioral response. During flight, insects experience a number of external and internal influences, such as wind gusts or wing damage, that act to create unintended deviations in the desired flight path. Typically, two or more exteroceptive sensors–compound eyes and mechanoreceptive wind hairs on the thorax and the head, for instance–act in concert for wind sensing and direction. Importantly, the systems might detect different aspects of the relative wind: optic flow might provide the body velocity estimates and the trichoid hair sensillae might

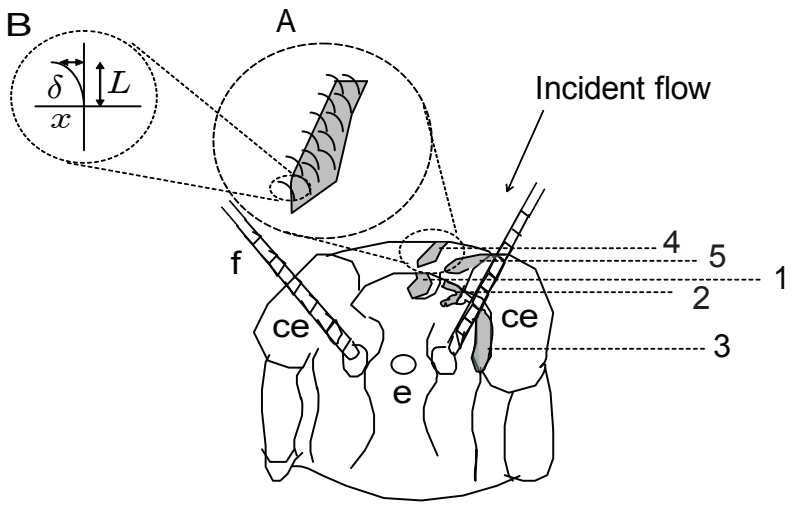

Figure 5.1: Frontal view of locust head with the five sets of hair arrays shaded in grey (redrawn from [81]). Inset A: Close up view of an array with distributed sensillae. Inset B: Sensor response (δ) caused by flexure from incident flow. ce-compound eye, e-ocelli, f-antenna.

provide an estimate of relative wind velocity and direction [80]. Hence, optic flow is one possible source of information that can be used to derive estimates of relative velocity for feedback, while the arrays of mechanoreceptive wind hairs provide an additional source of velocity information. In general, the presence of multiple kinds of sensors capable of detecting similar motion cues points towards the usefulness of back-up systems increasing stability as well as robustness in flight.

Arrays of trichoid hairs are found all over insect bodies including abdomen, thorax, wings and head (Fig. 5.1). These arrays deflect in response to air flow, with the sensor cells exhibiting a shift in the membrane potential, firing neurons at a frequency that is in general proportional to relative wind velocity and direction

[82]. The sensor inputs thus generated provide useful cues for navigation and flight stability, much like those obtained from optic flow. For instance, arrays of hair found on the locust head have been known to provide information of its yaw rate [83]. The insect trichoid hair sensillae are directionally sensitive and respond to flows along certain directions. This directional sensitivity arises primarily due to the eccentric attachment of the dendrite to the base of the hair shaft [84, 85], the shaft curvature and the socket force asymmetry at the base of the hair shaft [82], with the response being greatest in the direction opposite to the direction of shaft curvature.

The role of wind hair sensillae in navigation and stabilization of insect flight has been well known for a few decades [86, 87, 81]. In his seminal work, Weis Fogh directed a steady stream of air at the head of a desert locust at various angles of sideslip and showed that wind stimulation of hair arrays was a sufficient condition for initiating and maintaining flight in locusts. In an investigation of the role of the air current sensors in horizontal course control of tethered *Locusta migratoria* [88], it was found that the wind sensitive hair fields were the predominant sensor arrays involved in flight control. Moreover, the wind sensitive hair fields were found to directly control wing beat parameters that affected the course stabilizing horizontal flight maneuvers.

The local hair response is ambiguous as it is largely dependent on local flow velocity as well as its orientation and local temperature. Hence, the hair sensor system is thought to generate motion cues useful for navigation and stability through the combined array response obtained by integrating the individual hair responses over the array. Support for this surmise arises from the fact that the hair sensors

in over any array on the locust head are oriented in the same direction [89]. Also, the wind hair outputs have been found to be spatially compatible with the visual output and a map of the transduction channel for the wind-senstive hair system has been found to be very similar to that of the visuomotor system [90]. The numerous cephalic wind hair inputs,carried by sensory neurons, converge on parallel channels of descending interneurons that pass through the circumoesophageal ganglion on the ipsilateral side onto the suboesophageal ganglion, the cervical connective and finally through the thoracic ganglia where they emerge to provide just a few inputs to the flight motor neurons, which are post synaptic to thoracic interneurons [84, 91, 92]. Hence, each hair sensor is associated with one nerve cell, each of which carry the large number of hair array outputs and converge on relatively few descending interneurons, which in turn communicate with the flight motor. Thus, it is apparent that the transduction mechanism of the visuomotor and the hair mechanosensory systems are similar. Consequently, the mathematical formalism of *wide-field integration* can be used to study integrated hair array outputs.

The framework and approach outlined in this paper, initially demonstrated by Humbert *et al.* [58] for optic flow, takes advantage of the fact that while individual hair sensor response might be ambiguous in nature, valuable information related to the vehicle body states - encoded by the spatial structure of sensor response pattern spread over a wide field - can be extracted by weighting these patterns with a set of orthogonal functions which are then reducible to just a handful of control inputs and can be used to provide either increased stability or gust mitigation. The objective in this chapter is to develop a mathematical framework for combining hair

sensor array outputs with the optic flow outputs for the purpose of vehicle stability augmentation and gust rejection. Two different applications are looked at–stability augmentation of the micro-helicopter undergoing planar motion along a quiescent corridor and gust rejection of a fixed wing micro-air-vehicle undergoing 3D motion in an urban environment.

5.2 Individual Hair Sensor Response

In this section, the invididual hair sensor response is considered. Each hair sensor is modeled as a cantilever beam, a large fraction of which is assumed to be immersed in the boundary layer and with the tip immersed in a region of potential flow. The sensor responds to the dynamic pressure with flow viscosity having a significant influence on the sensor response. Accordingly, the Reynolds number largely determines the magnitude of the tip deflection and the root strain. Larger the Reynolds number, smaller the thickness of the boundary layer as the flow negotiates the surface, and larger is the tip deflection. The external excitation frequency is assumed to be small compared to the sensor's fundamental frequency, resulting in the inertial effects exerting a negligible influence on the sensor output. As the hair sensor responds to dynamic pressure across the surface, the sensor output can be written as (to the first order),

$$\delta = K_p \, ||V|| V \tag{5.1}$$

where V is the local flow velocity. The constant K_p depends on the properties of the hair sensor (length L, bending stiffness EI) and the flow (density ρ, drag coefficient

C_D), and therefore accounts for the effects of flexure of the hair sensor as well as boundary layer effects of the flow. Hence, the sensor output is proportional to the square of the local flow velocity. Both linear and curved MEMS-based artificial hair sensor arrays have been fabricated and the quadratic nature of the sensor output has been demonstrated in prior studies [93, 94].

5.3 Stability Augmentation in a Corridor

The limitations of using optic flow outputs for planar navigation, where the outputs couple inplane vehicle states v and ψ, was previously pointed out in chapter 2. In this section, it is shown that the hair array outputs can be used to augment the stability of the micro-helicopter by combining with optic flow outputs, as it traverses down the corridor. Towards that end, the integrated array response over a circular array (encoding vehicle-level properties) is considered. Assume that the micro-helicopter carries a circular ring, on which, mounted symmetrically on either side of the longitudinal axis, hair sensor arrays are located extending between $\phi_1 \leq \gamma \leq \phi_2$, and $2\pi - \phi_2 \leq \gamma \leq 2\pi - \phi_1$, with γ being the azimuth angle (anticlockwise positive, Fig. 5.2). If the vehicle perturbation states are small ($\frac{v}{u_0}$, $\frac{y}{a}$ $<<$ 1, small ψ, r), the flow over the hair arrays can be assumed to be fully attached. It is further assumed that the hair ring remains unaffected by the downwash from the main rotor. Finally, the hair sensor arrays are assumed to be directionally sensitive, with the sensors responding to air flow in the tangential direction (to the circular ring).

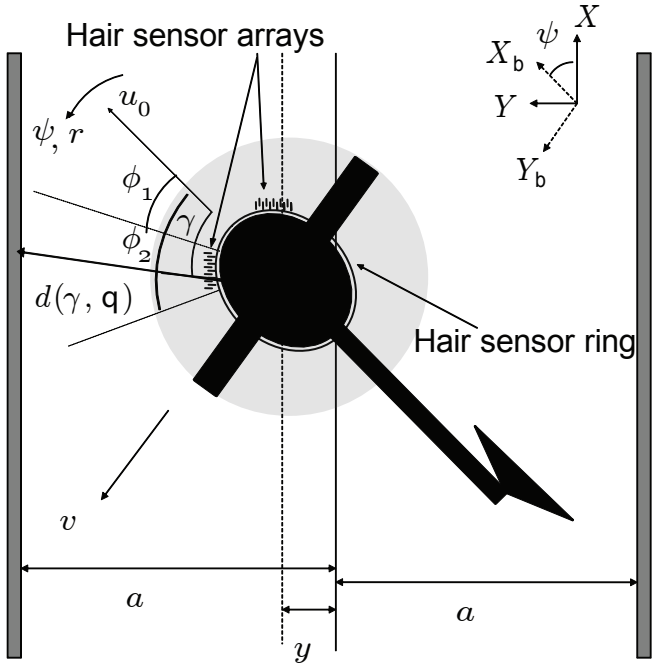

Figure 5.2: Hair sensor arrays on the micro-helicopter.

For planar incident flow, we have,

$$\delta(\gamma) = K_p \, ||V(\gamma)||V(\gamma), \tag{5.2}$$

where, $V(\gamma)$ is the azimuthal variation of the local tangential flow velocity.

If β_{ss} is the sideslip angle, defined as the angle between the body's longitudinal axis and the relative wind, it can be easily observed that for small perturbations, $\beta_{\text{ss}} = \frac{v}{u_0}$. From the results of planar, uniform potential flow around a sphere with a rotational velocity r, we have for flow around the hair sensor ring,

$$V(\gamma) = \frac{3}{2} u_0 \sin\gamma - \frac{3}{2} v \cos\gamma - R\, r, \qquad 0 \leq \gamma \leq 2\pi.$$

Rearranging, we have in the relative wind frame,

$$V(\gamma) = \frac{3}{2} U \sin(\gamma - \beta_{\text{ss}}) - R\, r, \qquad 0 \leq \gamma \leq 2\pi. \tag{5.3}$$

where $U = \sqrt{u_0^2 + v^2} \approx u_0$ is the resultant body translational velocity.

If the hair array response is assumed positive for clockwise deflection,

$$\delta = \begin{cases} -K_p V^2(\gamma), & \phi_1 \leq \gamma \leq \phi_2; \\ K_p V^2(\gamma), & 2\pi - \phi_2 \leq \gamma \leq 2\pi - \phi_1. \end{cases}$$

The wide-field integration technique for hair sensor arrays over the hair array S^1 can then be modeled as an inner product of sensitivity functions with the sensor response.

$$y_i^h(\mathbf{x}) = \langle\, \delta(\gamma, \mathbf{x}), F_i^h(\gamma) \rangle = \int_0^{2\pi} \delta(\gamma, \mathbf{x}) \,.\, F_i^h(\gamma)\, d\gamma. \tag{5.4}$$

Since the hair sensor arrays extend only over $\phi_1 \leq \gamma \leq \phi_2$ and $2\pi - \phi_2 \leq \gamma \leq 2\pi - \phi_1$, we have,

$$\begin{aligned} y_i^h(\mathbf{x}) &= \langle\, \delta(\gamma, \mathbf{x}), F_i^h(\gamma) \rangle \\ &= \int_{\phi_1}^{\phi_2} \delta(\gamma, \mathbf{x}) \,.\, F_i^h(\gamma)\, d\gamma \\ &+ \int_{2\pi-\phi_2}^{2\phi-\phi_1} \delta(\gamma, \mathbf{x}) \,.\, F_i^h(\gamma)\, d\gamma. \end{aligned} \tag{5.5}$$

For the hair sensor array under consideration, the components of the Fourier series $(1, \sin\gamma, \cos\gamma, \sin 2\gamma, \cos 2\gamma ...)$, which form a linearly independent set over $\gamma \in [\phi_1, \phi_2] \cup [2\pi - \phi_2, 2\pi - \phi_1]$, are used to construct a set of orthonormal basis fuctions using the Gram-Schmidt Orthonormalization process, resulting in $(1/2(\phi_2 - \phi_1))^{1/2}$, $\frac{1}{d}(\cos\gamma - \frac{\sin\phi_2 - \sin\phi_1}{(\phi_2 - \phi_1)})$, $\frac{1}{e}\sin\gamma$ - corresponding to the first three Fourier harmonics - as the basis functions for wide-field spatial integration. Taking the inner

Table 5.1: Hair array array response $y^h(\mathbf{x})$

WFI sensory input	Linearization
$a_0^h = -\frac{9}{4}u_0 l/\sqrt{2f}v - 6Ru_0\frac{c}{\sqrt{2f}}r$	$-\frac{9}{4}u_0 l/\sqrt{2f}v - 6Ru_0\frac{c}{\sqrt{2f}}r$
$a_1^h = \frac{9}{4}u_0(\frac{lg_1}{fd} - \frac{(b+c)}{d})v + \frac{3}{2}Ru_0(\frac{4cg_1}{fd} - \frac{l}{d})r$	$\frac{9}{4}u_0(\frac{lg_1}{fd} - \frac{(b+c)}{d})v + \frac{3}{2}Ru_0(\frac{4cg_1}{fd} - \frac{l}{d})r$
$b_1^h = \frac{1}{e}(\frac{9}{8}\,u_0^2(3c-b) + \frac{9}{8}\,u_0^2\,\beta_{\mathrm{ss}}^2(b+c) + \frac{3}{2}R\,u_0\,l\,\beta_{\mathrm{ss}}\,r)$	$\frac{9}{8e}\,u_0^2(3c-b)$

product with the tip displacement pattern, from (5.5),

$$\begin{aligned} y_{a_0}^h &= \frac{1}{K_p}\langle\,\delta, 1/\sqrt{2f}\rangle, \\ y_{a_1}^h &= \frac{1}{K_p}\langle\,\delta, \frac{1}{d}(\cos\gamma - \frac{g_1}{f})\rangle, \\ y_{b_1}^h &= \frac{1}{K_p}\langle\,\delta, \frac{1}{e}\sin\gamma\rangle. \end{aligned} \tag{5.6}$$

where,

$$\begin{aligned} b &= \frac{1}{3}(\cos 3\phi_2 - \cos 3\phi_1),\ c = \cos\phi_2 - \cos\phi_1, \\ d &= \sqrt{f + h_1 - 2\frac{g_1^2}{f}},\ e = \sqrt{f - h_1}, \\ f &= \phi_2 - \phi_1,\ g_1 = \sin\phi_2 - \sin\phi_1, \\ h_1 &= \frac{1}{2}(\sin 2\phi_2 - \sin 2\phi_1),\ l = \cos 2\phi_2 - \cos 2\phi_1,\ . \end{aligned}$$

Table 5.1 lists the planar hair array response and their linearizations obtained

from (5.6). It is apparent that the coefficients $y^h_{a_0}$ and $y^h_{a_1}$ are linear in β_{ss} and r. Hence, for a helicopter flying at a constant forward speed u_0, the processed hair sensor outputs that are sent to the flight motor generate direct linear estimates of the lateral translational velocity and the yaw rate, much like the processed outputs from optic flow. It is also apparent that an estimate of forward speed can be exclusively obtained from $y^h_{b_1}$ component of the hair array output. In addition, in hover $u_0 = 0$, and hence $\mathbf{y}^h = 0$. Therefore, hair sensor reponse cannot be used to stabilize the vehicle dynamics in hover. The response gets progressively stronger as the vehicle reference speed increases. Also, these outputs are exclusively a function of the velocity states of the vehicle. This is a typical feature of the hair sensor array. They do not generate information regarding the position states of the system, and hence cannot be independently used in applications where such information is critical, such as centering and obstacle avoidance. These sensors are thus usually used in concert with the visuomotor system, as is generally the case with flying insects. Finally, it is important to note that the hair sensor arrays generate a measure of the sideslip angle β_{ss} that can be used in feedback for horizontal course correction.

The block diagram for combining the hair array outputs with the visuomotor system is shown in Fig. 5.3. Neglecting the $y^h_{b_1}$ component, the combined observation equation is:

$$\mathbf{y} = \mathrm{C}\,\mathbf{x}, \tag{5.7}$$

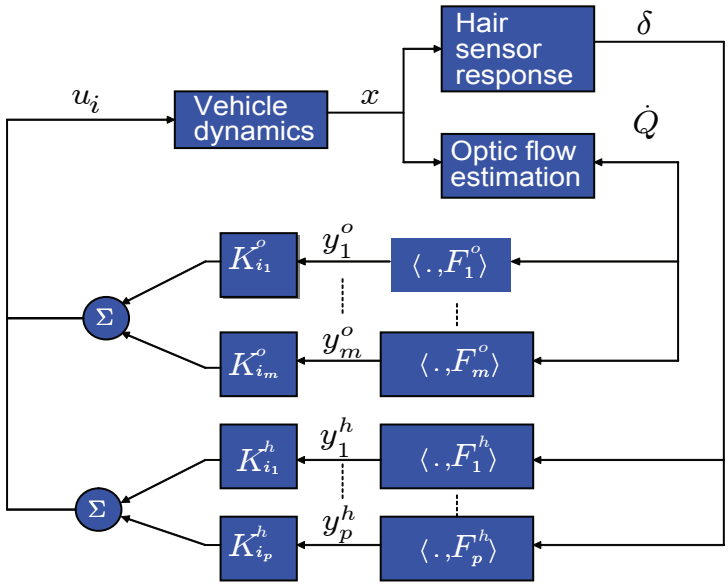

Figure 5.3: Static output feedback architecture for stability augmentation using hair sensor arrays.

where,

$$\mathrm{C} = \begin{bmatrix} \frac{-u_0}{2a^2} & 0 & 0 & 0 \\ 0 & \frac{-4}{3\pi a} & \frac{4u_0}{3\pi a} & 0 \\ 0 & -\frac{9}{4}u_0\frac{l}{\sqrt{2f}} & 0 & -6Ru_0\frac{c}{\sqrt{2f}} \\ 0 & \frac{9}{4}u_0(\frac{lg_1}{fd} - \frac{(b+c)}{d}) & 0 & \frac{3}{2}Ru_0(\frac{4cg_1}{fd} - \frac{l}{d}) \end{bmatrix}.$$

It was earlier noted that the optic flow outputs couple some of the inplane states and hence couple the lateral and yaw dynamics imposing severe limitations on the closed loop dynamics, bandwidth and performance (table 2.1). Combining optic flow and hair array outputs together allows for the decoupling of the states v and ψ from one another. This fact, together with the fact that lateral position estimates can be computed directly from optic flow results in a complete decoupling

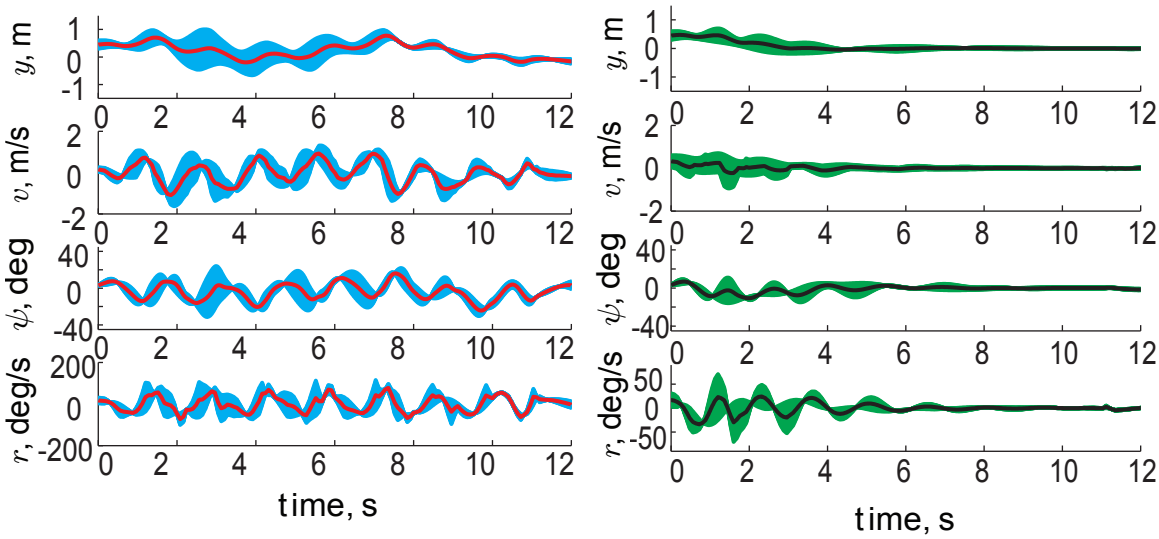

Figure 5.4: Lateral, Yaw dynamics for small perturbations with trajectories (and mean) for 20 trials; (A) Band (solid line) represents combined trajectories (mean) using just optic flow outputs, (B) Band (solid line) represents trajectories (mean) with combined hair and optic flow outputs.

of lateral and yaw dynamics. By including the hair sensor system and decoupling the lateral and yaw dynamics, the constraints on the gain selection can be alleviated allowing for greater latitude in the choice of gains of the system which improves bandwidth and performance, especially in yaw.

Hence, for quiescent flows, one can express δ in closed form, and subsequently linearize about the desired equilibrium pattern of hair deflection, yielding the linear output equation $\mathbf{y} = \mathbf{C}\,\mathbf{x}$. Modern control techniques such as LQR and pole placement can then be applied to derive gains for desired stability and navigational performance.

The hair array and optic flow outputs are combined to help stabilize and

navigate the micro-helicopter down the centerline of the corridor is demonstrated. Towards that end, static output feedback is used to couple the sensor systems with the in-plane dynamics of the helicopter and set up the stability augmentation system. The feasibility of using static output feedback would be evaluated for the combined sensor input through linear control design that guarantees local asymptotic stability of the complete nonlinear system, in effect extending the methodology used previously [26] to stabilize the vehicle using optic flow exclusively.

The equations of motion, linearized about the reference flight condition, describing the lateral (or sideslip) and yaw dynamics in the body frame are given by (4.3). The closed loop dynamics with static output feedback is governed by the equation $\dot{\mathbf{x}} = (\mathrm{A} + \mathrm{B}\,\mathrm{K}\,\mathrm{C})\,\mathbf{x}$. For the helicopter flying in a quiescent environment with no external disturbances, the problem simplifies to finding an appropriate gain matrix K that guarantees asymptotic stability of closed loop dynamics, which can be easily solved by using modern control techniques such as LQR, pole placement etc.

5.3.1 Simulation and Results

The influence of the hair sensor array inputs when used in conjunction with the optic flow system is demonstrated by constructing a simulation and investigating the closed loop dynamics of the helicopter in quiescent flow. For the various simulations that follow, the hair array parameters are set as follows: $\phi_1 = \pi/8$ rad, $\phi_2 = 3\pi/8$ rad, radius of the hair sensor ring R=0.1 m.

The flight behaviour of the helicopter is studied for a set of trials chosen with initial perturbations having a mean of $[y_0, v_0, \psi_0, r_0]^T = [0.4\,\mathrm{m},\ 0.18\,\mathrm{m/s},\ 3\,\mathrm{deg},\ 17\,\mathrm{deg}\,/\mathrm{s}]^T$. The simulation of the helicopter flying in a quiescent environment along the length of a corridor with no external gusts is constructed. A snapshot of the corridor the helicopter navigates in and used in the simulation was shown in Fig. 4.5A. The gains corresponding to the visuomotor system are selected in a manner similar to the gains chosen in prior studies [26]. The gains corresponding to the hair sensor array are chosen so as to decouple the states v and r from one another by selecting the desired damping coefficient for the lateral and the yaw dynamics.

The results for 20 different trials are as shown in Figs.5.4, 5.5. From these plots of the closed loop dynamics, we see that by augmenting the optic flow outputs (and gains) with hair array outputs (and gains), we augment the stability of the helicopter through static output feedback making the vehicle more robust. Also, significant mitigation of the problems associated with performance and bandwidth limitations of the closed loop dynamics is clearly seen from the results.

The results demonstrate the feasibility of using hair sensor arrays to extract useful motion cues for stability and navigation for planar motion of a micro helicopter using optic flow-based WFI methodology. Sideslip is difficult to estimate for small fixed-wing UAVs and the use of hair array outputs to measure sideslip provides a significant benefit of the use of the sensory system. A simple 2-D model of the hair arrays located symmetrically around a circular ring is shown to result in efficient stability augmentation and mitigation of the limitations imposed on bandwidth and closed loop performance by using just optic flow inputs.

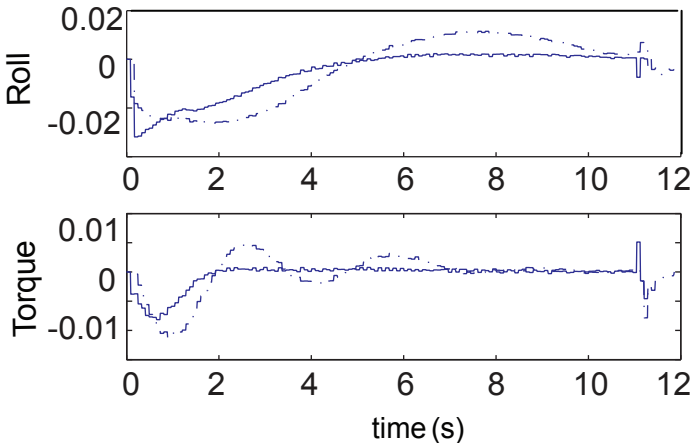

Figure 5.5: Mean control inputs for the set of small perturbations; Broken lines represent results using just optic flow, solid lines represent results with combined hair and optic flow outputs.

5.4 Gust Rejection in an Urban Environment

In this section, a spatially continuous representation response of the hair sensor over a hemispherical array is developed and a model for wide-field integration is introduced. Subsequently, a biologically consistent feedback architecture is developed by combining optic flow outputs with hair array outputs for detecting wind gust velocity. The wind gust velocity estimates are then used to reject gusts acting on a fixed wing MAV navigating in an urban environment.

5.4.1 Response of Hemispherical Hair Sensor

A spherical configuration is considered with the hair sensor array assumed to be uniformly distributed over the frontal hemisphere, where the flow as well as the boundary layer over the hair array is assumed to be laminar, with flow separation

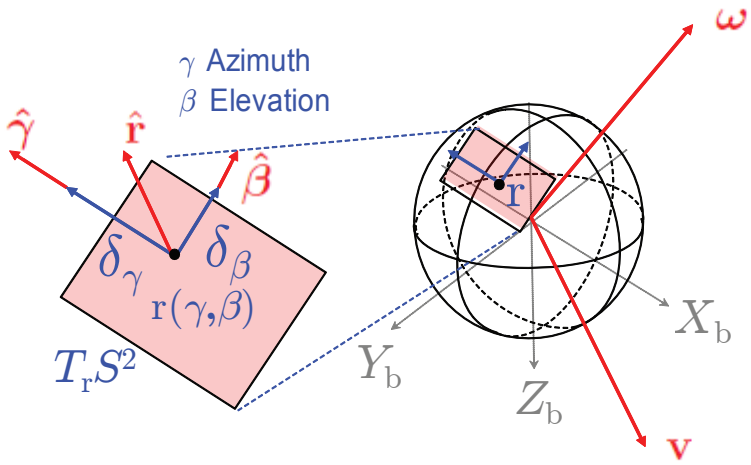

Figure 5.6: Hemispherical hair sensor array.

occurring over the rear end of the hemisphere. The interference effects of the hair sensor on the flow downstream is assumed to be negligible. A distributed array of hair sensors spread over the frontal hemisphere responds in flexure caused by tangential flow over the surface with each sensor output being proportional to the magnitude of the flexure root strain. In nominal state, the vehicle is assumed to have a reference velocity u_0 with the nominal velocity flow field across the surface leading to nominal response pattern across the sensor array. Perturbations to the nominal state causes perturbations to the nominal root strain, inducing changes in the sensor and cumulative array output. Hence, perturbations to the nominal state induces perturbations in the array output.

To obtain the hair sensor response at the location $r(\gamma,\, \beta)$ on the hemispherical surface , one begins by deriving the tangential velocity vector arising from both the translational and rotational components $\{u,\, v,\, w,\, p,\, q,\, r\}$ as well as gust $\mathbf{d} = [u_g,\, v_g,\, w_g,\, p_g,\, q_g,\, r_g]^T$.

The flow field due to the translational velocity is axisymmetric about the mean free stream velocity axis. Let γ, β and γ', β' be the spherical coordinates of the body defined in the body frame $\mathcal{B} = \{X_{\mathrm{b}},\, Y_{\mathrm{b}},\, Z_{\mathrm{b}}\}$ and the relative wind frame $\mathcal{W} = \{X_{\mathrm{W}},\, Y_{\mathrm{W}},\, Z_{\mathrm{W}}\}$ respectively. The axisymmetric unit tangent velocity vector at any point $\mathrm{r}(\gamma', \beta')$ arising from the translation of the body is,

$$\hat{\mathbf{r}}_{\mathbf{t}} = \sin\theta_t\,(-\hat{\mathbf{i}}_W) + \cos\theta_t\left(\cos\zeta_t(\hat{\mathbf{j}}_W) + \sin\zeta_t(\hat{\mathbf{k}}_W)\right),\ \cos\theta_t = \cos\gamma'\sin\beta',$$
$$\sin\zeta_t = \frac{\cos\beta'}{\sin\theta_t},\ \cos\zeta_t = \frac{\sin\beta'\sin\gamma'}{\sin\theta_t} \tag{5.8}$$

where ζ_t is the angle between the component of the tangent projected on the $Y_W - Z_W$ plane and Y_W axis (Fig. 5.7). The translational velocity vector at $\mathrm{r}(\gamma', \beta')$ defined in the relative wind frame then becomes

$$\mathbf{v}_{\mathbf{trans}} = \frac{3}{2}V_\infty \sin\theta_t\,\hat{\mathbf{r}}_{\mathbf{t}} \tag{5.9}$$

The velocity vector needs to be defined in spherical coordinates attached to the body frame. Towards that end, the transformation from body frame to relative wind frame is accomplished by the matrix,

$$T_{WB} : \mathbb{R}^3_B \mapsto \mathbb{R}^3_W,\ T_{WB} = \begin{bmatrix} \cos\alpha\cos\beta & \sin\beta & \sin\alpha\cos\beta \\ -\cos\alpha\sin\beta & \cos\beta & -\sin\alpha\sin\beta \\ -\sin\alpha & 0 & \cos\alpha \end{bmatrix}.$$

Furthermore, the transformation from rectangular coordinates to spherical coordinates is accomplished by the matrix

$$T_{SR} = \begin{bmatrix} \cos\gamma\sin\beta & \sin\gamma\sin\beta & \cos\beta \\ -\sin\gamma & \cos\gamma & 0 \\ -\cos\gamma\cos\beta & -\sin\gamma\cos\beta & \sin\beta \end{bmatrix}$$

Finally, the relative wind frame coordinates γ', β' can be related to the body fixed coordinates γ, β through the transformation

$$\begin{Bmatrix} \cos\gamma' \sin\beta' \\ \sin\gamma' \sin\beta' \\ \cos\beta' \end{Bmatrix} = T_{WB} \begin{Bmatrix} \cos\gamma \sin\beta \\ \sin\gamma \sin\beta \\ \cos\beta \end{Bmatrix} \tag{5.10}$$

For small perturbations of the body and wind velocity components from the nominal flow field, we have the following:

$$\begin{aligned} u_0\beta_{\text{ss}} &= v - v_g,\ u_0\alpha = w - w_g \\ V_\infty &= u_0 + u - u_g \end{aligned} \tag{5.11}$$

where, α and β_{ss} are the vehicle angle of attack and sideslip respectively, V_∞ is the freestream flow velocity and $\{u_g,\ v_g,\ w_g\}$, $\{p_g,\ q_g,\ r_g\}$ are the respectively wind translational and rotational velocities defined in the body frame $\mathcal{B}$.

Then from (5.8) and (5.10), the tangential velocity field over the spherical surface due to translation described fully in body-fixed spherical coordinates can be obtained as,

$$\mathbf{v_{trans}} = \frac{3}{2}V_\infty \left[\sin(\gamma - \beta_{\text{ss}})\,\hat{\boldsymbol{\gamma}} - (\cos\beta\cos(\gamma - \beta) - \alpha\sin\beta)\,\hat{\boldsymbol{\beta}}\right] \tag{5.12}$$

In addition to body translation, the rotation of the body also contributes to the the response of the hair sensor arrays. Accordingly, the relative wind velocity at any point r(γ, β) defined in body-fixed coordinates needs to be derived.

$$\mathbf{v_{rot}} = -\boldsymbol{\omega} \times \mathbf{r} \tag{5.13}$$

$\boldsymbol{\omega} = (p - p_g)\,\hat{\mathbf{i}}_B + (q - q_g)\,\hat{\mathbf{j}}_B + (r - r_g)\,\hat{\mathbf{k}}_B$ defines the angular velocity of the body with $\{p,\, q,\, r\}$ and $\{p,\, q,\, r\}$ being the rotational (roll, pitch and yaw) rates of the vehicle and gust respectively defined in the body frame. and,

$$\mathbf{r}(\gamma, \beta) = R\cos\gamma\sin\beta\,\hat{\mathbf{i}}_B + R\sin\gamma\sin\beta\,\hat{\mathbf{j}}_B + R\cos\beta\,\hat{\mathbf{k}}_B \tag{5.14}$$

with R being the radius of the hemisphere. Switching from rectangular coordinates to spherical coordinates, the resulting rotational component of the relative wind velocity is given by,

$$\begin{aligned}\mathbf{v_{rot}} = {} & [R((q - q_g)\sin\gamma\cos\beta - (r - r_g)\sin\beta + (p - p_g)\cos\beta\cos\gamma)]\,\hat{\boldsymbol{\gamma}} - \\ & [R((q - q_g)\cos\gamma - (p - p_g)\sin\gamma)]\,\hat{\boldsymbol{\beta}}\end{aligned} \tag{5.15}$$

The total relative wind velocity is then given by

$$\mathbf{v} = \mathbf{v_{trans}} + \mathbf{v_{rot}}$$

or,

$$\begin{aligned}\mathbf{v} = {} & \left[\frac{3}{2}V_\infty\sin(\gamma - \beta_{\text{ss}}) + R((q - q_g)\sin\gamma\cos\beta - (r - r_g)\sin\beta + (p - p_g)\cos\beta\cos\gamma)\right]\hat{\boldsymbol{\gamma}} - \\ & \left[\frac{3}{2}V_\infty(\cos\beta\cos(\gamma - \beta_{\text{ss}}) - \alpha\sin\beta) + R((q - q_g)\cos\gamma - (p - p_g)\sin\gamma)\right]\hat{\boldsymbol{\beta}}\end{aligned} \tag{5.16}$$

We notice that the velocity vector resides in the tangent space $T_{\text{r}}S^2$ at $\text{r}(\gamma, \beta)$.

The sensor output is then given by

$$\boldsymbol{\delta}(\mathbf{x}, \gamma, \beta) = K_p||\mathbf{v}||\mathbf{v}. \tag{5.17}$$

where $\mathbf{v}(\mathbf{x}, \gamma, \beta)$ is the incident flow velocity vector obtained in (5.16). Substituting the expression for $\mathbf{v}$ from (5.16) and truncating the resulting expression to first order

terms, the quantity $\frac{1}{K_p}\boldsymbol{\delta}(\mathbf{x},\gamma,\beta) = \delta_\gamma\hat{\boldsymbol{\gamma}} + \delta_\beta\hat{\boldsymbol{\beta}}$ has components along the azimuth γ and elevation β directions and resides in the vector space of piecewise continuous, square integrable functions on the sphere:

$$L^2(S^2,\mathbb{R}^2) = \left\{ \mathbf{f} = \begin{bmatrix} f_1(\mathbf{r}) \\ f_2(\mathbf{r}) \end{bmatrix} : \mathbf{r} \in S^2, f_k(\mathbf{r}) \in L^2(S^2), k = 1,2 \right\} \tag{5.18}$$

The component sensor response δ_γ and δ_β at any point r(γ, β) on the surface can be obtained as,

$$\begin{bmatrix} \delta_\gamma \\ \delta_\eta \end{bmatrix} = \begin{bmatrix} \delta_{\gamma_u} & \delta_{\gamma_\alpha} & \delta_{\gamma_{\beta_{\mathrm{ss}}}} & \delta_{\gamma_p} & \delta_{\gamma_q} & \delta_{\gamma_r} \\ \delta_{\beta_u} & \delta_{\beta_\alpha} & \delta_{\beta_{\beta_{\mathrm{ss}}}} & \delta_{\beta_p} & \delta_{\beta_q} & \delta_{\eta_r} \end{bmatrix} \begin{bmatrix} (u_0^2 + 2u_0(u-u_g)) \\ u_0^2\alpha \\ u_0^2\beta_{\mathrm{ss}} \\ u_0R(p-p_g) \\ u_0R(q-q_g) \\ u_0R(r-r_g) \end{bmatrix}$$

where,

$$
\begin{aligned}
\delta_{\gamma_u} &= \left(\frac{3}{2}\right)^2 \sin\gamma\sqrt{1-(\cos\gamma\sin\beta)^2}, \\
\delta_{\gamma_\alpha} &= -\left(\frac{3}{2}\right)^2 \frac{\cos\beta\cos\eta\sin\gamma\cos\gamma}{\sqrt{1-(\cos\gamma\sin\beta)^2}}, \\
\delta_{\gamma_{\beta_{\mathrm{ss}}}} &= -\left(\frac{3}{2}\right)^2 \cos\gamma\frac{1-(\cos\gamma\sin\beta)^2+(\sin\beta\sin\gamma)^2}{\sqrt{1-(\cos\gamma\sin\beta)^2}}, \\
\delta_{\gamma_p} &= \left(\frac{3}{2}\right)\cos\beta\cos\gamma\sqrt{1-(\cos\gamma\sin\beta)^2}, \\
\delta_{\gamma_q} &= \left(\frac{3}{2}\right)\sin\gamma\cos\beta\frac{2-(\cos\gamma\sin\beta)^2}{\sqrt{1-(\cos\gamma\sin\beta)^2}}, \\
\delta_{\gamma_r} &= -\left(\frac{3}{2}\right)\sin\beta\frac{1-(\cos\gamma\sin\beta)^2+(\sin\gamma)^2}{\sqrt{1-(\cos\gamma\sin\beta)^2}}, \\
\delta_{\beta_u} &= -\left(\frac{3}{2}\right)^2 \cos\beta\cos\gamma\sqrt{1-(\cos\gamma\sin\beta)^2}, \\
\delta_{\beta_\alpha} &= \left(\frac{3}{2}\right)^2 \sin\beta\frac{1-(\cos\gamma\sin\beta)^2+(\cos\gamma\cos\beta)^2}{\sqrt{1-(\cos\gamma\sin\beta)^2}}, \\
\delta_{\beta_{\beta_{\mathrm{ss}}}} &= -\left(\frac{3}{2}\right)^2 \sin\gamma\cos\beta\frac{1-2(\sin\beta\cos\gamma)^2}{\sqrt{1-(\cos\gamma\sin\beta)^2}}, \\
\delta_{\beta_p} &= \left(\frac{3}{2}\right)\sin\gamma\sqrt{1-(\cos\gamma\sin\beta)^2}, \\
\delta_{\beta_q} &= -\left(\frac{3}{2}\right)\cos\gamma\frac{1-(\cos\gamma\sin\beta)^2+(\cos\beta)^2}{\sqrt{1-(\cos\gamma\sin\beta)^2}}, \\
\delta_{\beta_r} &= \left(\frac{3}{2}\right)\frac{\sin\gamma\cos\gamma\cos\beta\sin\beta}{\sqrt{1-(\cos\gamma\sin\beta)^2}}. \qquad (5.19)
\end{aligned}
$$

The nominal (axisymmetric) tip deflection pattern at the reference forward speed u_0 is shown in Fig. 5.8.

5.4.2 WFI-based Decompositions of Hemispherical Hair Sensor Array

This section outlines the framework for pooling the response of individual sensors distributed over the hemisphere that contribute to the combined output and

the inversion technique for minimising the noise throughput to generate the required state estimates.

As noted in the earlier section, there are various similarities between the insect visuomotor system and the wind-hair mechanosensory system. Spatial pooling of the response of wind-hair sensilla occurs in a manner analogous to optic flow. Real spherical harmonics are again used as weighting functions to extract motion cues by parsing hair sensor response along the azimuthal and elevation directions. The WFI-based decompositions of the hair sensor response over the hemispherical array are given by,

$$y^k_{l,m} = \frac{1}{K_p}\langle \boldsymbol{\delta}, \mathbf{F}^h(\gamma,\, \beta)\rangle = \frac{1}{K_p}\int_{S^2} \boldsymbol{\delta}\,.\,\mathbf{F}^h(\gamma,\, \beta)\, d\Omega. \tag{5.20}$$

where $\mathbf{F}^h = Y_{l,m}(\gamma, \beta)\hat{\mathbf{k}}$, $k \in \{\gamma, \beta\}$ are the spherical harmonics along azimuth and elevation directions that form an orthogonal basis over the sphere S^2, given by (2.5).

The wide-field spatial pooling of individual sensor outputs is used in generating motion cues from the mechanosensory system. For instance, $y^{\beta}_{0,0}$ quantifies the goodness of the match between the sensor response induced by the flow and the transverse template pattern $Y_{0,0}\hat{\boldsymbol{\beta}}$ having a constant magnitude at all points on the spherical surface. A perturbation induced by a climbing vehicle can be captured by output $y^{\beta}_{0,0}$. The lateral asymmetry introduced by lateral velocity or sideslip β_{ss} can be extracted by the sensitivity function that is symmetric about the longitudinal axis in the vertical plane and antisymmetric in the horizontal plane, such as $Y_{3,-1}\hat{\boldsymbol{\gamma}}$ or $Y_{3,-3}\hat{\boldsymbol{\gamma}}$, while transverse and lateral asymmetry introduced by the roll rate p can be estimated by functions that are antisymmetric in the vertical plane, such as $Y_{3,2}\hat{\boldsymbol{\beta}}$.

Given $p \geq n$ spherical harmonics $\mathbf{F}^h = \{\mathbf{F}^h_j,\ j = 1...p\}$, for small perturbations about the reference flight condition $\mathbf{x}_{\text{ref}}$, the linear hair array outputs, accounting for measurement noise, can be written in the form

$$\tilde{\mathbf{y}}^h = C\mathbf{x} + C_0 + \mathbf{w} \tag{5.21}$$

where, $\tilde{\mathbf{y}}^h \in \mathbb{R}^p$ are the measured hair array outputs, the noise $\mathbf{w}$ is zero mean $E\{\mathbf{w}\} = 0$ with known covariance $E\{\mathbf{w}\mathbf{w}^T\} = R_{\mathbf{w}}$. The quantity $C_0 = \frac{1}{K_p}\langle\, \boldsymbol{\delta}|_{\mathbf{x}_{\text{ref}}},\ \mathbf{F}^h\,\rangle$ represents the nominal array output corresponding to the reference state $\mathbf{x}_{\text{ref}}$. The solution to the static estimation problem of the overdetermined, inconsistent set of linear equations, given by (5.21), is given by the weighted least squares estimator, $C_h^\dagger = (C^T W C)^{-1} C^T W$, which is used to generate optimal estimates $\hat{\mathbf{x}} = C_h^\dagger \tilde{\mathbf{y}}^h$ that minimises noise throughput. Hair sensor output measurements across the imaging surface are assumed to be affected by zero mean additive noise $\boldsymbol{\eta}(\gamma,\ \beta)$ with variance σ_n^2 with no correlation between measurement nodes or with signal amplitude. Measurement noise at the output can then be written as $\mathbf{w} = \langle \boldsymbol{\eta},\ \mathbf{F}\rangle$. Using linearity of the WFI operator (5.20) and the properties of the covariance matrix, we have,

$$R_{\mathbf{w}ij} = \Delta\beta\, \Delta\gamma \sigma_n^2 \langle \mathbf{F}^h_i,\ \mathbf{F}^h_j \rangle \tag{5.22}$$

where $\Delta\gamma$, $\Delta\beta$ is the spacing between successive viewing stations along the azimuthal and elevation directions respectively. For the present application, successive measurement nodes are assumed to be uniformly distributed across the frontal hemisphere with a separation of 9 deg. Hence, $\Delta\gamma, \Delta\beta$ are set to 9 deg.

The relative state estimates $\hat{\mathbf{x}}$ are optimal with respect to the span of the basis function set $\mathbf{F}^h$. Inclusion of spherical harmonics to a high degree is sufficient to

achieve convergence to the global optimum over $L_2(S^2, \mathbb{R}^2)$. For the relative state estimates $\hat{\mathbf{x}} = C_h^\dagger \tilde{\mathbf{y}}^h$ with $\tilde{\mathbf{y}}^h = \frac{1}{K_p}\langle \boldsymbol{\delta} - \boldsymbol{\delta}|_{\mathbf{x}_{\text{ref}}}, \mathbf{F}^h \rangle$, the linearity of the WFI operator allows computing state estimates using the state extraction pattern $\mathbf{F}^h_{\hat{\mathbf{x}}}$, given by,

$$\hat{\mathbf{x}} = \frac{1}{K_p}\langle \boldsymbol{\delta} - \boldsymbol{\delta}|_{\mathbf{x}_{\text{ref}}}, \mathbf{F}^h_{\hat{\mathbf{x}}} \rangle, \; \mathbf{F}^h_{\hat{\mathbf{x}}} = C_h^\dagger \mathbf{F}^h \tag{5.23}$$

Taking the inner product of the state extraction patterns with the instantaneous optic flow pattern results in velocity estimates with minimal noise throughput. The optimal state extraction patterns are shown in Fig. 5.9. As is apparent from the plots, hair array outputs can be used to generate an estimate of the relative wind velocity states $\{u - u_g,\, v - v_g,\, w - w_g,\, p - p_g,\, q - q_g,\, r - r_g\}$ of the vehicle. These estimates can then be combined with optic flow outputs that generate body state estimates to decouple wind velocity and body velocity states of the system.

5.4.3 Feedback Control Design

In this section, the state estimates generated by the visuomotor and the mechanosensory hair systems are used in design of controller gains for gust alleviation of a vehicle flying autonomously through a gusty environment as it demonstrates safe obstacle avoidance behavior. The control objective is to regulate the relative state estimates provided by visuomotor and hair sensor systems to reference values, while simultaneously alleviating gust effects resulting in stable obstacle avoidance behaviour. The salient features of the control design philosophy are listed below.

Static (as opposed to dynamic) compensation is employed yielding a fast and

efficient computation paradigm. The vehicle considered is a highly maneuverable fixed wing MAV developed by Aurora Flight Sciences Inc., weighing 680 g, with a payload of 227 g and with a wing span of 1.7 ft. The vehicle attains a nominal flight speed of 7 m/s. The complete three dimensional motion of the vehicle with six degrees of freedom is considered. Small perturbation theory is invoked in developing the state equations, which is given by (5.24).

$$\begin{bmatrix} \dot{u} \\ \dot{w} \\ \dot{q} \\ \dot{\theta} \\ \dot{v} \\ \dot{p} \\ \dot{r} \\ \dot{\phi} \end{bmatrix} = \begin{bmatrix} 0.036 & -1.93 & 1.92 & 9.81 & 0 & 0 & 0 & 0 \\ 1.78 & -5.82 & 4.61 & 0 & 0 & 0 & 0 & 0 \\ 2.20 & -15.261 & -12.21 & 0 & 0 & 0 & 0 & 0 \\ 0 & 0 & 1 & 0 & 0 & 0 & 0 & 0 \\ 0 & 0 & 0 & 0 & -0.39 & 2.21 & 6.46 & 9.81 \\ 0 & 0 & 0 & 0 & -15.54 & -4.72 & -4.8158 & 0 \\ 0 & 0 & 0 & 0 & -2.26 & 0.39 & -1.39 & 0 \\ 0 & 0 & 0 & 0 & 0 & 1 & 0 & 0 \end{bmatrix} \begin{bmatrix} u \\ w \\ q \\ \theta \\ v \\ p \\ r \\ \phi \end{bmatrix}$$

$$+ \begin{bmatrix} 1 & 0 & 0 & 0 \\ 0 & 0 & 0 & 0 \\ 0 & 0 & 1 & 0 \\ 0 & 0 & 0 & 0 \\ 0 & 0 & 0 & 0 \\ 0 & -1 & 0 & 0 \\ 0 & 0 & 0 & 1 \\ 0 & 0 & 0 & 0 \end{bmatrix} \begin{bmatrix} F_x \\ LL \\ MM \\ NN \end{bmatrix} + \begin{bmatrix} -0.036 & 0 & 0 & 0 & 0 & 0 \\ 0 & 0 & 0 & 5.82 & 0 & 0 \\ 0 & 0 & 0 & 0 & 12.21 & 0 \\ 0 & 0 & 0 & 0 & 0 & 0 \\ 0 & 0.39 & 0 & 0 & 0 & 0 \\ 0 & 0 & 0 & 4.72 & 0 & 0 \\ 0 & 0 & 0 & 0 & 0 & 1.39 \\ 0 & 0 & 0 & 0 & 0 & 0 \end{bmatrix} \begin{bmatrix} u_g \\ v_g \\ w_g \\ p_g \\ q_g \\ r_g \end{bmatrix} \quad (5.24)$$

The above equation can be written in the standard form $\dot{\mathbf{x}} = A\mathbf{x} + B\mathbf{u} + D\mathbf{d}$, with

A, B, D having their usual meaning. Throttle, and the three turning moments - roll, pitch and yaw - provide actuation of the vehicle, with the control saturation limits being $|F_{x_t}| \leq 7$, $|LL| \leq 10$, $|MM| \leq 10.3$, $|NN| \leq 10.5$. The reference for the state vector $\mathbf{x} = \{y, z, u, v, w, \phi, \theta, \psi, p, q, r\}$ that accounts for the pitch and thrust deviation required to attain a nominal speed of 7 m/s is given by $\mathbf{x}_{\text{ref}} = \{0, -K_{z_\theta}(\hat{\theta} - \tilde{\theta}), 7, 0, 2.135, 0, 0.305, 0, 0, 0, 0\}$. The reference K_{z_θ} is set to 3.5, which, as before in chapter 4, helps the vehicle surmount vertical obstacles by spiking the reference altitude temporarily. Also, as before, in addition to the optic flow and hair array sensors, the vehicle deploys a pitch sensor and an altitude sensor (sonar), generating near perfect pitch and altitude measurements respectively, that are available for feedback. Hence, the optic flow system generates estimates for the nine body states $\{y, u, v, w, \phi, \psi, p, q, r\}$, while the hair sensor system (in conjunction with the optic flow system) generates the six wind (gust) velocity estimates. The optimal weighting patterns for the body and wind states are:

$$\begin{aligned} \hat{x}_i &= \langle \dot{\mathbf{Q}}, \mathbf{F}_{x_i} \rangle + C^{\dagger}_{i,M+1} \bar{z} \\ \hat{d}_j &= \langle \dot{\mathbf{Q}}, \mathbf{F}_{x_j} \rangle - \langle \frac{1}{K_p}(\delta - \delta|_{\text{ref}}), \mathbf{F}^h_{(x-d)_j} \rangle. \end{aligned} \tag{5.25}$$

where $\bar{z}$ denotes sonar altitude measurements, $i = \{y, u, v, w, \phi, \theta, \psi, p, q, r\}$ denote the set of optic flow state estimates, $j = \{u, v, w, p, q, r\}$ denote the velocity estimates and d denotes the wind velocity estimates generated by the combined action of the hair and optic flow systems. $C^{\dagger}$ is the weighted least squares minimum variance estimator from chapter 2, that generates body state estimates with minimal noise and environment uncertainty throughput.

The gust velocity estimates are generated from the variation of hair sensor response across the surface of the sphere. The relationship between the hair sensor response and the velocity states is basically quadratic (5.17), which has been approximated as a linear model for small gust disturbance (5.25). Larger the gust disturbances or greater the deviation of the vehicle body states from the target state, greater the deviation of the linear gust estimates from their true values. As gust rejection performance is completely determined by the accuracy of the gust velocity estimates, the linear gust estimation process for the highly maneuverable vehicle would not be sufficiently accurate for the purpose of adequate gust alleviation. It then becomes imperative to consider the complete non linear model in estimating gust velocities. Hence, the linear model for generating the gust velocity estimates (5.25) is replaced with the complete nonlinear model.

Given the hair sensor array outputs $\tilde{\mathbf{y}}^h$ and the body state estimates from optic flow outputs, the equation $\tilde{\mathbf{y}}^h - \mathbf{v}|\mathbf{v}| = 0$ needs to be solved for the gust velocities $\mathbf{d} = \{u_g, v_g, w_g, p_g, q_g, r_g\}^T$. Broyden's iterative root-finding algorithm [95] lends itself very well to the present application and is used to generate the gust estimate from the non linear model. The method requires an initial guess, as well as the approximation of the inverse of the Jacobian matrix at the initial guess estimate. The iterative algorithm is given by,

$$\mathbf{d}_{n+1} = \mathbf{d}_n + \mathbf{J}_n^{-1}(\tilde{\mathbf{y}}^h - \mathbf{v}_n|\mathbf{v}_n|) \tag{5.26}$$

with $\mathbf{J}_0^{-1} = C_h^\dagger$ being the Jacobian and the linear gust estimate (5.25) chosen as the initial guess estimate $\mathbf{d}_0$.

The objective of gust rejection is achieved through feedforward control using gust velocity estimates, given by $\mathbf{u}_{\text{ff}} = -B^{-1}D\hat{\mathbf{d}}$. However, referring to the control input matrix B given in (5.24), it is apparent that perfect gust alleviation cannot be achieved as control authority is insufficient to negate lateral and transverse gusts v_g and w_g. Therefore, H_∞ control strategy with state feedback is employed to mitigate the througput of v_g, w_g components of gust, while the rest of the components are negated directly by the feedforward mechanism. The methodology for generating static H_∞ feedback gains for gust mitigation, which was developed in a prior study [96], was adopted for deriving feedback gains for the fixed wing MAV. The state penalty matrix is set to $J_{\mathbf{x}} = \text{diag}\{1, 100, 1, 1, 100, 100, 400, 1, 1, 0.25, 1\}$ and the control penalty matrix is set to $J_{\mathbf{u}} = \text{diag}\{1, 1, 1, 1\}$. The control gains are chosen so as to ensure vehicle stability across the family of different environments described in section 2.2. This is done by analyzing for linear stability analysis that proceeds by ensuring the eigenvalues of $A_{\text{cl}} = (A - BKC^{\dagger}C)$ across the family of modeled environments lie in the open left half plane. The control gains are given in table 5.2. The resulting poles of the closed loop system for each of the limiting cases is shown in Fig. 5.10. Thus, the gust velocity estimates are used to achieve near-perfect rejection of those gust components with adequate control authority, while the static feedback gains that act on the body state estimates generated by the optic flow system ensure stable obstacle avoidance behaviour through state feedback.

Table 5.2: H_∞ static feedback gains K

Throttle	Roll	Pitch	Yaw
$K_{F_{x,y}} = 0.00$	$K_{L_y} = 0.13$	$K_{M_y} = 0.00$	$K_{N_y} = 1.00$
$K_{F_{x,z}} = -3.64$	$K_{L_z} = 0.00$	$K_{M_z} = -17.78$	$K_{N_z} = 0.00$
$K_{F_{x,u}} = 4.06$	$K_{L_u} = 0.00$	$K_{M_u} = -0.53$	$K_{N_u} = 0.00$
$K_{F_{x,v}} = 0.00$	$K_{L_v} = 0.40$	$K_{M_V} = 0.00$	$K_{N_v} = 1.62$
$K_{F_{x,w}} = 4.21$	$K_{L_w} = 0.00$	$K_{M_w} = -4.45$	$K_{N_w} = 0.00$
$K_{F_{x,\phi}} = 0.00$	$K_{L_\phi} = -3.22$	$K_{M_\phi} = 0.00$	$K_{N_\phi} = -4.38$
$K_{F_{x,\theta}} = -33.67$	$K_{L_\theta} = 0.00$	$K_{M_\theta} = 66.32$	$K_{N_\theta} = 0.00$
$K_{F_{x,\psi}} = 0.00$	$K_{L_\psi} = 2.37$	$K_{M_\psi} = 0.00$	$K_{N_\psi} = 11.49$
$K_{F_{x,p}} = 0.00$	$K_{L_p} = -0.51$	$K_{M_p} = 0.00$	$K_{N_p} = -0.48$
$K_{F_{x,q}} = -0.53$	$K_{L_q} = 0.00$	$K_{M_q} = 3.61$	$K_{N_q} = 0.00$
$K_{F_{x,r}} = 0.00$	$K_{L_r} = 0.4828$	$K_{M_r} = 0.00$	$K_{N_r} = 5.79$

5.4.4 Simulation

In this section, the efficacy of using the hair sensor system for the purpose of gust rejection is investigated. Various controller architectures are considered and results are presented for simulation of the fixed wing micro-air-vehicle subjected to sustained gust flying in an outdoor urban environment (Fig. 4.7). Optic flow estimates provide sufficient motion cues for vehicle stabilization and navigation. In addition, the hair sensor system is used to estimate gust velocities accurately.

The simulation process for the combined use of the optic flow and the hair mechanosensory systems in achieving stable obstacle avoidance behaviour as well as efficient gust rejection performance of the vehicle is shown in Fig. 5.11. The feedforward gain $K_{\text{ff}} = B^{-1}D$ helps achieve gust mitigation while the feedback gain K, shown in table 5.2 helps achieve stable obstacle avoidance behavior. The gust profiles are generated by the Dryden model described by (4.1).

5.4.4.1 Static Controller Framework-Based Navigation of the Urban Environment

The static feedback gains are coupled to the static estimator (Fig. 5.25) for enabling safe relexive navigation in the urban environment. As the emphasis of current study is demonstration of collision avoidance by gust rejection using hair sensory arrays, a single nominal trajectory in the absence of gust as well as the influence of the hemispherical hair sensor array on vehicle trajectories for 20 different sets of gust profiles are looked at. The nominal trajectory of the vehicle flying in

the absence of gust is shown in Fig. 5.12. The vehicle pose, proximity and velocity variation with time is shown in Fig. 5.13. As can be seen from the figure, safe collision avoidance behavior of the highly agile vehicle results in substantial deviation of the state estimates from the target state, especially during the first right turn of the vehicle, requiring the nonlinear model of the hair sensor array response for accurate gust estimation.

Gust causes deviation from the nominal trajectory, with larger gust throughput resulting in greater deviation from the nominal case. The combined trajectories obtained by the vehicle flying with just the optic flow sensor enabled is shown in Fig. 5.14A for all the gust cases. As can be seen from the figure, optic flow based navigation of a cluttered environment results in collision in multiple instances, making navigation hazardous in the presence of gusts. The activation of the hair sensor system also results in mutiple collisions (Fig. 5.14B), resulting in a marginal improvement in the collision avoidance behavior of the vehicle. The time history of the vehicle velocity as well as the gust component velocity states for a sample trajectory from Fig. 5.14B are shown in Fig. 5.15. A sharp maneuver (during the first right turn) causes large deviation from the true states of the vehicle. It is apparent that the deviation in the gust velocity estimates from their true values coincide with the deviation in the estimates of vehicle velocity from their true values. This can clearly be seen in the Fig. 5.16, where the relative wind velocity estimates, generated by the hair sensor system, coincide with their true values. Hence, poor gust velocity estimation, caused by poor body velocity estimation, gives rise to poor gust rejection performance, causing multiple collisions in Fig. 5.14B.

An improvement in the vehicle's gust rejection performance then requires better accuracy in body velocity estimates than that obtained using optic flow. The niche of optic flow-based sensing is proximity and pose estimation. Thus, an alternate approach based on a combination of a triaxial GPS and rate gyro unit is considered for generating accurate velocity estimates. The GPS and rate gyro units operate at 10 and 50 Hz, with an accuracy of ± 0.2 m/s and ± 0.1 deg/s [97], generating near-accurate estimates of vehicle translational and rotational velocity respectively. Static estimation and compensation framework is again employed, with optic flow used to sense vehicle pose and proximity, while GPS and rate gyro units are used to detect vehicle velocity.

The nominal trajectory in the absence of gust is shown in Fig. 5.17. Improved velocity estimation clearly results in a change in the trajectory when compared with Fig. 5.12. The results with and without the hair sensor system are shown in Fig. 5.18. The vehicle manages to negotiate the environment in a safe manner using just optic flow, with the hair sensor system again exerting a marginal influence on the vehicle's collision avoidance behavior. Fig. 5.19 shows the comparison of the body and gust velocity estimates with the true states for a sample trajectory from Fig. 5.18B. It is apparent that the increase in accuracy of the body velocity estimates results in near accurate gust velocity estimation.

As noted earlier, the gust velocity components v_g, w_g are not directly negated with feedforward control, and their combined influence on the vehicle dynamics could be the reason for the negligible improvement in the vehicle's performance despite accurate gust velocity estimation. To confirm this supposition, the vehicle

trajectories with just the 4 components of gust ($\{u_g,\, p_g,\, q_g\, r_g\}$) that are directly negated with the hair sensor array are considered. The results are shown in Fig. **??**. It is apparent that the hair sensor system exerts a significant influence on the vehicle dynamics and manages to reject gust completely, resulting in vehicle trajectories that are similar to the nominal trajectory (Fig. 5.17). Hence, in this case, near perfect gust rejection using hair sensor arrays results in safe collision avoidance behavior.

5.4.4.2 Kalman Filter-Based Navigation of the Urban Environment

Finally, to complete the study, a brief discussion of an alternative to the static controller framework, based on the Kalman filter, for the purpose of accurate velocity estimation is included. The static estimator used above is replaced with the Kalman filter which is a dynamic estimator. A well known property of the Kalman filter is capability of state estimation in the absence of a full state estimate. Thus, Kalman filter can be used to generate wind velocity estimates in addition to body state estimates using just optic flow outputs, precluding the need for the hair sensor system. Using the optic flow measurement model developed in section 2.3, the dynamic estimate of the augmented state $\mathbf{x}_a = \{\mathbf{x},\, \mathbf{d}\}^T$ can be obtained from,

$$\dot{\hat{\mathbf{x}}}_a = A_a\hat{\mathbf{x}}_a + B_a\mathbf{u} + L(\tilde{\mathbf{y}} - C_{\mathrm{m}}\hat{\mathbf{x}}_a) \tag{5.27}$$

where $L = PC_{\mathrm{m}}^T R^{-1}$ is the Kalman gain, $R = R_w + R_{\Delta C}$ is the covariance matrix that penalizes high measurement noise and environment uncertainty in the output measurements, $\tilde{\mathbf{y}}$ are the outputs obtained from the spherical optic flow model and

C_{m} is the mean of the limiting cases of the environments considered in section 2.2. P is obtained from the equation

$$A_a P + P A_a^T + D D^T - P C_{\mathrm{m}} R^{-1} C_{\mathrm{m}} = 0$$

The augmented matrices A_a, B_a are given by,

$$A_a = \begin{bmatrix} A & DC_w \\ 0 & A_w \end{bmatrix}, \; B_a = \begin{bmatrix} B \\ u \end{bmatrix},$$

The dynamics of the gust filter is given by,

$$\begin{aligned} \dot{\mathbf{x}}_w &= A_w \mathbf{x}_w + B_w \mathbf{n} \\ \hat{\mathbf{d}} &= C_w \mathbf{x}_w + D_w \mathbf{n} \end{aligned} \tag{5.28}$$

where $\mathbf{n}$ is white noise input. Thus, the gust filter dynamics is used to estimate the gust velocity $\hat{\mathbf{d}}$. The gust dynamics that generates estimates of the Dryden gust profile is described in a prior study [96]. The simulation process used is again given by Fig. 5.11, where the static H_∞ feedback gain K is given in table 5.2 and the feedforward control input $\mathbf{u}_{\mathrm{ff}}$ negates gust using the wind velocity estimates $\hat{\mathbf{d}}$ generated by the dynamic estimator in the absence of the hair sensory system.

When implemented on the fixed wing MAV, the Kalman filter results in a negligible improvement in the gust rejection performance of the vehicle (Fig. 5.21), again leading to multiple collisions for several different gust profiles. It is seen that the gust velocity estimates show poor convergence with the true values. One possible explanation could be the inability of the dynamic estimator to incorporate environment structural uncertainty in a straightforward manner. The combination

of environment structural uncertainty and gust disturbance results in the poor performance of the dynamic estimator, which is reflected in the performance of the vehicle as it navigates the cluttered environment.

5.4.5 Discussion

The motion cues generated by the optic flow system employing static controller framework is sufficient to safely navigate the cluttered environment if perfect gust rejection takes place. The hair sensor arrays manage to generate accurate relative wind velocities using the non-linear hair estimation model from section 5.4.3. The study highlights the need for accurate gust velocity estimates for perfect gust rejection, which in turn depend on accurate body velocity estimates derived from the optic flow outputs. Thus, it is seen that the performance of the hair sensor system depends on the performance of the optic flow system. In addition, the hair sensor system is seen to be especially useful if sufficient control authority exists to negate the most important components of gust in a feedforward manner. Thus, given these conditions, the hair sensor system is well suited for gust rejection applications.

The hair sensor arrays generate motion cues such as sideslip and angle-of-attack, which are particularly difficult to estimate using lightweight miniature sensors embedded on microsystems, in a computationally efficient manner, thus precluding the need for an extensive wind velocity estimating apparatus as well as complicated processing algorithms [12]. The methodology proposed in this chapter is certainly feasible as lightweight triaxial GPS and rate gyro sensors have been

used extensively on existing MAVs for accurate translational and rotational velocity estimation [5, 98]. Given the current lack of sensors with the required size and bandwidth capabilities, coupling the optic flow sensor with hair sensor arrays in a static controller framework provides an attractive alternate paradigm for MAV navigation applications.

Finally, with regard to a comparison of the static controller framework using hair sensor arrays with the dynamic H_∞ controller framework that exclusively utilizes optic flow outputs, it is seen that both approaches successfully overcome the optic flow output deficiency in planar motion. Simulation-based validation studies of both approaches demonstrate improved closed loop performance and bandwidth for navigation applications. Additionally, both static and dynamic controller frameworks are seen to account for environment uncertainty as well as mitigate gusts in a straightforward manner. Both approaches are used to demonstrate safe reflexive 3D navigation behavior in an cluttered, urban environment subjected to gusts. Finally, both approaches are computationally efficient - H_∞ loop shaping approach results in a low order dynamic gain, while static compensation using hair sensor arrays allows offline computation of the corresponding gains. This is especially true of planar navigation applications. It is seen that both approaches enable autonomous reflexive navigation in outdoor, gusty and uncertain environments.

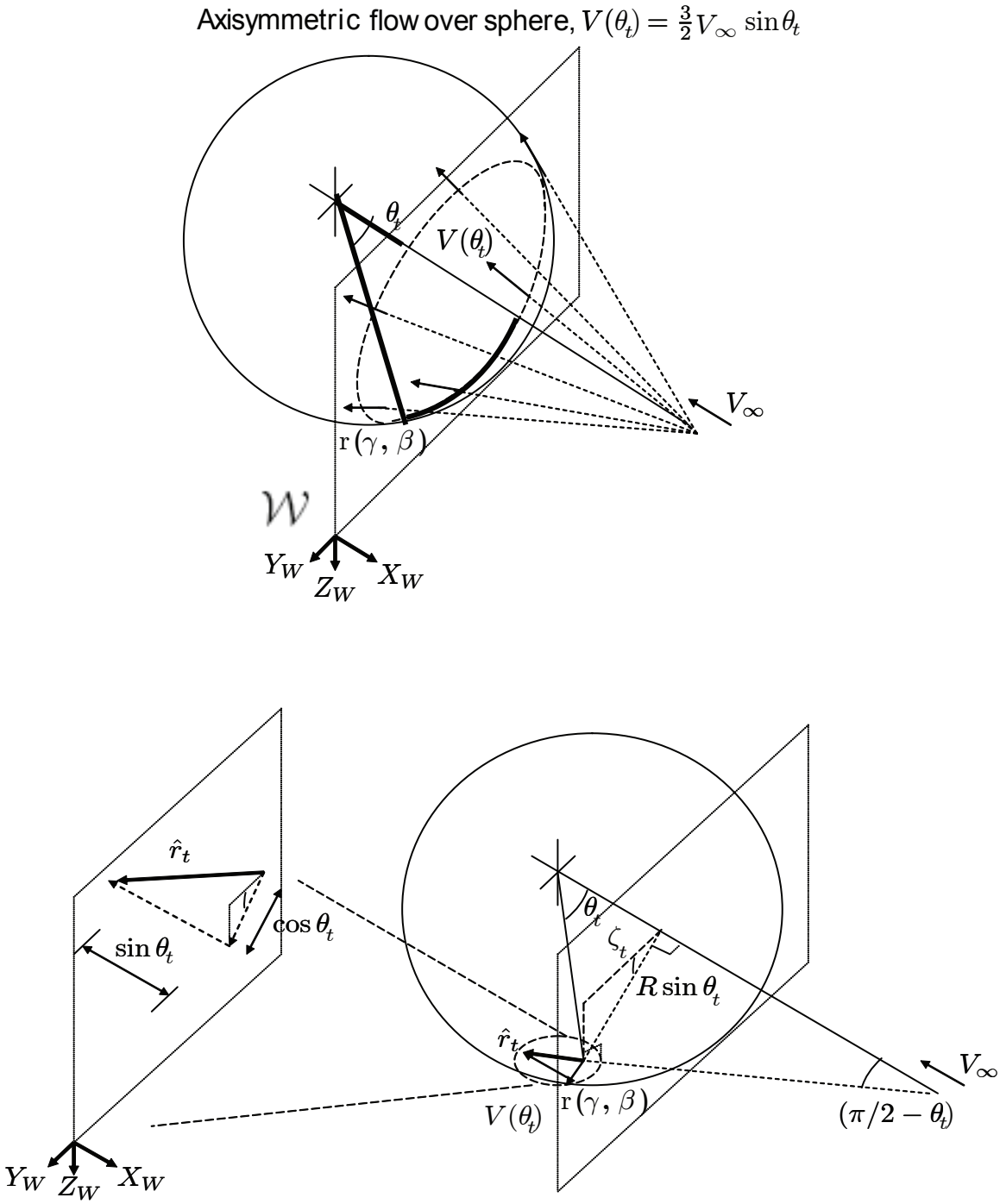

Figure 5.7: Flow field over spherical surface.

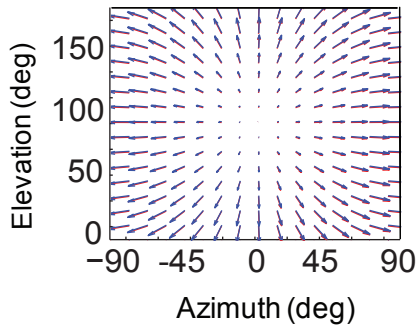

Figure 5.8: Nominal sensor response variation around the hemispherical array.

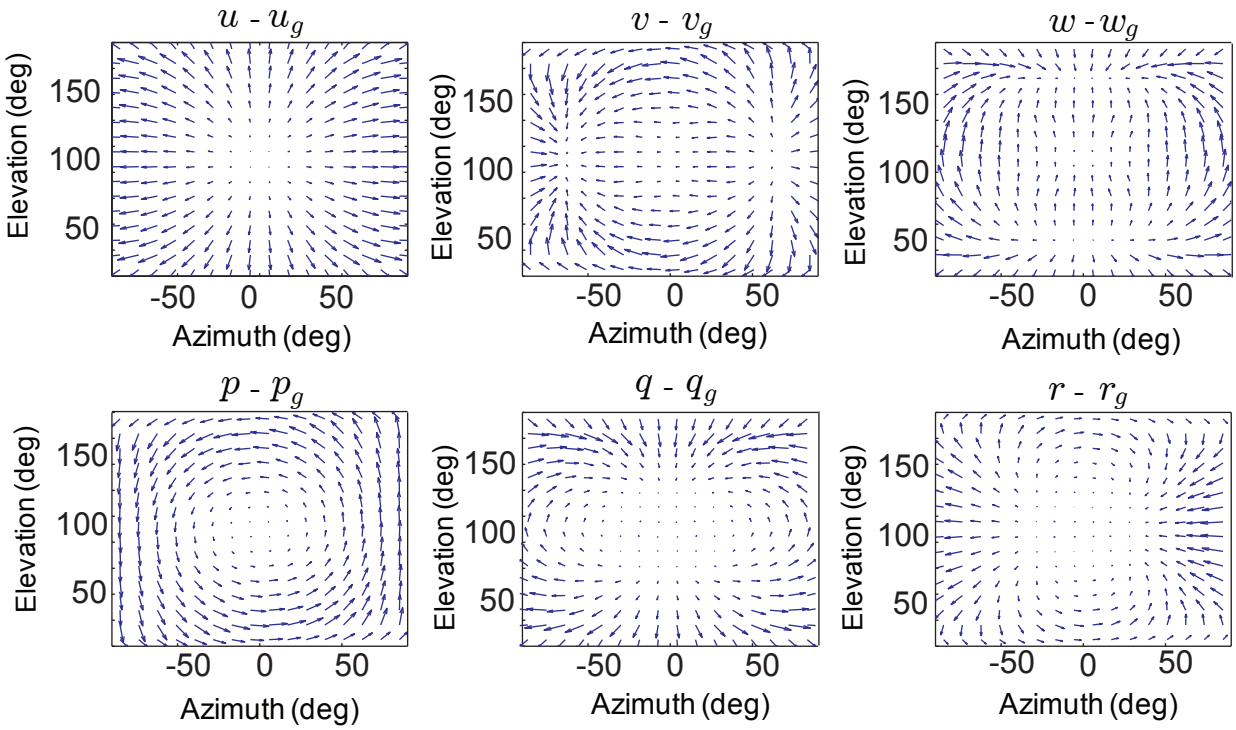

Figure 5.9: Optimal hair array relative velocity sensitivity functions.

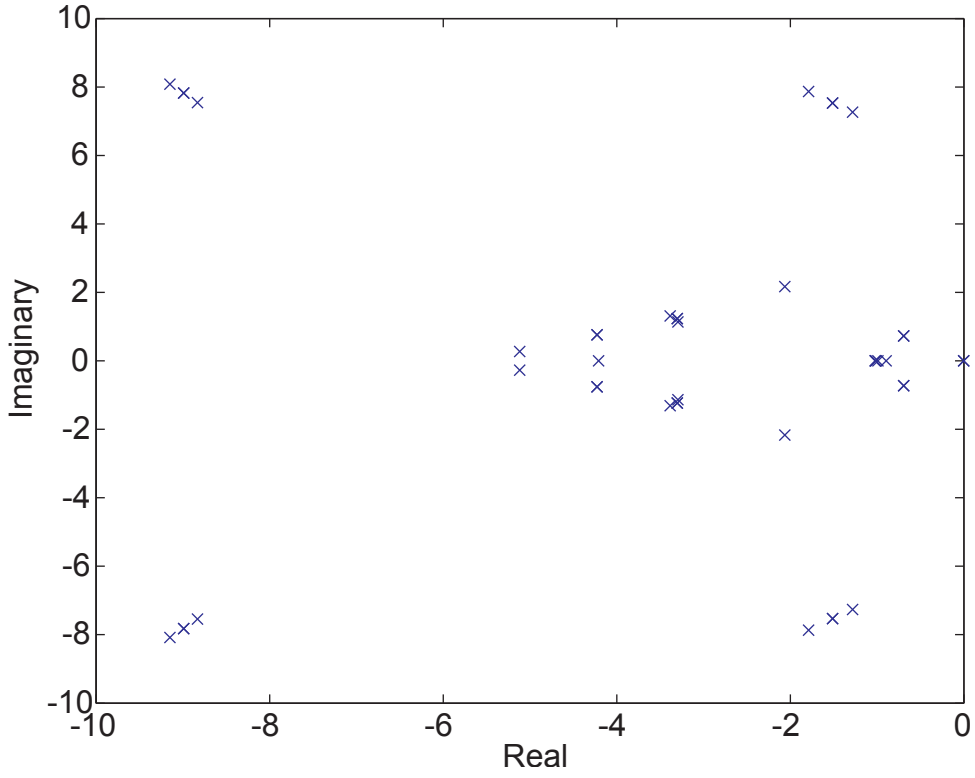

Figure 5.10: Pole locations for the range of modeled environments.

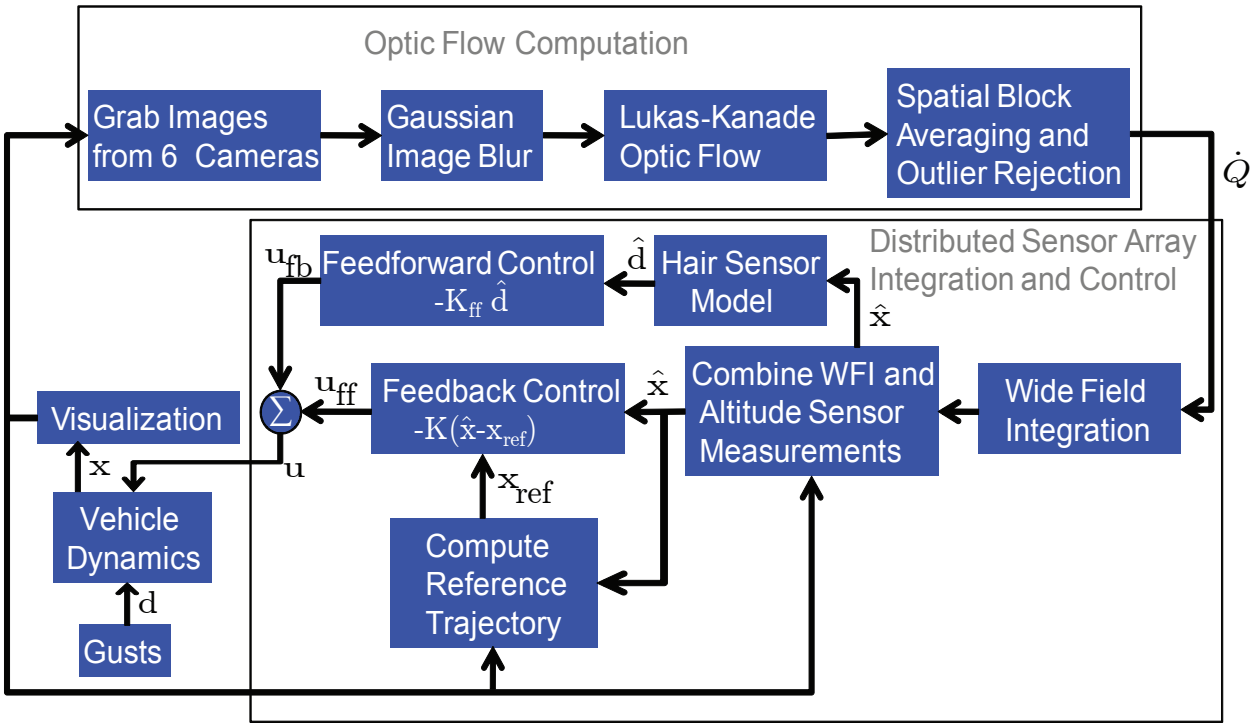

Figure 5.11: Simulation block diagram.

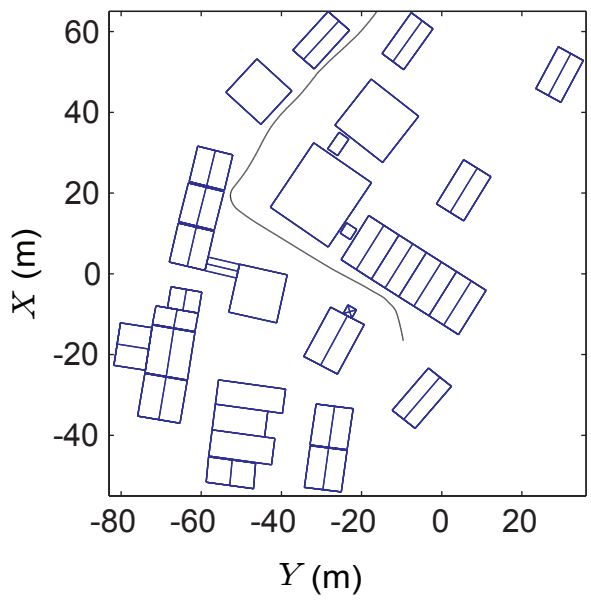

Figure 5.12: Nominal vehicle trajectory in the absence of gust.

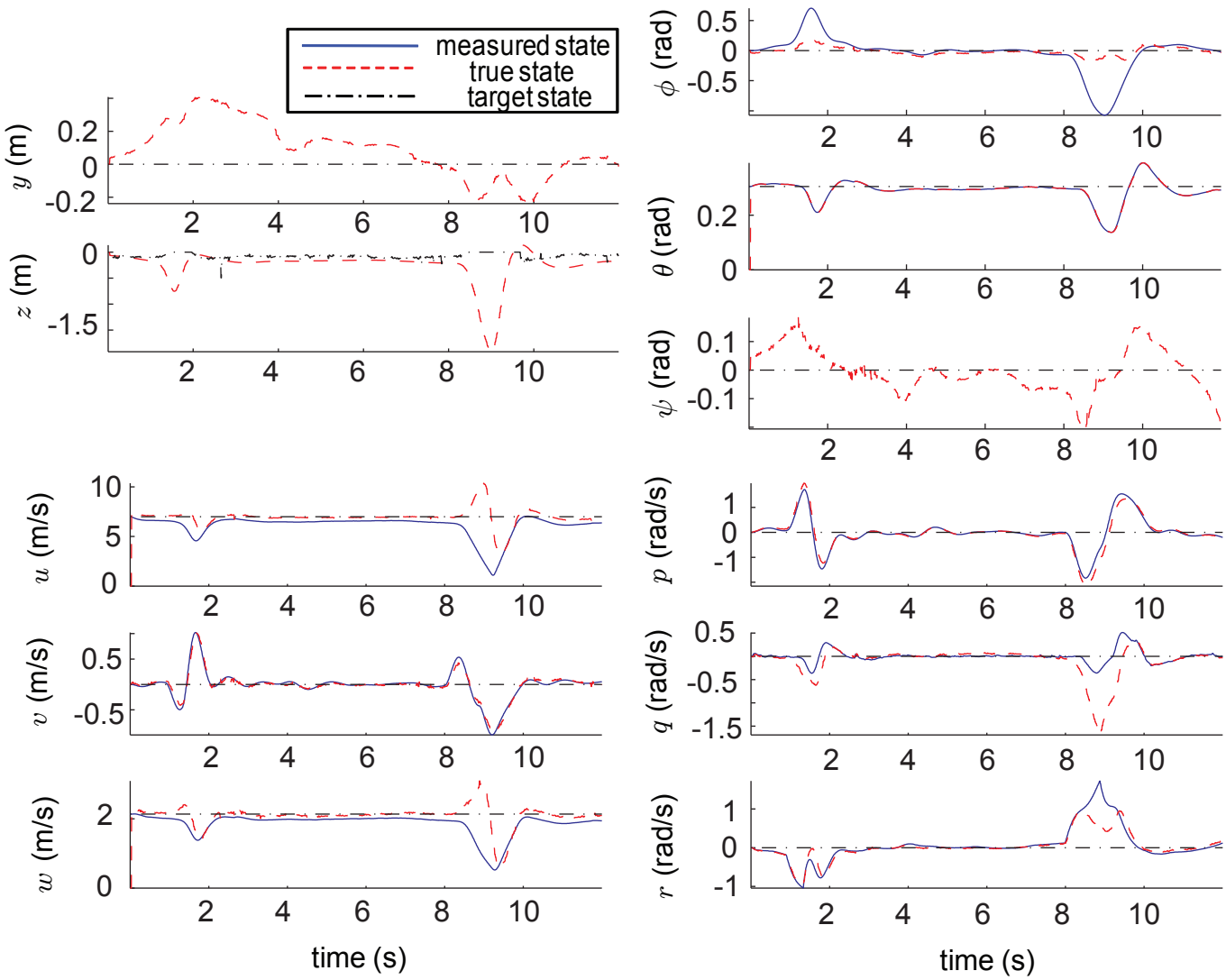

Figure 5.13: Vehicle state variation with time for the nominal trajectory.

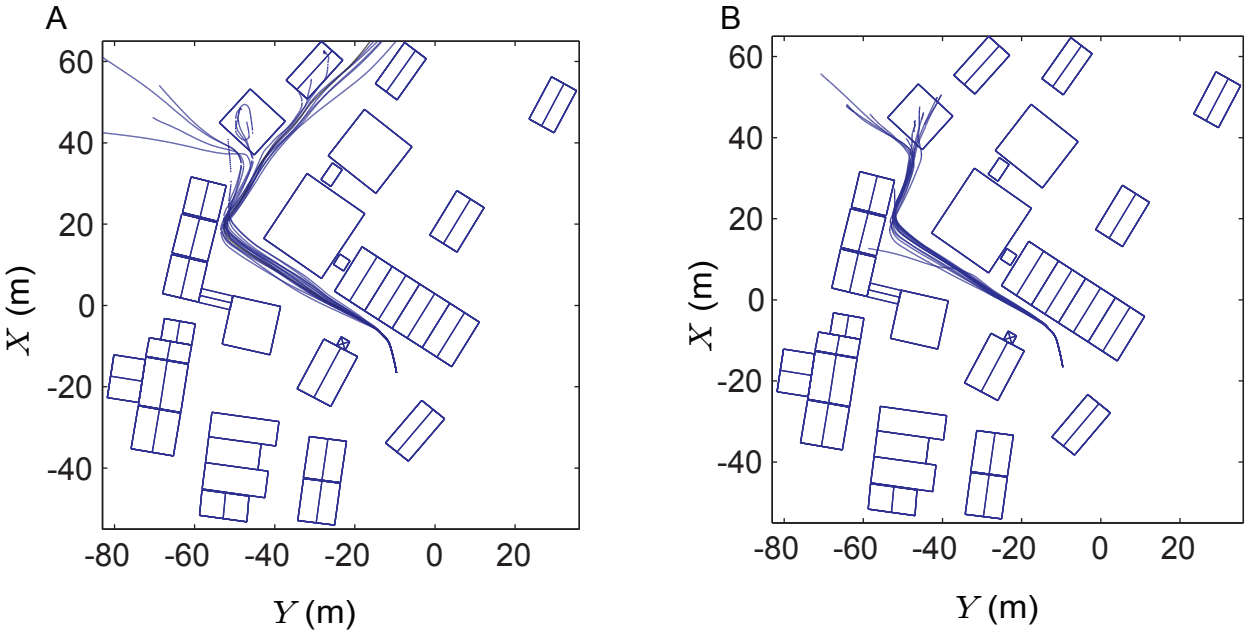

Figure 5.14: Vehicle trajectories in the presence of sustained gust; (A) Optic flow enabled navigation, (B) Optic flow and hair sensor array enabled navigation.

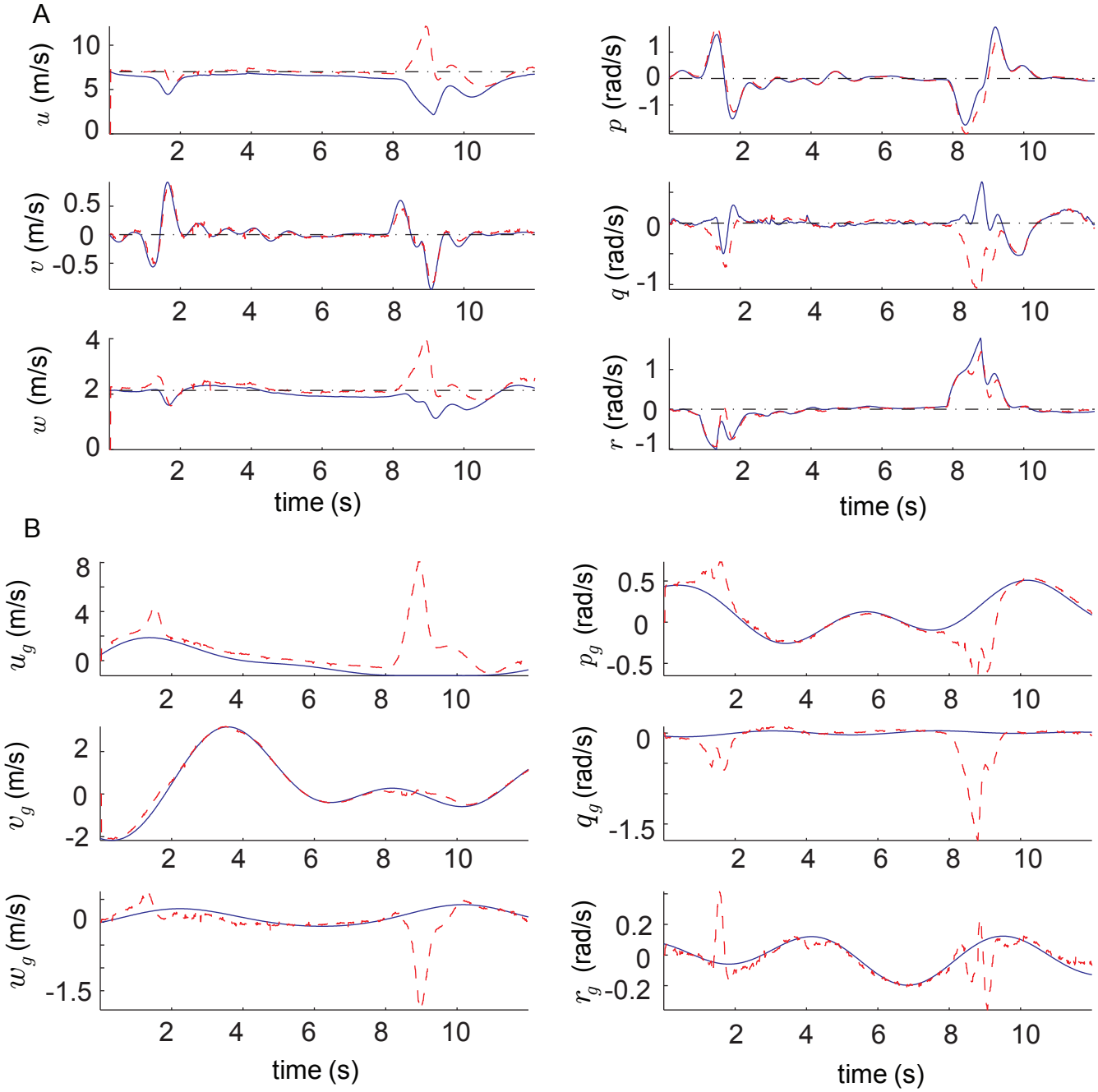

Figure 5.15: Vehicle and gust velocity profiles for a sample trajectory from Fig. 5.14B. Blue solid lines represent true state, red broken lines represent state estimates

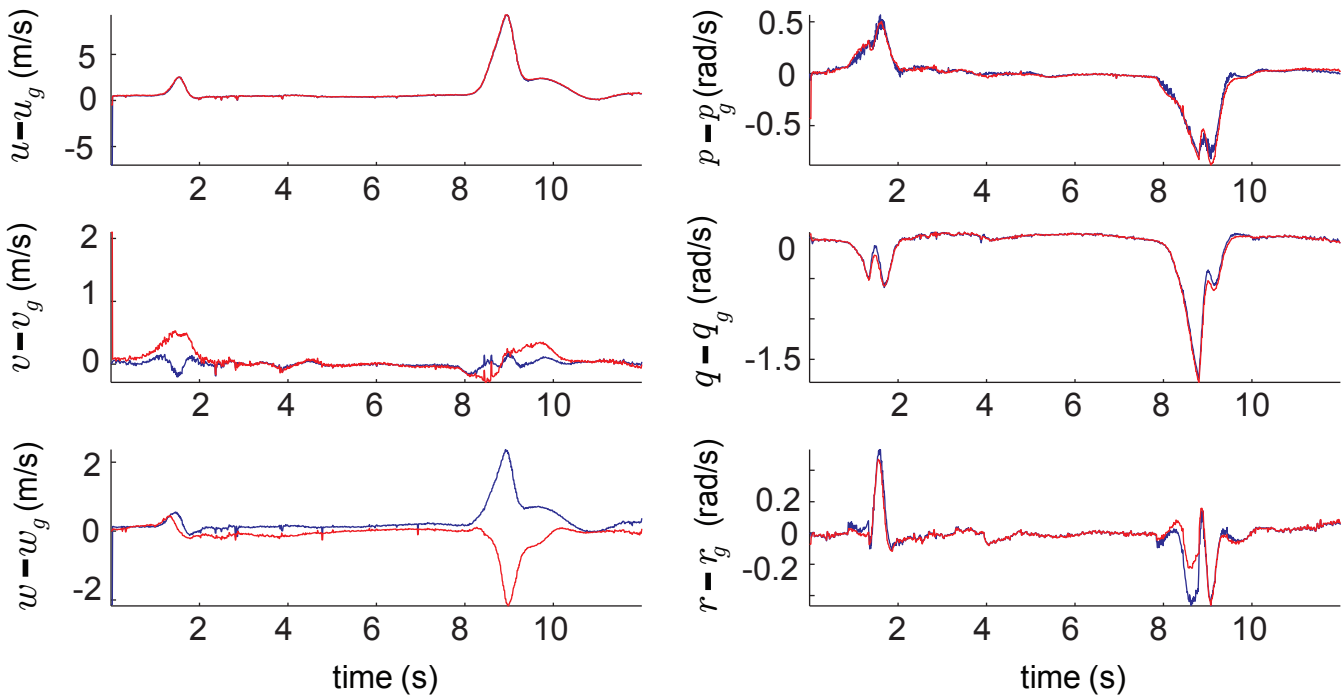

Figure 5.16: Relative wind velocity profiles generated using the hemispherical hair sensor array; blue lines represent true states, red lines represent state estimates.

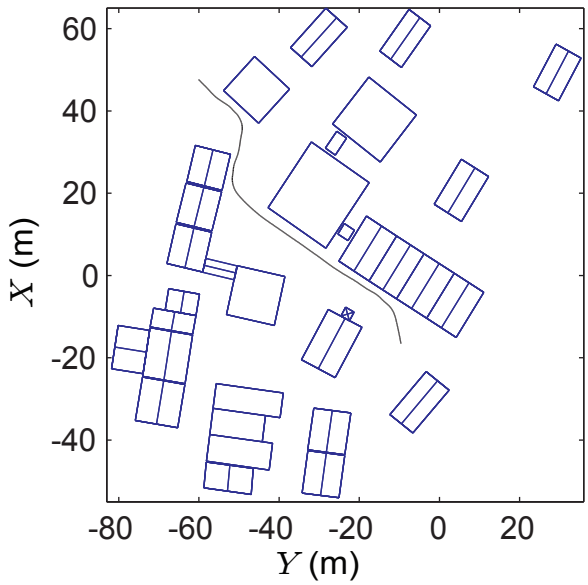

Figure 5.17: Simulation trajectory with GPS and rate gyro measurements in the absence of gust.

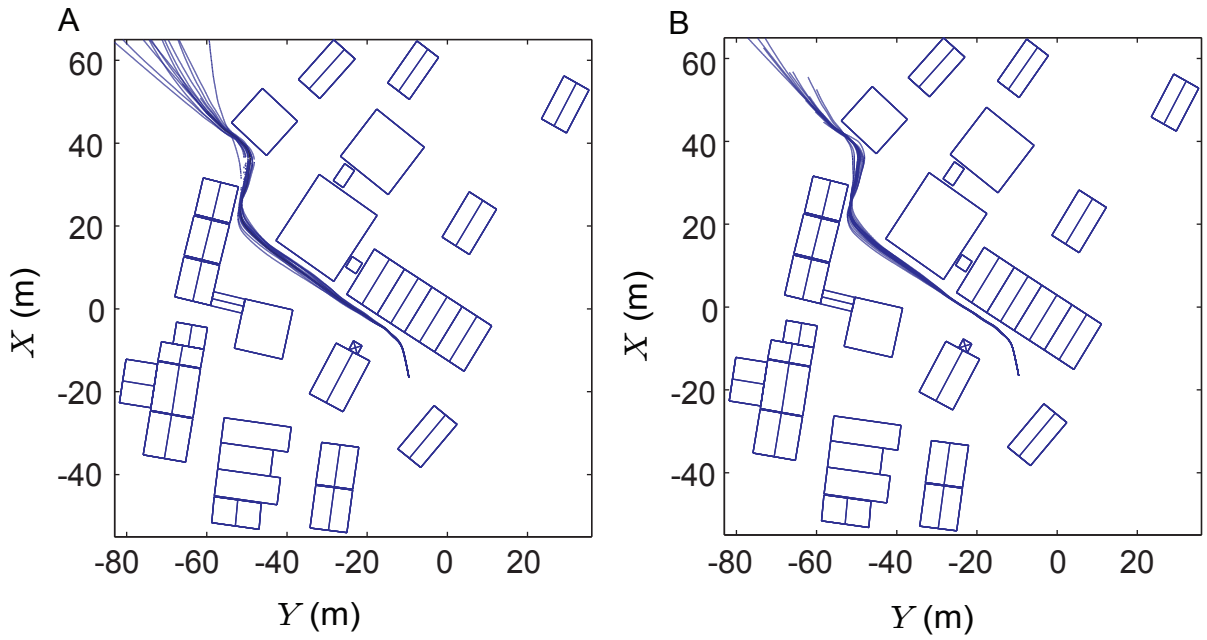

Figure 5.18: Simulation trajectories with GPS and rate gyro measurements in the presence of gust; (A) Optic flow enabled navigation, (B) Optic flow and hair sensor array enabled navigation.

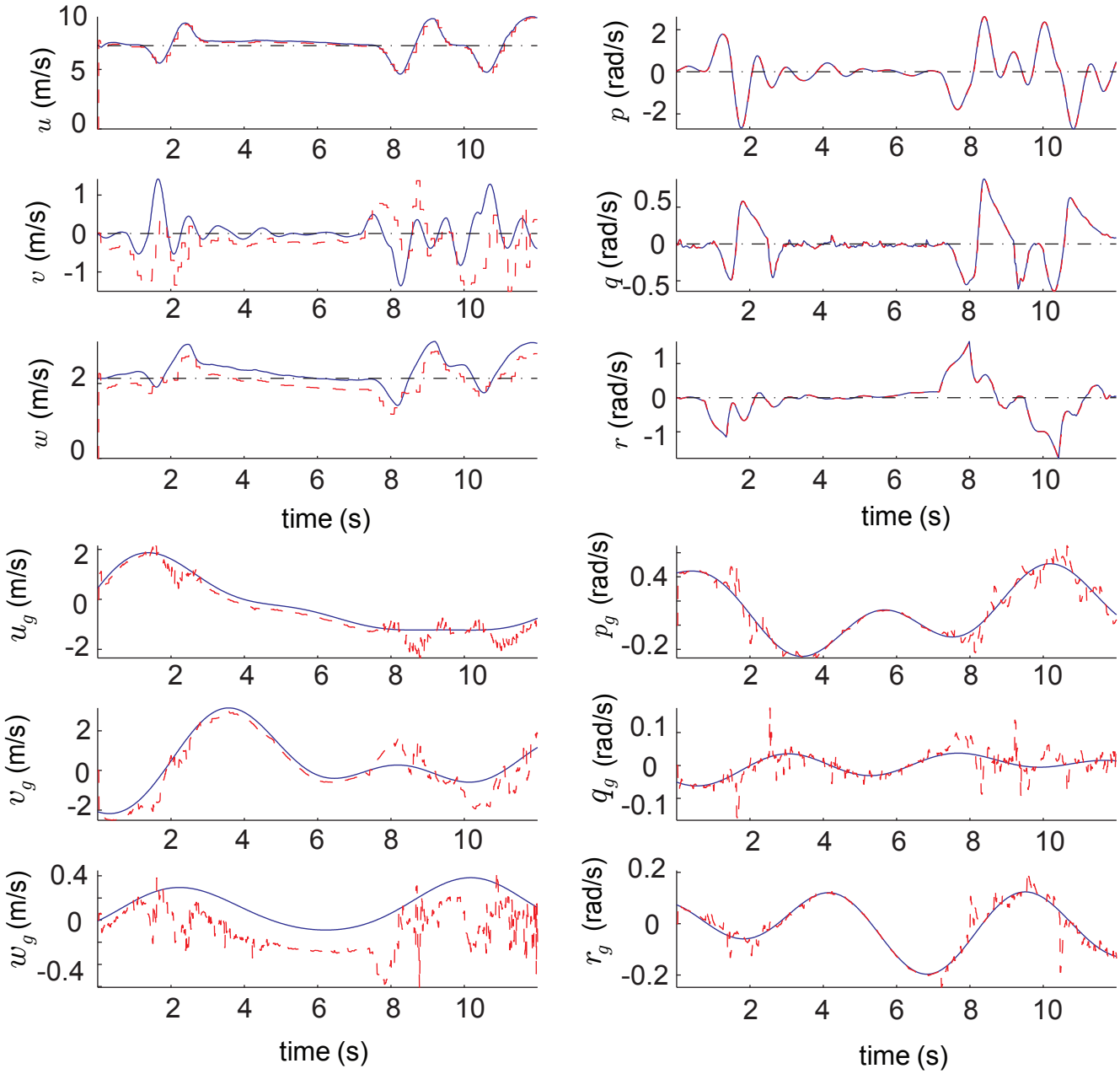

Figure 5.19: Vehicle and gust velocity profiles for a sample trajectory from Fig. 5.18B; blue solid lines represent true states, broken broken lines represent state estimates.

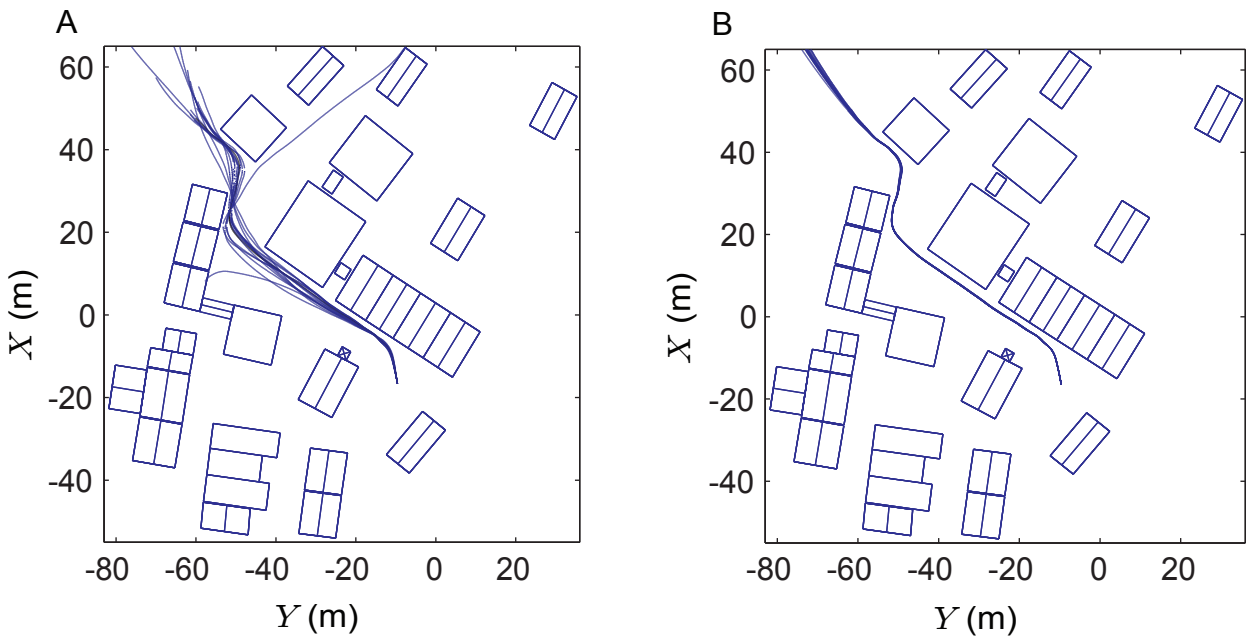

Figure 5.20: Simulation trajectories with GPS and rate gyro measurements in the presence of gust ($v_g = w_g = 0$); (A) Optic flow enabled navigation, (B) Optic flow and hair sensor array enabled navigation.

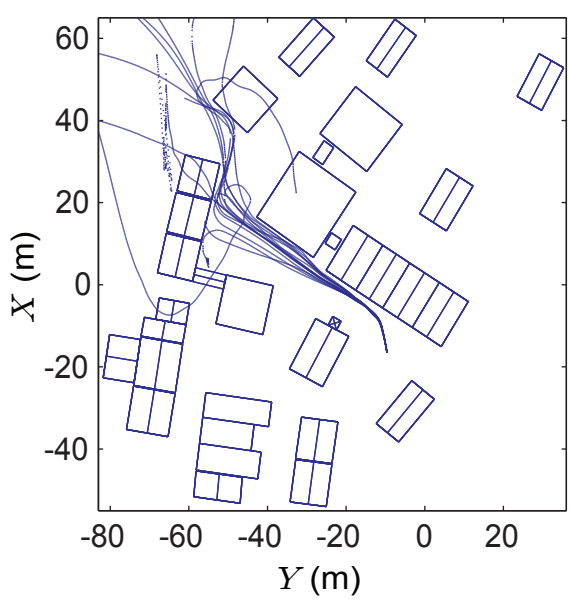

Figure 5.21: Vehicle trajectory using the Kalman filter in the presence of gusts.

Chapter 6

Summary and Conclusions

This chapter summarizes key results, contributions as well as limitations of current work. Areas of future work are also identified.

6.1 Conclusion

The primary focus of this dissertation involves optic flow-guided navigation in a cluttered, urban environment that is subjected to gusts. The central objective of current research is the development of insect-inspired computationally efficient processing algorithms that enable safe reflexive obstacle avoidance and terrain mapping behavior (red and blue trajectories in Fig. 1.1). Accordingly, the H_∞ loop shaping dynamic controller framework is employed in designing feedback gains that provide stabilising commands for the vehicle to follow an obstacle-symmetric path, resulting in safe navigation in unknown and gusty environments. The methodology adopted allows for a degree of uncertainty in the local environment map, which precludes the need for computationally expensive algorithms that generate accurate environment structure from motion or employ optimization-based trajectory generation strategies. The techniques developed in this dissertation are broad-based with application to any distributed sensor array such as the lateral line system found in fish for proximity detection or any point sensor such as sonar, rangefinders and

IMUs. The following key contributions of the dissertation are listed below:

<u>H_∞ controller synthesis framework</u>

- The insect-inspired technique of *wide-field integration* is adapted to the H_∞ controller synthesis framework for designing feedback gains for plants that incorporate environment uncertainty and gusts.

- Robust stability is expressly demonstrated in a rigorous fashion for both planar and 3D urban navigation.

- Safe planar and 3D urban navigation using the H_∞ controller synthesis framework is demonstrated. Dynamic controllers suitable for planar and 3D urban navigation are developed.

- The H_∞ loop shaping approach is shown to overcome the limitation of optic flow outputs by generating accurate pose, proximity and velocity estimates for planar navigation, which is shown to help improve closed loop performance and bandwidth.

- The feedback gains obtained with the loop shaping design methodology are shown to deliver robust vehicle performance in a typical 3D urban environment for both planar and 3D navigation applications, resulting in a physically realizable system requiring minimal computational effort. The current framework extends the previous static analysis to dynamic controllers and the mapping between optic flow estimates and actuator commands for the dynamic controller framework is demonstrated.

Hair mechanosensory system

- The hair sensor array outputs are derived and extraction of navigationally relevant motion cues for both planar and 3D navigation are demonstrated.

- The use of the hair sensor array for the purposes of stability augmentation are demonstrated for the micro-helicopter undergoing planar motion. The hair array outputs are shown to help overcome the limitation of optic flow outputs, and the attendant improvement in the closed loop system performance and bandwidth is demonstrated.

- The hemispherical hair array response for 3D gust rejection application is derived and extraction of suitable motion cues for navigation is demonstrated. The hair array outputs are shown to generate optimal relative wind velocity estimates that minimise noise throughput.

- A biomimetic sensorimotor architecture, patterned on the insect visuomotor system, is developed and various static and dynamic controller frameworks are considered for detection of gusts for safe 3D urban navigation. The performance of the hair sensor system is shown to be dependent on the performance of the optic flow system and the necessary conditions for efficient use of the hair sensor system for gust rejection applications are delineated.

6.2 Limitations

The technique of WFI, which forms the basis of the controller synthesis framework, is computationally efficient for generating relevant motion cues for navigation. However, it is limited to working in regions of sufficient contrast and texture, which is a limitation of modern imaging devices, thus necessitating the use of feature tracking and detection based navigation algorithms [77]. However, the associated computational burden is too large for practical implementation onboard an MAV.

A secondary flaw of WFI is its insensitivity to small obstacles. WFI is ideally suited to detection of large obstacles, with integration over a wide field filtering out perturbations due to small obstacles. Insects have demonstrated detection of to both large and small obstacles [99, 73], suggesting the need for a complementary small-field processing mechanism that enables small obstacle avoidance behavior.

The environment model in chapter 2 does not include a front wall, and hence the measurement model for optic flow does not incorporate longitudinal proximity x. This results in several close encounters of the vehicle as it navigates the urban environment, as seen in Fig. 4.17. This is particularly the case when the vehicle encounters symmetric obstacles in its flight path, which induce minimal optic flow across the visual field. Thus, the current methodology renders navigation hazardous in the presence of such obstacles.

Finally, the methodology adopted for demonstrating safe reflexive navigation behavior is based on the surrounding environment being stationary. Optic flow is a scaled measure of velocity/depth. Hence, a moving environment that generates

either decreased or increased optic flow would cause the vehicle to either move closer or move away, depending on motion direction, much like honeybees flying past a moving wall [18]. Such flight behavior might become hazardous, particularly with the present methodology where close encounters were reported in multiple instances in chapter 4. Thus, stability analysis in a non-stationary environment needs to be investigated.

6.3 Future Work

The need for continuous control capability that is a function of longitudinal proximity x to evade obstacles directly in front was highlighted in chapter 4. The environment model from chapter 2 can be modified to incorporate longitudinal proximity, thus eliminating blind spots on the optic flow sensor and precluding the need for a frontal proximity sensor such as sonar or laser rangefinder.

The current methodology is geared towards enabling safe relexive navigation behavior in a cluttered, obstacle laden environmet (red and blue trajectories from Fig. 1.1), as demonstrated in chapter 4. Thus, the vehicle is seen to wander aimlessly in the large urban environment. True autonomous capability requires implementation of an outer control loop that enables strategic waypoint navigation (yellow line in Fig. 1.1).

Another way forward is to experimentally validate the H_∞ loop shaping design framework, especially for planar navigation, where the resulting controller was shown to be of low order (2 outputs, 3 inputs and 4 states), which is potentially physically

realizable. The demonstration of improvements in closed loop performance and bandwidth, as well as safe reflexive navigation in an uncertain environment subjected to gusts are in order.

The hair sensor array outputs currently do not model flow separation and hence do not incorporate the attendant effects of flow noise and uncertainty. Developing an optimal estimator, similar to the optic flow system, that minimises noise and uncertainty throughput, would deliver relative wind velocity estimates that are robust to the influence of flow separation. Also, experimental validation of the hair sensor array, especially for stability augmentation in planar navigation applications, needs to be demonstrated.

Finally, the H_∞ controller synthesis framework can be extended to other distributed sensor systems.

Bibliography

[1] R. J. Wood, E. Steltz, and R. S. Fearing. Nonlinear performance limits for high density piezoelectric bending actuators. In *International Conference on Robotics and Automation*, Barcelona, Spain, 2005.

[2] R. J. Wood, S. Avadhanula, R. Sahai, E. Steltz and R. S. Fearing. Microrobot design using fiber reinforced composites. *ASME Journal of Mechanical Design*, 130(5), 2008.

[3] A. M. Hoover and R. S. Fearing. Fast scale prototyping for folded millirobots. In *Robotics and Automation, 2008. ICRA 2008. IEEE International Conference on*, pages 886−892, May 2008.

[4] A. K. Brown. Performance test results of an integrated GPS/MEMS inertial navigation package. [Online]. Available: http://www.navsys.com/Papers/0409001.pdf

[5] J. Evers. Biological inspiration for agile autonomous air vehicles. *Platform innovations and system integration for unmanned air, land, and sea vehicles*, Neuilly-sur-Seine, France, 2007.

[6] M. Garratt and J. Chahl. Visual control of an autonomous helicopter. *Proceedings of the 41st aerospace sciences meeting and exhibit*, Reno, Nevada, 2003.

[7] O. Amidi, Y. Mesaki and T. Kanade. A visual odometer for autonomous helicopter flight. *Robotics and Autonomous Systems*, 28(185), 1999.

[8] S. Hrabar and G. S. Sukhatme. Omnidirectional vision for an autonomous helicopter. *IEEE international conference on robotics and automation*, 558−563, 2003.

[9] P. J. Garcia-Pardo, G. S. Sukhatme and J. F. Montgomery. Towards vision-based safe landing for an autonomous helicopter. *Robotics and Autonomous Systems*, 38(1):19−29, 2002.

[10] J. Li and R. Chellappa. A factorization method for structure from planar motion. *Motion and video computing*, 2:154−159, 2005.

[11] F. Kendoula, I. Fantoni and K. Nonamib. Optic flow-based vision system for autonomous 3d localization and control of small aerial vehicles. *Robotics and Autonomous Systems*, 57(6−7):591−602, 2009.

[12] S. L. Waslander and C. Wang. Wind disturbance estimation and rejection for quadrotor position control. *AIAA Infotech@Aerospace Conference and AIAA Unmanned...Unlimited Conference*, Seattle WA, April 2009.

[13] A. Borst and J. Haag. Neural networks in the cockpit of the fly. *Journal of Comparative Physiology A*, 188:419−437, 2002.

[14] M. Egelhaaf, R. Kern, H. G. Krapp, J. Kretzberg, R. Kurtz and A. Warzecha. Neural encoding of behaviourally relevant visual-motion information in the fly. *Trends in Neurosciences*, 25:96−102, 2002.

[15] J. Gibson. *The perception of the visual world*. Houghton Mifflin, Boston, 1950.

[16] C. T. David. Compensation for height in the control of ground speed by *Drosophila* in a new barber's pole wind tunnel. *Journal of Comparative Physiology*, 147(4):485−493,1982.

[17] L. F. Tammero and M. H. Dickinson. The Influence of Visual Landscape on the Free Flight Behavior of the Fruit Fly Drosophila Melanogaster. *Journal of Experimental Biology*, 205:327−343, 2002.

[18] M. V. Srinivasan, S. W. Zhang, M.Lehrer and T. S. Collett. Honeybee navigation *en route* to the goal: Visual flight control and telemetry. *Journal of Experimental Biology*, 199(1):237−244, 1996.

[19] M. V. Srinivasan and S. W. Zhang. Visual Motor Computations in Insects. *Annual Review in Neuroscience*, 27:679−696, 2004.

[20] J. J. Koonderink and A. J. van Doorn. Facts on optic flow. *Biological Cybernetics*, 56(4):247−254, 1987.

[21] K. Hausen. Motion sensitive interneurons in the optomotor system of the fly. part i. the horizontal cells. Structures and signals. *Biological Cybernetics*, 45:143-156, 1982.

[22] K. Hausen. Motion sensitive interneurons in the optomotor system of the fly. part ii. the horizontal cells. Receptive field organization and response characteristics. *Biological Cybernetics*, 46(1):67−79, 1982.

[23] R. Hengstenberg, K. Hausen and B. Hengstenberg. The number and structure of giant vertical cells (vs) in the lobula plate of the blowfly. *Calliphora Erythrocephala. Journal of Comparative Biology*, 149(2):163−177, 1982.

[24] D. C. O' Carroll, S. B. Laughlin, N. J. Bidwell and R. J. Harris. Spatio-temporal properties of motion detectors matched to low image velocities in hovering insects. *Vision Research*, 37(23):3427−3439, 1997.

[25] H. G. Krapp, B. Hengstenberg and R. Hengstenberg. Dendritic structure and receptive-field organization of optic flow processing interneurons in the fly .*Journal of Neurophysiology*, 79:1902−1917, 1998.

[26] J. Conroy, G. Gremillion, B. Ranganathan and S. J. Humbert. Implementation of wide-field integration of optic flow for autonomous quadrotor navigation. *Autonomous Robots*, 27(3):189−198, Oct. 2009.

[27] H. Dahmen, M. Franz and H. G. Krapp. Extracting ego-motion from optic flow: limits of accuracy and neuronal filters. *Processing visual motion in the real world - A survey of computational, neuronal and ecological constraints*, Berlin, Heidelburg: New York: Springer Verlag, 143−168, 2001.

[28] G. Barrows, J. Chahl and M. Srinivasan. Biologically inspired visual sensing and flight control. *The Aeronautical Journal*, 107:159−168, 2003.

[29] B. K. Horn. *Robot vision*. Cambridge, MA: MIT Press and McGraw-Hill, 1986.

[30] E. R. Davies *Machine vision: Theory, algorithms, practicalities*. San Fransisco, CA: Morgan Kaufmann, 2005.

[31] M. V. Srinivasan, J. Chahl, K. Weber, S. V. M. Nagle and S. W. Zhang. Robot Navigation Inspired by Principles of Insect Vision. *Robotics and Autonomous Systems*, 26:203−216, 1999.

[32] M. Franz and H. Mallot. Biomimetic robot navigation. *Robotics and Autonomous Systems*, 30:133−153, 2000.

[33] J. Santos-Victor and G. Sandini. Embedded visual behaviors for navigation. *Robotics and Autonomous Systems*, 19:299−313, 1997.

[34] D. Coombs, M. Herman, T. Hong and M. Nashman. Real-time obstacle avoidance using central flow divergence, and peripheral flow. *IEEE Transactions on Robotics and Automation*, 14:49−59, 1998.

[35] T. Netter and N. Franceschini. A robotic aircraft that follows terrain using a neuromorphic eye. *Proceedings of the IEEE/RSJ IROS conference on robots and systems*, Lausanne, Switzerland, 2002.

[36] L. Muratet, S. Doncieux, Y. Briere and J. Meyer. A contribution to vision-based autonomous helicopter flight in urban environments. *Robotics and Autonomous Systems*, 50(4):195−209, 2005.

[37] J. Serres, D. Dray, F. Ruffier and N. Franceschini. A vision-based autopilot for a miniature air vehicle: joint speed control and lateral obstacle avoidance. *Autonomous Robots*, 25:103−122, 2008.

[38] S. Hrabar and G. S. Sukhatme. A comparison of two camera configurations for optic-flow based navigation of a UAV through urban canyons. *IEEE/RSJ international conference on intelligent robots and systems*, 2673−2680, 2004.

[39] S. Hrabar, G. S. Sukhatme, P. Corke, K. Usher and J. Roberts. Combined optic-flow and sterero-based navigation of urban canyons for a UAV. *Proceedings of the IEEE International Conference on Intelligent Robots and Systems*, IEEE Publications:3309−3316, Piscataway, NJ, Dec. 2005.

[40] S. Griffiths, J. Saunders, A. Curtis, B. Barber, T. McLain and R. Beard. Maximizing minature aerial vehicles: obstacle and terrain avoidance for MAVs. *IEEE Robotics and Automation Magazine*, 13(3):34−43, 2006.

[41] W. E. Green, P. Y. Oh and G. Barrows. Flying insect inspired vision for autonomous aerial robot maneuvers in near-earth environments. *Proceedings of the IEEE international conference on robotics and automation*, New Orleans, LA, 2004.

[42] R. Harrison. A biologically inspired analog IC for visual collision detection. *IEEE Transactions on Circuits and Systems*, 52(11):2308−2318, 2005.

[43] J. C. Zufferey and D. Floreano. Fly-inspired visual steering of an ultralight indoor aircraft. *IEEE Transactions on Robotics*, 22:137−146, 2006.

[44] J. S. Chahl and M. V. Srinivasan. A complete panoramic vision system, incorporating imaging, ranging, and three dimensional navigation. *Proceedings of the IEEE Workshop on Omnidirectional Vision*, IEEE Publications:104−111, Piscataway, NJ, Aug. 2002.

[45] N. Franceschini, F. Ruffier and J. Serres. A bio-inspired flying robot sheds light on insect piloting abilities .*Current Biology*, 17(4):329−335, 2007.

[46] A. Beyeler, J. C. Zufferey and D. Floreano. Optic-flow to steer and avoid collisions in 3D. *Flying Insects and Robotics*, Springer-Verlag, Berlin, 2009.

[47] A. X. Miao, G. L. Zacharias and R. Warren. Passive navigation from image sequences: A practitioner's approach AiAA Flight Simulation Technologies Conference. AIAA Paper, 1996−3556, 1996.

[48] J. J. Kehoe, A. S. Watkins, R. S. Causey and R. Lind. State estimation using optical flow from parallax-weighted feature tracking. AIAA Guidance, Navigation and Control Conference and Exhibit, AIAA Paper, 2006−6721, 2006.

[49] A. R. Bruss and K. P. Horn. Passive navigation. *Computer Vision, Graphics, and Image Processing*, 21(1):3−20, 1983.

[50] M. O. Franz, J. S. Chahl and H. G. Krapp. Insect-inspired estimation of egomotion. *Neural Computation*, 16(11):2245−2260, 2004.

[51] O. Toupet, J. D. Paduano, R. Panish, R. Sedwick and E. Frazzoli. Augmenting state estimates with multiple camera visual measurements. AIAA Infotech at Aerospace Conference and Exhibit, AIAA Paper, 2007−2983, 2007.

[52] T. P. Webb, R. J. Prazenica, A. J. Kurdila and R. Lind. Vision-based state estimation for autonomous micro air vehicles. *Journal of Guidance, Control and Dynamics*, 30(3):816−826, 2007.

[53] B. Call, R. Beard and C. P. Taylor. Obstacle avoidance for unmanned vehicles using image feature tracking. In *Proceedings of AIAA Guidance, Navigation and Control Conference*. AIAA-2006-6541, Keystone, CO, 2006.

[54] A. J. Grunwald. Stability and control of a remotely controlled indoors micro hovering vehicle. In of the AIAA Guidance, Navigation and Control Conference and Exhibit. AIAA-2005-6283, San Fransisco, CA, 2005.

[55] P. Gurfil and H. Rotstein. Partial aircraft state estimation from visual motion using the subspace constraints approach. *Journal of Guidance, Control and Dynamics*, 24(5):1016-1028, 2001.

[56] M. Blosch, S. Weiss, D. Scaramuzza and R. Siegwart. Vision based MAV navigation in unknown and unstructured environments. *IEEE international conference on robotics and automation*, 21−28, Anchorage AK, 2010. doi:10.1109/ROBOT.2010.5509920

[57] A. J. Davison, I. D. Reid, N. D. Molton and O. Stasse. Monoslam: Real-time single camera slam. *IEEE Transactions on Pattern Analysis and Machine Intelligence*, 29(6):1052−1067, June 2007.

[58] S. J. Humbert, A. M. Hyslop and M. W. Chinn. Experimental validation of wide-field integration methods for autonomous navigation. *Proceedings of the IEEE Conference on Intelligent Robots and Systems (IROS)*, San Diego CA, 2007.

[59] S. J. Humbert, R. M. Murray and M. H. Dickinson. Sensorimotor convergence in visual navigation and flight control systems. In *Proceedings of the 16th IFAC World Congress*, vol. 16, Prague, Czech Republic, 2005.

[60] S. J. Humbert and A. M. Hyslop. Bio-inspired visuomotor convergence. *IEEE Transactions on Robotics*, 26(1):121−130, 2010.

[61] M. Frye and M. H. Dickinson. Fly flight: A Model for the Neural Control of Complex Behavior. *Neuron*, 32:385−388, 2001.

[62] A. M. Hyslop and S. J. Humbert. Autonomous navigation in three-dimensional environments using wide-field integration of optic flow. *Journal of Guidance, Control and Dynamics*, 33(1):147−159, 2010.

[63] A. Lanzon. Simultaneous synthesis of weights and controllers in H_∞ loop-shaping. *Proceedings of the 40th IEEE Conference on Decision and Control*, Orlando, Fl, Dec. 2001.

[64] J. Sefton and K. Glover. Pole-zero cancellations in the general H_∞ problem with reference to a two-block design. *Systems and Control Letters*, 14:295−306, 1990.

[65] S. Skogestad and I. Postlethwaite. *Multivariable Feedback Control*, Wiley, 1996.

[66] G. Vinnicombe, G. *Uncertainty and Feedback*. Imperial College Press, 2001.

[67] J. Conroy, S. J. Humbert, D. Pines. System identification of a rotary-wing micro air vehicle. *Journal of the American Helicopter Society*, 56(2), 2011.

[68] Military Specification. Flying Qualities of Piloted Airplanes. Tech. Rep. U.S. Military Specification MIL−F−8785C.

[69] Military Specification. Flying Qualities of Piloted Airplanes. Tech. Rep. U.S. Military Specification MIL−HDBK−1797.

[70] D. MacFarlane and K. Glover. A loop shaping design procedure using H_∞ synthesis *IEEE Transactions on Automatic Control*. AC-36, 759−769, 1992.

[71] J. Keshavan and S. J. Humbert. MAV Stability Augmentation Using Weighted Outputs from Distributed Hair Sensor Arrays. *American Control Conference*, Baltimore MD, 2010.

[72] S. J. Humbert and A. M. Hyslop. Bio-inspired visuomotor convergence. *IEEE Transactions on Robotics and Automation*, 2009.

[73] J. W. Aptekar, P. A. Shoemaker and M. A. Frye. Figure Tracking by Flies is Supported by Parallel Visual Streams. *Current Biology*, March 2012. doi:10.1016/j.cub.2012.01.044

[74] A. X. Miao, G. L. Zacharias and R. Warren. Passive navigation from image sequences: A practitioner's approach. AIAA Flight Simulation Technologies Conference, AIAA Paper 1996−3556, 1996.

[75] L. Muratet, S. Doncieux and J. A. Meyer. A biomimetic reactive navigation system using the optical flow for a rotary-wing UAV in urban environment. *Proceedings of the 35th International Symposium of Robotics [CD-ROM], International Symposium of Robotics, Paris, 2004.*

[76] A. M. Hyslop and S. J. Humbert. Wide-field integration methods for autonomous navigation of 3-D environments. AIAA Guidance, Navigation and Control Conference, AIAA Paper, 2008.

[77] G. N. DeSouza and A. C. Kak. Vision for mobile robot navigation: A survey. *IEEE Transactions on Pattern Analysis and Machine Intelligence*, 24(2):237−266, 2002.

[78] G. Klein and D. Murray. Parallel tracking and mapping for small ar workspaces. *Proceedings 6th IEEE and ACM International Symposium on Mixed and Augmented Reality ISMAR 2007*:225234, 2007.

[79] H. Chao, Y. Cao and Y.Chen. Autopilots for small fixed-wing unmanned air vehicles: A survey. *Proceedings of the IEEE International Conference on Mechatronics and Automation*, IEEE Publications, Piscataway, NJ, 3144-3149, Sept. 2007. doi: 10.1109/ICMA.2007.4304064

[80] M. Gewecke, H. G. Heinzel and J. Philippen. Role of antennae of the dragonfly Orthetrum Cancellatum in flight control. *Nature*, 249:579−582, 1974.

[81] J. M. Camhi. Yaw-correcting postural changes in locusts. *Journal of Experimental Biology*, 52:519−531, 1970.

[82] J. M. Camhi. Locust wind receptors I. Transducer mechanics and sensory response. *Journal of Experimental Biology*, 50:335−348, 1969.

[83] G. K. Taylor and H. G. Krapp. *Sensory Systems and Flight Stability: What Do Insects Measure and Why?* Fink Publishing Chesapeake:275, 1982.

[84] D. M. Guthrie. Observations on the nervous system of the flight apparatus in the locust Schistocerca Gregaria. *Q. J. Micr. Sci.*, 105:320−328, 1964.

[85] D. M. Guthrie. The functions and fine structure of the cephalic airflow receptor in Schistocerca Gregaria. *Journal of Cell Science*, 1:463–470, 1966.

[86] T. Weis-Fogh. An aerodynamic sense organ stimulating and regulating flight in locusts. *Nature*, 164:873−874, 1949.

[87] T. Weis-Fogh. Biology and physics of locust flight. iv. Notes on sensory mechanisms in locust flight. *Philosophical Transactions of the Royal Society in London*B, 239:553−584, 1956.

[88] M. Gewecke and J. Philippen. Control of the horizontal flight course by air-current sense organs in Locusta Migratoria. *Physiological Entomology*, 3:43−52, 1978.

[89] U. Smola. Investigation into the topography, mechanics and aerodynamics of the sensory hairs on the head of Locusta Migratoria. *Zeitschrift fur Vergleichende Physiologie*, 67:382−402, 1970b.

[90] H. Reichert. Sensory Inputs and Flight Orientation in Locusts. *Comparative Biochemistry and Physiology* A, 104:647−657, 1993.

[91] J. Bacon and M. Tyrer. The innervation of the wind-sensitive head hairs of the locust, Schistocerca Gregaria. *Physiological Entomology*, 4:301−309, 1979.

[92] N. M. Tyrer, J. P. Bacon and C. A. Davies. Sensory projections from the wind-sensitive head hairs of the locust Schistocerca Gregaria. Distribution in the central nervous system. *Cell Tissue Res.*, 203:79−92, 1979.

[93] Z. Fan, J. Chen, J. Zou, D. Bullen, C. Liu and F. Delcomyn. Design and fabrication of artificial lateral line flow sensors. *Journal of Micromechanics and Microengineering*, 12:655−661, 2002.

[94] N. Chen, C. Tucker, J. M. Engel, Y. Yang, S. Pandya and C. Liu. Design and Characterization of artificial haircell sensor for flow sensing with ultra-

high velocity and angular sensitivity. *Journal of Micromechanical Systems*, 16(5):999−1014, 2007.

[95] C. G. Broyden. A class of methods for solving nonlinear simultaneous equations. *Math. of Computations*, 19:577−593,1965.

[96] J. Gadewadikar, F. L. Lewis, K. Subbarao, K. Peng, B. M. Chen. H-Infinity static output feedback control for rotorcraft. *Journal of Intelligent Robot Systems*, 54:629−646, 2009.

[97] D. M. Bevly. Global Positioning System (GPS): A low cost velocity sensor for correcting inertial sensor errors on ground vehicles. *Journal of Dynamic Systems, Measurement and Control*, 126:255−264, 2004.

[98] M. L. O'Connor. *Carrier-Phase Differential GPS for Automatic Control of Land Vehicles: A Dissertation*. PhD thesis, Stanford University, December 1997.

[99] M. Egelhaaf. On the neuronal basis of figure-ground discrimination by relative motion in the visual system of the fly. ii. figure detection cells, a new class of visual interneurones. *Biological Cybernetics*, 52:195−209, 1985.